



MONASH University

Investigating the Catalytic and Stereoselective Effects of Oriented  
External Electric Fields on the Cyclisation of 2'-Aminochalcone

Adrea Snow

Supervisors: Prof. Ekaterina Pas  
Prof. Michelle Coote

Monash School of Chemistry

November 2021

# Contents

<b>Contents</b>	ii
<b>List of Figures</b>	iv
<b>List of Tables</b>	ix
<b>1 Introduction</b>	2
1.1 Reaction control through oriented external electric fields	2
1.2 Extending the use of OEEFs to solution	7
1.3 The cyclisation of 2'-aminochalcone	8
1.4 Theoretical methodology of reaction rates	9
1.5 Computational chemistry	12
1.5.1 Thermodynamic corrections to the internal energy	13
1.5.2 Continuum solvation models	14
1.6 Research objectives	15
<b>2 Computational details</b>	17
<b>3 Results and discussion</b>	20
3.1 Pathway selection	20
3.2 Static benchmarks based on cardinal field directions, following the "rules"	33
3.2.1 Benchmarking the non-activated pathway barrier as a function of $F_Y$	33
3.2.2 Benchmarking the bias of the <i>S</i> isomer over the <i>R</i> isomer as a function of $F_Z$	35
3.2.3 Investigating the role of dielectric medium (CPCM) on OEEF perturbation	38
3.3 Identifying optimal OEEF directions for catalysis and <i>R/S</i> selectivity	40
3.3.1 Electron density difference analysis of the optimised OEEF perturbations	43

3.4	Benchmarking the optimised OEEF directions on relaxed geometry . . . . .	45
3.5	Investigating the effects of charged derivatisation of 2'-aminochalcone . . . . .	49
3.6	Thermodynamic benchmarking of the derivatised and non-derivatised species . . . . .	56
<b>4</b>	<b>Conclusion and Future Research . . . . .</b>	<b>60</b>
<b>5</b>	<b>References . . . . .</b>	<b>62</b>
<b>Appendix</b>	<b>  A Raw data from the pathway benchmarking in Section 3.1 . . . . .</b>	<b>xiii</b>
<b>  B Raw data and reaction trajectories from Section 3.4 . . . . .</b>	<b>xv</b>	
<b>  C Electron density difference maps of the derivatives discussed in Section 3.5 . . . . .</b>	<b>xviii</b>	
<b>  D Raw data and reaction trajectories from Section 3.4 . . . . .</b>	<b>xx</b>	
<b>  E Transition state geometries and reaction trajectories from the OEEF perturbed benchmarks     in Section 3.6 . . . . .</b>	<b>xxi</b>	
<b>  F Full theoretical choices, approximations and precision used throughout the project . . . . .</b>	<b>xxv</b>	

# List of Figures

1.1 Valence bond diagrams of a generic Diels-Alder reaction demonstrating (a) the uncatalysed, concerted pathway and (b) the resulting stepwise pathway with reduced barrier as a product of the stabilisation of the charge-transfer state, by the electric field denoted in the centre box. Reproduced from Stuyver <i>et al.</i> <sup>8</sup> . . . . .	3
1.2 Polarised (I and III) and non-polarised (II) transition states of the model Diels-Alder reaction, used in the STM OEEF catalysis experiments of Aragonès <i>et al.</i> <sup>9</sup> . . . . .	4
1.3 OEEF direction and the resulting effect on the reaction trajectory for the Diels-Alder cyclisation of an asymmetrical ethene derivative into cyclopentadiene. Reproduced from Wang <i>et al.</i> <sup>11</sup> . . . . .	5
1.4 Resulting <i>R</i> and <i>S</i> reaction pathways of the asymmetric Diels-Alder reactions from Wang <i>et al.</i> , <sup>11</sup> as perturbed by an OEEF of $F_X = 0.005 \text{ au} (\sim 0.26 \text{ V}\cdot\text{\AA}^{-1})$ . . . . .	6
1.5 Example potential energy surface of hypothetical molecule A–B–C, displaying the degrees of freedom of the length of bonds A–B and B–C on the X and Z axes, with energy being displayed on the Y axis, reproduced from Cramer. <sup>20</sup> . . . . .	9
3.1 Relative reaction trajectories of the non-activated and five catalysed reaction pathways of <b>1</b> → <b>4</b> . Where no transition states are present, that portion of the pathway was found to be barrierless. . . . .	24
3.2 Transition state 2 of each of the pathways, excluding the Brønsted acid 2 pathway, as due to its barrierless nature, no transition state geometry exists. The labels show the transition state bonding distance, in angstrom. . . . .	26

3.3	a) PES scans along the forming bond of the Lewis base pathway, with the free proton on the Lewis base (blue) and on the cyclising amine (orange). b) PES scan of the $N_{LB} - C$ bond distance of the protonated Lewis base leaving the carbonyl carbon, prior to cyclisation occurring. The scans in a) were performed with constrained $N_{LB} - C$ bond distances, in order to prevent the dissociation of the species. . . . .	27
3.4	Isosurfaces of the LUMO from the non-activated and Brønsted acid 2 pathway intermediate species, following an isovalue of 0.05. . . . .	28
3.5	Barrier height of the cyclisation step of each of the pathways plotted against their respective transition state bonding distance. A linear trendline ( $R^2 = 0.996$ ) has been added to demonstrate the linearity of the non-intermolecularly stabilised species transition state bond length as a function of their barrier height. The Brønsted acid 2 pathway has been omitted, as no transition state geometry exists. . . . .	29
3.6	$\log(k)$ Rate constants of the non-activated pathway as a function of temperature. . . .	31
3.7	Non-activated transition state of 2'-aminochalcone, as aligned to the cardinal axes . .	33
3.8	a) Potential energy of the reactant, transition state and product as a function of $F_Y$ , in SMD ethanol. The energies are all relative to the unperturbed reactant. b) Reaction trajectory based on the potential energy from the OEEF scan in Section 3.2.1, coloured from most negative field direction (brightest) to most positive (most dull). . . . .	34
3.9	Magnitude of the molecular dipole of the reactant, transition state and product of the non-activated pathway, as a function of catalytic OEEF field strength. . . . .	34
3.10	The resulting potential energy barrier heights of the reaction trajectory as a function of the strength of $F_Y$ . . . . .	35

3.11 a) Potential energy of the <i>S</i> isomer of the reactant, transition state and product as a function of $F_Z$ , in SMD ethanol (b). The energies are all relative to the unperturbed reactant. b) Reaction trajectory based on the potential energy from the OEEF scan in Figure 3.11 , coloured from most negative field direction (brightest) to most positive (most dull). . . . .	36
3.12 Magnitude of the molecular dipole of the reactant, transition state and product of the non-activated pathway, as a function of $ F_Z $ . . . . .	36
3.13 The resulting gas phase and SMD solvated barrier heights of reaction trajectory as a function of the strength of $F_Z$ . . . . .	37
3.14 Reduction in barrier heights of the OEEF-perturbed and non-perturbed scans of the non-activated pathway as a function of solvent dielectric constant. The barrier heights are all relate to their maximum energy at $\epsilon_r = 0$ . . . . .	39
3.15 Differences between the OEEF perturbed barrier heights and non OEEF-perturbed scans of the non-activated pathway as a function of CPCM dielectric constant. This plot shows the amount of stabilisation afforded by the CPCM dielectric pertaining to the stabilisation of OEEF induced charge separation. . . . .	39
3.16 Initial, rough scan of the catalytic stabilisation of the <i>S</i> isomer afforded by various OEEFs on the non-activated transition state, relative to the non-OEEF perturbed molecule. Each sphere represents a perturbed field direction, and it's colour represents the magnitude of the perturbation from most stabilising (red) to least (blue). The arrows represent the most stabilising field direction (yellow), the relative magnitude and direction of the molecular dipole of the unperturbed transition state (blue) and the perturbed transition state (pink). . . . .	40

3.17 More granular scans of a) the catalytic effects of the OEEF on the <i>S</i> isomer transition state, and b) the stereoselective effects of the OEEF for the <i>S</i> isomer over the <i>R</i> isomer. Each sphere represents a perturbed field direction, and its colour represents the magnitude of the perturbation from most catalytic (red) to least (blue), and most selective for the <i>S</i> isomer (red) to least (blue). The arrows represent the optimal field direction (yellow), and the relative magnitude and direction of the molecular dipole of the unperturbed transition state (blue) and the perturbed transition state (pink).	41
3.18 Electron density difference isosurfaces of the non-activated transition state geometry in CPCM ethanol, as perturbed by the optimised a) <i>S</i> selective, b) <i>S</i> anti-selective, and c) catalytic field directions at $ \vec{F}  = 0.1 \text{ V}\cdot\text{\AA}^{-1}$ as per Table 3.7, following an isovalue of 0.0002. The red and blue isosurfaces represent regions of increased and decreased electron density, respectively. The yellow arrow is a representation of $\vec{F}$ .	43
3.19 $\log(k)$ rate constant differences between the catalysed and unperturbed, and <i>S</i> selective and <i>S</i> anti-selective OEEF perturbed pathways, modelled against a series of solvents. Asymptotes have been drawn in for easier comparison of trends.	46
3.20 a) Reduction in barrier heights for the non OEEF-perturbed and for each of the optimised OEEF directions as a function of solvent dielectric constant, relative to the maximum energy at $\varepsilon_r = 0$ . b) Relative differences between the non OEEF-perturbed and OEEF-perturbed results from Figure 3.20a. This plot shows the amount of stabilisation afforded by the CPCM dielectric pertaining to the stabilisation of OEEF induced charge separation, with the added stabilisation of the geometry relaxation.	47
3.21 OEEF directions that result in the maximum separation between the <i>S</i> and <i>R</i> pathways of the derivatised transition state. The grey dots represent the scanned OEEF directions and the arrows denote the OEEF that resulted in the maximum <i>S</i> and <i>R</i> separation for each derivative. The orange group represents $R_1$ and the cyan group represents $R_2$	50

3.22 Electronic energy of the <i>R</i> (red) and <i>S</i> (blue) energy of each derivative in their optimal field, relative to the non OEEF-perturbed derivative's energy. . . . .	52
3.23 Electronic energy of the <i>R</i> (red) and <i>S</i> (blue) isomer of each derivative as perturbed by the $R_1=H, R_2=H$ optimal field, relative to the non OEEF-perturbed derivative's energy. . . . .	52
3.24 a) Electronic energy of the <i>R</i> (red) and <i>S</i> (blue) isomers of all permutations of $R_1, R_2=H, t\text{-Bu}$ , as perturbed by the optimal <i>S</i> selective OEEF for $R_1=H, R_2=H$ , a) relative to their non-perturbed energy. Differences between the energy of the <i>t</i> -Bu derivatised geometries and $R_1=H, R_2=H$ have been plotted in b) to explicitly show the stability afforded by the added polarisability of the bulky groups alone. . . . .	53
3.25 Potential energy of the <i>R</i> (red) and <i>S</i> (blue) isomer of the non derivatised 2'-aminochalcone, with $q_1/q_2 = 0.1, 0$ , or $0.1$ point charges in place of the <i>R</i> groups. . . . .	54
3.26 $\log(k)$ rate constant differences between the catalytic and stereoselective OEEFs for the non-derivatised and $R_1, R_2=\text{NO}_2$ derivatised species of 2'-aminochalcone in $ \vec{F}  = 0, 0.1$ and $0.2 \text{ V}\cdot\text{\AA}^{-1}$ . . . . .	57
A.1 PES scans along the reaction coordinate for all barrierless steps in the various pathways.	xiv
B.1 Reaction trajectories for the relaxed benchmarks performed in Section 3.4 . . . . .	xvii
C.1 Electron density difference isosurfaces following an isovalue of 0.0002 for the optimal $0.1 \text{ V}\cdot\text{\AA}^{-1}$ <i>S</i> selective/ <i>S</i> anti-selective OEEF directions for each of the derivatives, calculated at M06-2X/6-31+G*, solvated in CPCM ethanol. The red and blue isosurfaces represent regions of increased and decreased electron density respectively. The yellow arrow is a representation of the direction of the applied field vector. . . . .	xix
E.1 Reaction trajectories for the benchmarks performed in Section 3.6. . . . .	xxii
E.2 Transition state geometries from the OEEF perturbed benchmarks in Section 3.6 . . .	xxiv

# List of Tables

3.1	Energetic terms added to each benchmarked pathway to normalise them to the non-activated reactant . . . . .	23
3.2	Rate constants ( $\log(k)$ ) for both the intermediate formation reactions and the cyclisation, for each of the six pathways of <b>1</b> → <b>4</b> . Since the non-activated pathway has no intermediate formation step, it has been left blank. . . . .	25
3.3	CHELPG partial charges ( $e$ ) of the bonding atoms of the intermediate geometry of each of the pathways. . . . .	25
3.4	Optimal OEEF directions for catalysis and stereoselection in $V\cdot\text{\AA}^{-1}$ . The <i>S</i> anti-selective field is the <i>S</i> selective field, flipped along the mirror plane for the molecule; the <i>Z</i> axis. . . . .	42
3.5	Rate constants for the relaxed geometry of the non-activated pathway, as perturbed by the identified catalytic, <i>S</i> selective and <i>S</i> anti-selective OEEFs, in comparison to the unperturbed pathway, in a range of solvents. All rates are shown as $\log(k)$ . . . . .	45
3.6	Maximum electronic energy energy differences between <i>S</i> and <i>R</i> isomers of the derivatives of the non-activated pathway, as identified by OEEF scanning. The energy reported as $\Delta\Delta E$ is calculated as $\Delta E(S) - \Delta E(R)$ as perturbed by $\vec{F} = 0.1 V\cdot\text{\AA}^{-1}$ . . . . .	51
3.7	$\log(k)$ rate constants for the cyclisation of both the $R_1, R_2=H$ and $R_1, R_2=\text{NO}_2$ forms of 2'-aminochalcone, both unperturbed and perturbed by catalytic, <i>S</i> selective, and <i>S</i> anti-selective OEEFs. . . . .	56
A.1	Raw $\Delta G^\circ$ from the benchmarking of the reaction pathways in Section 3.1. The blank cells pertain to calculations that were not performed. . . . .	xiii
A.2	raw $\Delta G^\circ$ of the species used top balance the reaction trajectories in Section 3.1. . . . .	xiii
A.3	Transition state imaginary frequencies and calculated transmission coefficients for the intermediate formation and cyclisation steps respectively, for the reaction pathways benchmarked in Section 3.1. . . . .	xiii

B.1	Raw $\Delta G^\circ$ , transition state imaginary frequencies, and transmission coefficients for the benchmarks performed in Section 3.4 . . . . .	xv
D.1	Raw $\Delta G^\circ$ , transition state imaginary frequencies, and transmission coefficients for the benchmarks performed in Section 3.6 . . . . .	xx

# Abstract

Controlling reactivity through means of oriented external electric fields (OEEFs) has grown in interest in the past 30 years, owing to its ability to manipulate the outcome of a reaction without the need for specially designed catalysts. At present, few solvated reactions have been computationally investigated to understand how OEEFs could be used to control stereoselection, particularly with an intent to guide further experimental research. The intramolecular cyclisation of 2'-aminochalcone to aza-flavanone through an aza-Michael addition is a good candidate for OEEF mediated stereocontrol, and as of yet stereoselective synthesis has not been experimentally accomplished. In this research, the influence of directionality and strength of the OEEF, the choice of solvent and derivatisation were explored using density functional theory to better understand how OEEFs could be used to control the rate and stereoselectivity of the reaction. When solvated in ethanol, a catalytic increase in rate constant by a factor of 3.2 and an enantiomeric excess of 99.9% were found to be achievable in appropriate OEEFs of  $|\vec{F}| = 0.2 \text{ V}\cdot\text{\AA}^{-1}$ , with derivatisation found to be a probable method for increasing this further. Future research is planned to be carried out, investigating how to solvate the reaction in specially designed solvents in order to ensure that the reactant stays aligned with an appropriately stereoselective OEEF.

# 1 Introduction

## 1.1 Reaction control through oriented external electric fields

Chemical reactivity can be broadly reduced down to the dynamics of electrons; if one can control the electronic environment, one can control the reactivity. This notion has been at the forefront of chemical research for as long as inductive and resonance effects have been utilised to manipulate the strength of bonds. While the understanding that electrons (as negatively charged particles) could be influenced by an Electric Field (EF) has been around for over a century, the idea of utilising these fields to influence reactivity has only been explored in the past 30 years.

The methods to this approach were initially theoretical in nature and experimentally crude, involving the use of ionic clusters and concentrated salt solutions,<sup>1</sup> however, through the use of early *ab initio* techniques, the mechanisms by which ‘electrostatic catalysis’ could be achieved were able to be more rigorously and precisely investigated. These computational studies in the early 90s sought to understand solvent effects, and more generally the effects of localised EFs on chemical reactions, such as the Friedel-Crafts<sup>2</sup> reaction in which appropriately placed point charges were found to "dramatically lower" the reaction barrier. Further evidence for the direct influence of electrostatic catalysis came from biology, as the concept that within the binding site of an enzyme, an Internal Electric Field (IEF) generated by charged amino acids within the binding site could effectively be creating a pre-ordered environment that would stabilise the substrate’s Transition State (TS).<sup>3</sup>

Through the development of the valence bond (VB) model of chemical reactivity, Sini *et al.*<sup>4,5</sup> discovered that all covalent bonds could be stabilised through the introduction of charge-separated resonance contributors. A bond between atoms A and B could be described by the equation  $[A^+ B^- \longleftrightarrow A-B \longleftrightarrow A^- B^+]$ , with the specific ratio combinations of these resonance contributors

defining how ionic the resulting bond is. In [Equation \(1\)](#) this is described in VB notation, as the superposition (linear combination) of the contributing resonance species ( $A-B$ ,  $A^-B^+$  and  $A^+B^-$ ), with the amount that each resonance form contributes as a coefficient ( $C_1$ ,  $C_2$  and  $C_3$ ). This gives rise to the most stable form of the bond, whose wavefunction ( $\Psi_{A-B}$ ) can be polarised by stabilising one of the ionic resonance species over another.

$$\Psi_{A-B} = C_1(A-B) + C_2(A^-B^+) + C_3(A^+B^-) \quad (1)$$

This theoretical formalism laid the groundwork for further computational research into the field, with Shaik *et al.* continuing to explore the effects of external electric fields (EEF). Initially, they created selectivity between competing nonpolar epoxidation and hydroxylation reactions<sup>6</sup> and later, Meir *et al.*<sup>7</sup> identified that an Oriented EEF (OEEF) applied uniformly across all atoms could afford endo/exo selectivity of Diels-Alder reactions by polarising the TS and allowing for the mixing of new charge-transfer states. As shown in [Figure 1.1](#), this was demonstrated through a model

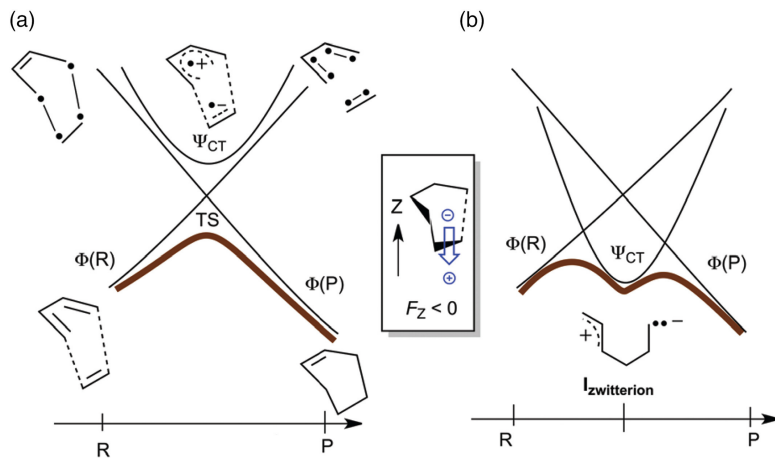


Figure 1.1: Valence bond diagrams of a generic Diels-Alder reaction demonstrating (a) the uncatalysed, concerted pathway and (b) the resulting stepwise pathway with reduced barrier as a product of the stabilisation of the charge-transfer state, by the electric field denoted in the centre box. Reproduced from Stuyver *et al.*<sup>8</sup>

Diels-Alder reaction, where following the concerted cycloaddition, the reaction trajectory was found to be a linear combination of only the mixing of the reactant and product states, resulting in a single transition state. By introducing an electric field that stabilised the polarised Charge Transfer state (CT), a lower energy zwitterionic intermediate would form that reduced

the overall barrier of the reaction.<sup>8</sup> Simply put, the resulting CT state had a much lower energy than the non-polarised TS reducing the barrier of the reaction.

Meir's theoretical exploration was put to the test experimentally by Aragonès *et al.*<sup>9</sup> who used the electric field from a scanning tunnelling microscope (STM) to catalyse a model Diels-Alder cycloaddition. This was accomplished by tethering the dienophile and diene to the STM plate and tip, respectively in such a way as to align the forming bonds with the STM field direction. The tip and plate were brought into proximity of each other and the difference in potential between the two formed an OEEF which passed through the reaction axis of the cyclisation. As shown in [Figure 1.2](#), depending on the strength and direction in which the potential bias was applied, based on the VB diagrams in [Figure 1.1](#) a different polarised TS would be stabilised. In the absence of the field and at low field strengths, the natural polarity of the molecule resulted in species I being the main resonance contributor to the superposition of the TS. The direction of the field could either stabilise or destabilise this resonance form changing the composition of the TS and thus the barrier height of the reaction. At stronger field strengths, species III was also able to be stabilised, and since both resonance contributors became accessible, both field directions were seen to be catalytic. While this research was incredibly valuable as an experimental proof of concept for the progression of the field, being the first practical example of exclusively electrostatic catalysis, the impracticality of having to tether the reactants to align with the field left it unsuitable for any kind of reaction on scale.

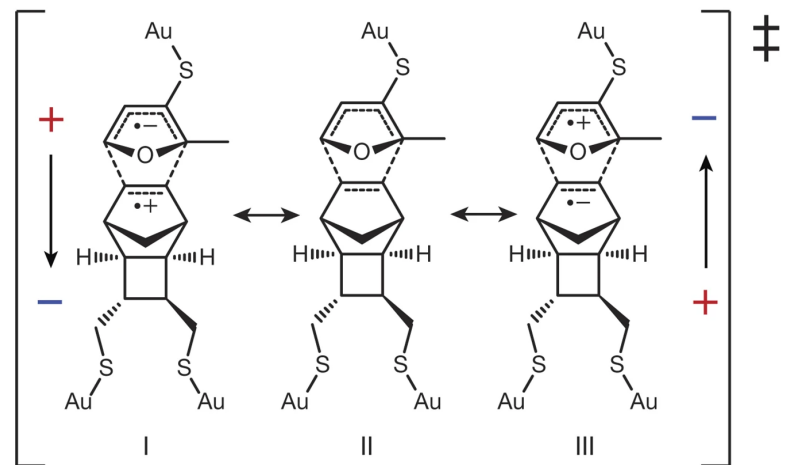


Figure 1.2: Polarised (I and III) and non-polarised (II) transition states of the model Diels-Alder reaction, used in the STM OEEF catalysis experiments of Aragonès *et al.*<sup>9</sup>

and direction in which the potential bias was applied, based on the VB diagrams in [Figure 1.1](#) a different polarised TS would be stabilised. In the absence of the field and at low field strengths, the natural polarity of the molecule resulted in species I being the main resonance contributor to the superposition of the TS. The direction of the field could either stabilise or destabilise this resonance form changing the composition of the TS and thus the barrier height of the reaction. At stronger field strengths, species III was also able to be stabilised, and since both resonance contributors became accessible, both field directions were seen to be catalytic. While this research was incredibly valuable as an experimental proof of concept for the progression of the field, being the first practical example of exclusively electrostatic catalysis, the impracticality of having to tether the reactants to align with the field left it unsuitable for any kind of reaction on scale.

With sufficient experimental evidence and a theoretical understanding of the effect of OEEFs, Shaik

*et al.* formalised the "governing effects and rules for electric-field effects on chemical reactivity",<sup>10</sup>

here on referenced as the "rules". They are as follows:

Rule i) An EEF that is oriented along a "bond axis" will polarise the bond, favouring one of the ionic species ([Equation \(1\)](#)), eventually cleaving it heterolytically. As this polarisation occurs, the bond dipole increases, causing it to interact more strongly with the OEEF, stabilising the species in the process.

Rule ii) Every reaction possesses a "reaction axis" which follows the flow of electrons from reactant to product, through the TS. In the view of an organic chemist, this follows the flow of the "curly arrows".

Rule iii) Applying an OEEF along the "reaction axis" will stabilise the TS by increasing the bond ionicity (as per [rule \(i\)](#)), and symmetry of the HOMO-LUMO overlap of the transition state allowing, will encourage mixing of the charge-transfer states.

Rule iv) A molecule that either possesses a dipole moment or that is polarisable, will experience a torque that will cause it to rotate to align with a sufficiently strong OEEF. This is explored further in [Section 1.2](#).

Beyond the four rules laid out by Shaik, electrostatic control of reactions can be extended, to create discrimination between the reaction pathways that form different isomers. Wang *et al.*<sup>11</sup> demonstrated this theoretically in an *ab initio* study by using OEEFs to control the product formation of a Diels-Alder cycloaddition of polar, asymmetric ethene derivatives with cyclopentadiene (see [Figure 1.3](#)). Wang showed that by orienting the OEEF perpendicular to the reaction axis, discrimination could be created between the *endo* and *exo* pathways, or the *R* and *S* pathways, depending

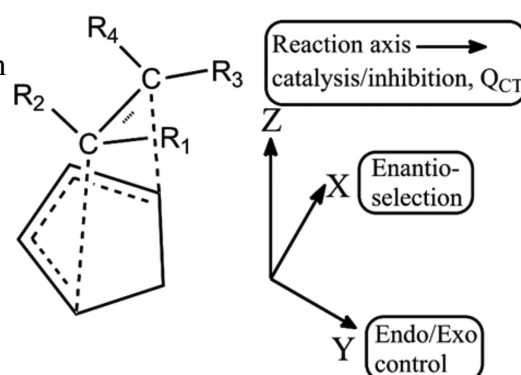


Figure 1.3: OEEF direction and the resulting effect on the reaction trajectory for the Diels-Alder cyclisation of an asymmetrical ethene derivative into cyclopentadiene. Reproduced from Wang *et al.*<sup>11</sup>

on the chosen cardinal direction. In the case of enantioselectivity, this discrimination occurred due to the OEEF in the positive X direction destabilising the *R* transition state and stabilising the *S* transition state causing a  $44.4 \text{ kJ}\cdot\text{mol}^{-1}$  difference at  $F_X = 0.25 \text{ V}\cdot\text{\AA}^{-1}$  ( $F_X$  denoting the X component of the cartesian vector  $\vec{F}$  of the OEEF). When the OEEF was flipped to point in the negative X direction, the selectivity favoured the *R* pathway over the *S* pathway with the same magnitude of separation between the two.

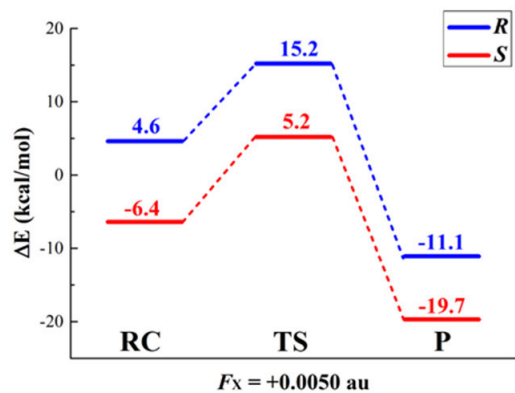


Figure 1.4: Resulting *R* and *S* reaction pathways of the asymmetric Diels-Alder reactions from Wang *et al.*,<sup>11</sup> as perturbed by an OEEF of  $F_X = 0.005 \text{ au}$  ( $\sim 0.26 \text{ V}\cdot\text{\AA}^{-1}$ )

transition states. This discrimination occurred to all species in the reaction trajectory equally and thus had no effect on the barrier heights of the reactions, as shown in Figure 1.4. Selection occurred through discrimination between the energy of the reactant pre-complexes which could easily break apart and re-form to produce the lowest energy species as per Boltzmann statistics.

This enantioselection was the result of the OEEF pushing the electron density from one end of the molecule, through the ethylene bond to the other, depending on the direction of  $F_X$ . Since the ethene was asymmetric, the more electronegative end of the molecule was more receptive to the electron density than the other, leading to a discrimination between the direction of the polarisation of the ethylene bond and the resulting energy of the *R* and *S*

Formal rules for OEEF controlled enantioselection are highly dependent on the specifics of the reaction. Therefore general rules cannot be made to characterise their behaviour beyond the non-specific:

Rule v) ‘Control over the isomeric products of a reaction will likely come as the result of an OEEF oriented perpendicular to the reaction axis, and will not typically be associated with a net catalytic benefit.’

## 1.2 Extending the use of OEEFs to solution

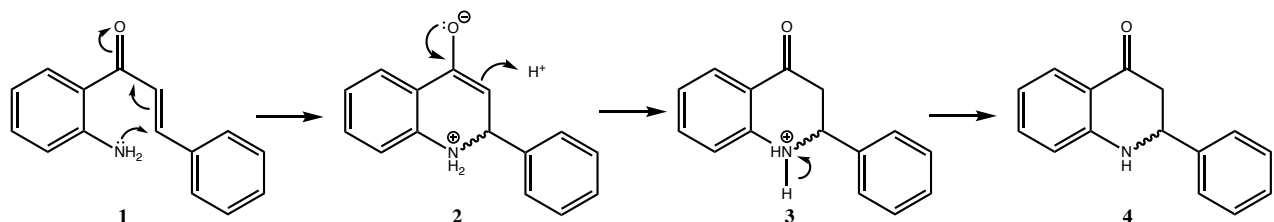
While the STM experiments of Aragonès *et al.*<sup>9</sup> were conveniently able to fix the reactants in the correct orientation to ensure that the OEEF passed through the reaction axis, reactions typically occur in solution making the adoption of the required geometry in relation to an OEEF far more challenging. Following rule (iv), however, when allowed to rotate freely the reactant will align itself with the OEEF according to its dipole moment.<sup>10,12</sup> The amount of stabilising energy that is obtained from the OEEF can be quantified through the relationship  $\Delta E = 20.7\vec{F} \cdot \vec{\mu}$  (kJ·mol<sup>-1</sup>), where  $\vec{F}$  is the EF strength (in V·Å<sup>-1</sup>) and  $\vec{\mu}$  is the dipole moment (in Debye). The constant 20.7 is a unit conversion factor from J to kJ·mol<sup>-1</sup>. If the OEEF strength, or the magnitude of the dipole moment is strong enough, the stabilisation energy can overcome the rotational kinetic energy of the molecule, preventing it from freely rotating.<sup>10,13</sup> If, however the electric field is too strong, the corresponding ionic species (Equation (1)) of bonds within the molecule will be stabilised more than the covalent forms, causing the molecule to be cleaved as per rule (i).<sup>10,12</sup>

This ability for a solvent as a bulk medium to stabilise the separation of charges within its continuum is quantified as its dielectric constant (relative permittivity), which is a relative measure of its ability to reduce electrostatic forces over a distance. It is generally considered to be a function of the solvent molecule's dipole, charge, polarisability, and bulk structure.<sup>14</sup> As the polarisation of solutes from an OEEF is inherently a process that increases the magnitude of opposing charges across a distance (a dipole), the ability of the solvent to stabilise this charge separation is fundamental to the stabilisation of the polarised solute. Solvents with a large dielectric constant will better stabilise highly polarised species than those with small dielectric constants, making them more susceptible to the OEEF's perturbation. This separation of charges is accomplished by the solvent molecules rearranging themselves to align in a way to form an internal electric field that cancels out the field produced by the charged solute, minimising the energy of the system. This process is not specifically

limited to the stabilising solute, however, and the solvent molecules will also produce an IEF that will oppose out an EEF.<sup>12</sup> As a result, a trade-off must be made to choose a solvent which will maximise stabilisation and solubility of the polarised species, while minimising screening of the OEEF.<sup>15</sup>

### 1.3 The cyclisation of 2'-aminochalcone

The cyclisation of 2'-aminochalcone (**1**) to form aza-flavanone (**4**) is a simple example of an intramolecular aza-Michael conjugate addition in which the nucleophilic lone pair electrons from the nitrogen attack the adjacent  $\alpha$ ,  $\beta$ -unsaturated ketone at the electrophilic  $C_\beta$ , pushing the electrons up the conjugated system and onto the receptive ketone oxygen. If an appropriate electrophile is present in solution, such as a free proton, the electron density can flow back down from the oxygen, allowing the addition of the electrophile into  $C_\alpha$ . This cyclisation creates a new stereocentre at  $C_\beta$ , which under standard conditions will form as a racemic mixture of the two stereoisomers, as shown in [Scheme 1](#).



Scheme 1: Uncatalysed pathway for the aza-Michael addition of 2'-aminochalcone to form aza-flavanone

The historical method for performing this reaction is to combine **1** in varying ratios of hot glacial acetic acid and phosphoric acid for 20 minutes, which produces yields of up to 78%.<sup>16</sup> Through the push to greenify the reaction, Lewis base catalysts were identified as the gold standard, with 2.7 mol% piperidine/KOH affording > 99% yield in 5 minutes at room temperature, using water as a solvent.<sup>17</sup>

While the non-enantioselective reaction has been thoroughly optimised, in order to select for a particular stereoisomer, the reaction requires the use of chiral acids and harsh solvents. One such example from Saito *et al.*<sup>18</sup> produces racemic **4** bound to a BINOL derived chiral phosphoric acid, which can

be subsequently separated using column chromatography to give a 93% enantiomeric excess from a 95% yield. While this method of enantioselection is incredibly inefficient (as fundamentally, half of the product can be considered waste), it also requires the use of 1:1 benzene:*n*-hexane as solvent. This significantly restricts the industrial capabilities of this method, due to its highly hazardous nature.<sup>19</sup>

## 1.4 Theoretical methodology of reaction rates

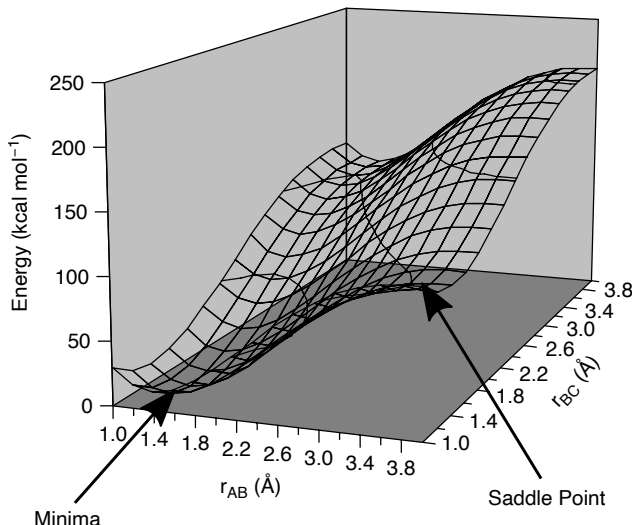


Figure 1.5: Example potential energy surface of hypothetical molecule A–B–C, displaying the degrees of freedom of the length of bonds A–B and B–C on the X and Z axes, with energy being displayed on the Y axis, reproduced from Cramer.<sup>20</sup>  
the PES (configuration of atoms) to another, it will traverse the PES along the lowest energy pathway, as afforded by the kinetic energy of the system.

The Potential Energy Surface (PES) can be considered an *n*-dimensional plane, with each dimension representing a degree of freedom of the molecule, and the potential energy of the molecule represented as the surface's topology, as demonstrated in Figure 1.5. Any stable configuration of the system will therefore reside in an energetic minimum on the PES, and the extent that the system emerges out of the well will be determined by its kinetic energy. For any chemical system to move from one minimum on

Transition State Theory (TST) and the Eyring-Polanyi equation use the PES model to make the assumption that a reaction will go from one minimum to another across a "saddle point", where all degrees of freedom except for one are at an energetic minimum. Statistical mechanics defines that configurations that a system adopts can be described as a Boltzmann population distribution, and that this distribution is based on the potential energy of each respective configuration. TST follows the

logic that the reactants and the TS will be in equilibrium with each other, and that the rate at which a reaction occurs will be directly proportional to the relative energy difference between the reactant and transition state; *i.e.* the barrier height. This is shown in the basic form of the Eyring-Polanyi equation, [Equation \(2\)](#).<sup>14,20</sup> The rate constant of a reaction pertaining to the system moving between two minima without an energetic barrier can be described by the relationship [Equation \(3\)](#).<sup>14,20</sup> Since TST assumes that an equilibrium is reached between the reactant and transition state of a single step, the theory cannot faithfully account for multi-step reactions, where intermediates are often short-lived, and equilibrium will not be reached. Rate constants for multi step reactions can be approximated as the product of rate constants for each individual step.

$$k^\ddagger = \left( \frac{k_b T}{h} \right) \exp \left( \frac{-\Delta H^{\ddagger}}{RT} \right) \quad (2)$$

$$k = \exp \left( \frac{-\Delta H^\circ}{RT} \right) \quad (3)$$

TST is a convenient method in that it is computationally simple to calculate the potential energy of a system, however it is not guaranteed that the maximum on the  $\Delta E$  PES will result in a maximum on the  $\Delta G^\circ$  ‘free energy surface’ of the system, and thus the barrier may in fact be higher than TST would predict. It also assumes that any reactant species will only cross the barrier a single time to reach the product. Variational Transition State Theory (VTST) reduces these issues by taking the the Eyring-Polanyi equation ([Equation \(2\)](#)), and using the maximum energy from the ‘Gibbs free energy surface’ of the reaction coordinate ( $\Delta G^{\ddagger}$ ) in place of the potential energy barrier ( $\Delta H^{\ddagger}$ ) to provide a more accurate depiction of the reaction rate constant.

The approximations made by TST and VTST are effective at describing the rate of reactions that are thermally activated, as their Boltzmann population distribution will largely consist of high energy

species that are capable of traversing the activation barrier. At lower temperatures, and with lighter elements, however, the effects of quantum tunnelling can start to predominate.<sup>20</sup> In this context, quantum tunnelling can be described as the ability for the reactants to pass *through* the reaction barrier rather than crossing over it. It is a fundamentally quantum phenomenon, whose probability will be dependent on the height and cross-sectional shape of the barrier, as well as the mass of the particles and the temperature of the system. Tunnelling is significantly more likely to happen for proton transfers, where the tunnelling particle has a wavelength comparable to the relatively narrow barrier width. The Eyring-Polanyi equation can be modified to account for this, with the addition of the transmission coefficient term ( $\kappa_{(T)}$ ), as can be seen in the VTST example in [Equation \(4\)](#).

$$k^\ddagger = \left( \kappa_{(T)} \frac{k_b T}{h} \right) \exp \left( \frac{-\Delta G^{\circ\ddagger}}{RT} \right) \quad (4)$$

While multiple approximations have been made to quantify this phenomena, the Skodje-Truhlar tunnelling coefficient approximation<sup>21</sup> is considered to be one of the most accurate, for its relative accessibility<sup>22</sup> and lack of extra computation required. At its core, it considers three terms; the imaginary component of the frequency pertaining to the reaction coordinate ( $\text{Im}(\nu^\ddagger)$ ), the activation energy ( $V^\ddagger$  as  $(\Delta E + ZPVE)^\ddagger$ ), and the symmetry of the barrier ( $V$  as  $\max([( \Delta E + ZPVE)_{prod} - (\Delta E + ZPVE)_{reac}], 0)$ ). All of these components can be conveniently obtained from the same thermodynamic corrections that are used to calculate  $k^\ddagger$  from the TST and VTST approaches and the transmission coefficient can be calculated using [Equation \(5\)](#).

$$\kappa_{(T)} = \begin{cases} \frac{\beta}{\beta-\alpha} \left[ \exp \left( (\beta - \alpha)(\Delta V^\ddagger - V) \right) - 1 \right] & , \quad \alpha \leq \beta \\ \frac{\beta\pi/\alpha}{\sin(\beta\pi/\alpha)} - \frac{\beta}{\beta-\alpha} \exp \left( (\beta - \alpha)(\Delta V^\ddagger - V) \right) & , \quad \alpha \geq \beta \end{cases} \quad (5)$$

$$\alpha = \frac{2\pi}{h\text{Im}(\nu^\ddagger)} \quad \beta = \frac{1}{k_B T}$$

## 1.5 Computational chemistry

Computational chemistry is the application of fundamental physical and mathematical methods to solve chemical problems, utilising computational resources to calculate the otherwise prohibitively complicated equations involved.

One such physical theory used by computational chemists is Quantum Mechanics (QM), which aims to solve the time independent Schrödinger equation ( $\hat{H}\Psi = E\Psi$ ) in order to better understand the nature of the chemical system. *Ab initio* methods accomplish this by optimising a linear combination of primitive gaussian functions, representing the electrons in the system, to form its wavefunction ( $\Psi$ ). This can then be used with an appropriate hamiltonian ( $\hat{H}$ ) to determine the overall energy of the system ( $E$ ). The optimisation of the wavefunction is an iterative process in which each electron's representative functions are optimised against the "mean field" of the electrostatic contributions of all other electrons in the system, until the solution reaches the specified convergence criteria. This mean field approach accounts for 99% of the system's energy, however it neglects to account for the dynamic interactions between electrons, (electron correlation). Since the nature of chemical reactivity is the dynamic movement of electrons, this 1% error has the most influence on the energy of the reaction itself. When higher levels of theory are made to mitigate this issue, these calculations can be highly accurate, however scale in computational cost much more rapidly with the size of the chemical system.<sup>20</sup>

Rather than optimising the wavefunction directly, Density Functional Theory (DFT) optimises the electron density of the system to determine its energy. This approach scales far more favourably and more explicitly accounts for the correlation energy than more affordable *ab initio* methods. The nature of DFT, however, means that the solutions that emerge are fundamentally based on parameterisation and approximation, as no universal relationship between the electron density and the energy is known.

Therefore, DFT methods are only as accurate as the approximations that the methods utilise.<sup>20</sup> It can be said that DFT solves approximate forms of the Schrödinger equation exactly, whereas *ab initio* methods solve the exact form of the Schrödinger equation approximately.

### 1.5.1 Thermodynamic corrections to the internal energy

While *ab initio* and DFT approaches are fundamentally tools that calculate the electronic energy of a molecule, for the output energies to be chemically meaningful in a real world context, it is required to calculate the thermodynamic properties of the system. This is accomplished by taking a starting geometry and measuring the gradient of the PES, either analytically, or by finite differences; perturbing every degree of freedom (DoF) and measuring the resultant energy. Since the first derivative of the PES gives the forces involved for every DoF, these differences can be converted into vibrational frequencies using the harmonic oscillator approximation for larger frequencies, and their sum used to calculate the zero point vibrational energy (ZPVE) as shown in [Equation \(6\)](#). This matrix of gradients is known as the Hessian. To determine the internal energy of the system, the ZPVE is added on to the electronic energy, with thermal corrections to the vibrational, rotational and translational energy, for DoF that become accessible at temperatures above 0 K ([Equation \(7\)](#)).

$$E_{ZPVE} = \frac{1}{2} \sum_i h\nu_i \quad (6)$$

$$\Delta U^\circ = E^\circ + E_{ZPVE} + E_{vib} + E_{trans} + E_{rot} \quad (7)$$

$$\Delta H^\circ = \Delta U^\circ + nRT \quad (8)$$

$$\Delta G^\circ = \Delta H^\circ + T\Delta S \quad (9)$$

$$\Delta S = \Delta S_{trans} + \Delta S_{rot} + \Delta S_{vib} \quad (10)$$

Assuming 1 mole of the system in question, the standard definition of  $\Delta H^\circ = \Delta U^\circ + PV$  can be used, along with the statistical mechanical relationship  $PV = nRT$  to give [Equation \(8\)](#), providing the enthalpy of the system. To obtain the Gibbs free energy of the system, as per [Equation \(9\)](#), the entropy must be calculated, as the sum of rotational, vibrational, and translational entropic terms, as per [Equation \(10\)](#). These are calculated using standard thermodynamics of an ideal gas, under the rigid rotor and harmonic oscillator approximations.<sup>14,20</sup>

### 1.5.2 Continuum solvation models

Solvation approaches in computational chemistry can be broken down into two broad categories; implicit, and explicit solvation. Explicit solvation involves modelling the bulk by explicitly placing solvent molecules around the solute, and including them as a part of the calculation. Since the scaling of QM calculations is exponential with the number of basis functions, explicit solvation methods are typically considered too expensive to be practically usable for the vast majority of systems.

Implicit solvation models take a different approach and treat the solvent as a continuum, based on its bulk properties. The most common of these is the Conductor like Polarisable Continuum Model<sup>23</sup> (CPCM) which, based on the size of the solvent molecule, places the solute in a cavity within the bulk and treats the surface of the cavity as a pure conductor ( $\varepsilon = \infty$ ). Using the specified dielectric constant of the solvent, it then scales back the screening to more appropriately represent the permittivity of the solvent and subsequently allows the solute to be polarised. Through this process, the CPCM method breaks down the solvation free energy into the energy required to form the solvation cavity, the electrostatic stabilisation afforded by the charge screening process, and the energy associated with the change in dispersion within the bulk solvent.<sup>24</sup> While the conductor scaling approach is an effective method for modelling high dielectric solvents such as water, it is less effective for low dielectric solvents, such as *n*-hexane.<sup>25</sup>

An extension to the CPCM model is that of the Solvent Model based on Density (SMD), which takes the electrostatic term from CPCM and calculates a new cavity-dispersion solvent-structure (CDS) term based on the charge density of the solute to account for the rest of the solvation free energy. It calculates the CDS term as the sum of short-range interactions between the solute and the first solvation shell, and as such uses extra parameters for the bulk surface tension, hydrogen bonding acidity and basicity, aromaticity and halogenicity.<sup>25</sup> When the system being studied is similar to the training data set which was used to parameterise the SMD model (as is the case for common organic reactions in conventional solvents), it can be considered a significant improvement over CPCM.

## 1.6 Research objectives

Following the work of Shaik *et al.*,<sup>10</sup> this project aims to use computational chemistry to investigate the cyclisation of 2'-aminochalcone to form aza-flavanone under the influence of OEEFs. The ultimate goal of this research is to both identify whether the reaction is suitable for studying under the effects of OEEFs, and to act as a "theoretical roadmap" to make better educated decisions for future theoretical and experimental studies into the effects of OEEFs on this reaction.

The cyclisation of 2'-aminochalcone to form aza-flavanone was chosen as the subject of this study for a number of reasons. Firstly, the synthesis of the reactant is a simple process and can be performed using off-the-shelf reagents. Secondly, due to the change in conjugation that occurs from the **1** → **2** → **3**, the kinetics of the reaction can be easily monitored using UV-Vis spectrometry, or NMR spectroscopy. Thirdly, since the reaction is unimolecular, there are fewer factors that can influence its kinetics. This particular point is quite important when considering that the rate of intermolecular reactions would also be influenced by OEEF-induced diffusion through the solvent, and that having multiple constituents within a reaction would make aligning them with the OEEF significantly more

difficult. Finally (and most importantly), the reaction forms a new chiral centre without any pre-existing chirality present in the reagents, making stereoselection significantly more impressive as a feat.

As a part of this theoretical roadmap, this research aims to:

- Understand the catalytic processes involved in performing the reaction and identify the most appropriate pathway for studying the reaction under the influence of an OEEF.
- Identify how the reaction can be controlled using OEEFs to produce both catalysis and enantioselection, to quantify these effects, and to understand their mechanistic processes.
- Investigate how this OEEF mediated reaction control could be influenced by the addition of localised electric fields, through charged functionality.

## 2 Computational details

For the majority of this work the chosen choice of theory was the M06-2X<sup>26</sup> DFT functional with the double- $\zeta$ , singly-augmented, Pople basis set with added diffuse functions (6-31+G\*)<sup>27,28</sup>. While the use of Pople basis sets is somewhat outdated, M06-2X was parameterised to work with small basis sets and has been shown to work effectively with this family of basis sets.<sup>26</sup> Through rigorous benchmarking, the combination of M06-2X/6-31+G\* has been identified as one of the best performing functional/basis set combinations for modelling the perturbative effects of electric fields with a mean absolute deviation of 0.08 kJ·mol<sup>-1</sup><sup>9</sup> and has become the standard for modelling these systems.<sup>9</sup> In other portions of this project M06-2X has been used in conjunction with the more modern and robust Dunning's augmented, polarised, triple- $\zeta$  basis set (aug-cc-pVTZ),<sup>29,30</sup> to afford better non-OEEF perturbed results, while still keeping the computational cost relatively low. Errors for this method have been benchmarked to 0.077 Å for geometry optimisations and 10.75 kJ·mol<sup>-1</sup> for barrier heights.<sup>31</sup>

For accurate benchmarking of non-OEEF perturbed systems,  $\omega$ B97M-V<sup>32</sup> was chosen as it has been shown to generally be the best performing DFT functional for geometry optimisations and barrier heights<sup>31,33</sup> with RMSD errors of 0.014 Å and 7.0 kJ·mol<sup>-1</sup> respectively.<sup>31</sup> In this research it was paired with Ahlrichs' quadruple- $\zeta$ , doubly polarised basis set (Def2-QZVPP),<sup>34</sup> as this family of basis sets have been parameterised<sup>35</sup> to work effectively with the RI-J approximations<sup>36</sup> that allow for significant speedups in the calculation of the coulombic terms of the DFT functional. These approximations introduce minimal errors of  $\sim$ 0.2 kJ·mol<sup>-1</sup> with hybrid DFT methods while affording decreases in computational cost of more than 8 times, making this method attainable for the systems studied in this research. All thermodynamic calculations throughout this research were calculated using M06-2X/6-31+G\* with CPCM solvation for OEEF perturbed systems and  $\omega$ B97M-V/Def2-QZVPP with SMD solvation for non-OEEF perturbed systems. For standard state conditions, a temperature of 298.15 K was used for all thermodynamic calculations (except where otherwise stated) and all

subsequent calculations assume 1 M concentrations.

For non-OEEF perturbed, high level energetic calculations where high level thermodynamic calculations were not required,  $\omega$ B97M-V was used in conjunction with Ahlrichs' triple- $\zeta$ , singly polarised basis set with added diffuse functions (Def2-TZVPD),<sup>34</sup> with a slightly smaller integration grid. These modifications came with an associated RMSD error of 0.018 Å for geometry optimisations and 7.4 kJ·mol<sup>-1</sup> for energetics, such as PES scans.<sup>31</sup>

Throughout this research, errors have mostly been mitigated due to the use of relative energies and energetic differences, rather than using absolute energies alone. The DFT functionals chosen have all been shown to be robust and are often used as benchmarking points of reference in themselves.<sup>37</sup>

For all calculations involving the use of OEEFs, a tradeoff had to be made between choosing an affordable level of theory that would best describe the perturbative effects of the OEEF and also accurately representing the barrier heights of the system. While it could be assumed that more robust methods, such as  $\omega$ B97M-V would accurately represent both, given that the field of electrostatic catalysis is relatively new, few benchmark studies have been performed to verify this. Those performed by Aragonès *et al.*<sup>9</sup> and Gryn'ova *et al.*<sup>38</sup> had to be assumed representative of the systems studied in this work, due to time and resource limitations.<sup>39</sup> As such, any and all kinetic and thermodynamic calculations performed on systems perturbed by OEEFs can only be considered to represent the change in rate as a result of the OEEF and should not be considered qualitative for absolute kinetics. This is made even more prevalent by the recognition that in the Eyring-Polanyi equation, the rate constant is proportional to the exponent of the free energy, so very small changes in the energy result in very large changes in the rate, with 5.7 kJ·mol<sup>-1</sup> equating to an order of magnitude difference in rate constant at room temperature. Throughout this work, all rate constants have been reported

specifically as  $\log(k)$ , for the sake of simplicity.

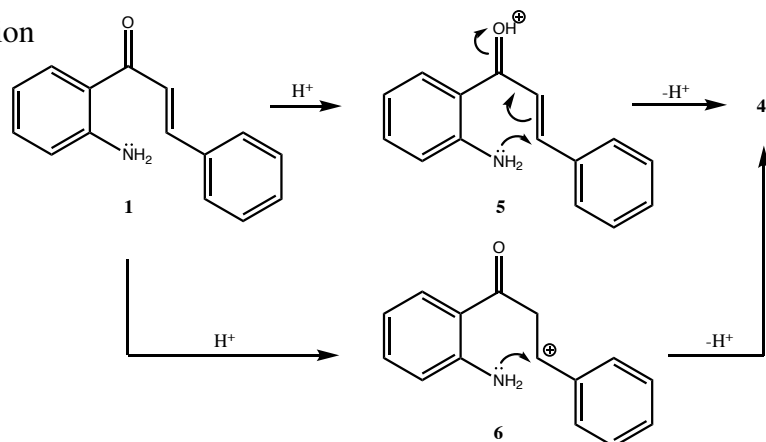
A full breakdown of all the calculation details for all the jobs performed can be found in [Appendix F](#).

It should be noted that throughout this work, all OEEF directions will be presented using the Gaussian<sup>40</sup> notation, which has the vector pointing from negative to positive, which has become standard in the field of electrostatic catalysis. This is contrary to conventional physics notation which describes the vector pointing from positive to negative as has been used throughout this work for molecular dipoles. This has the effect that when aligned, the molecular dipole points in the same direction as the OEEF.

### 3 Results and discussion

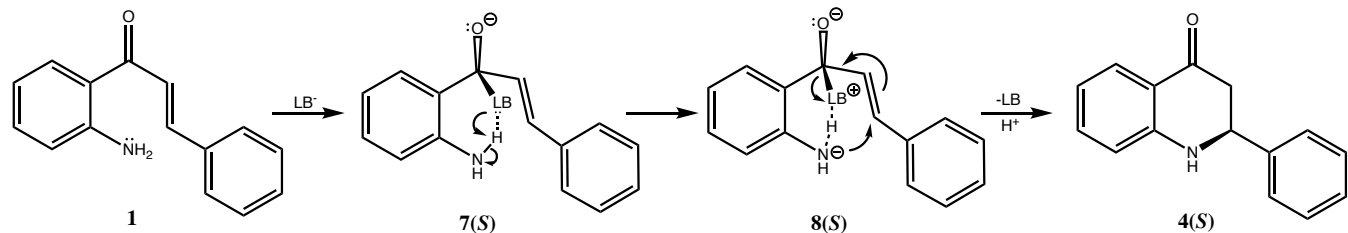
#### 3.1 Pathway selection

For the reaction of **1** → **4**, apart from the non-catalysed pathway, published mechanisms were only available for the Brønsted acid activation.<sup>41</sup> Two potential pathways were theorised (Scheme 2), the first being activated through protonation of the ketone (**5**) and the second through protonation of C<sub>α</sub>, producing C<sub>β</sub><sup>+</sup> (**6**). These pathways will be identified as ‘Brønsted acid 1’ and ‘Brønsted acid 2’, respectively. The Lewis base pathway was also known to be highly effective,<sup>17</sup> however the specific mechanism did not appear to have been fully elucidated. For the ‘Lewis base’ pathway in this research, the nucleophile was assumed to attach to the carbonyl carbon, forcing the carbonyl π electrons onto the oxygen, as shown in Scheme 3.



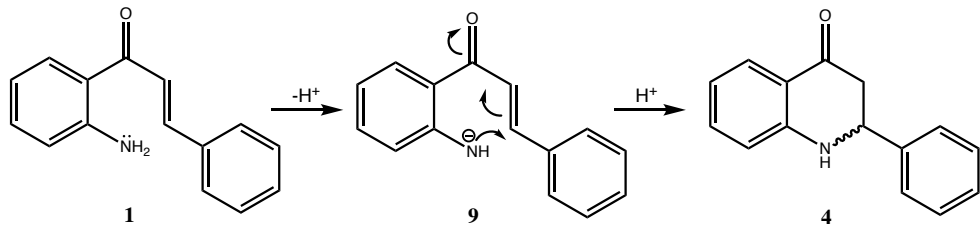
Scheme 2: Brønsted acid catalysed pathways 1 (top) and 2 (bottom) of **1** → **4** as suggested by, and recreated from Bunce and Nammalwar<sup>41</sup>

Lewis base pathway was also known to be highly effective,<sup>17</sup> however the specific mechanism did not appear to have been fully elucidated. For the ‘Lewis base’ pathway in this research, the nucleophile was assumed to attach to the carbonyl carbon, forcing the carbonyl π electrons onto the oxygen, as shown in Scheme 3.



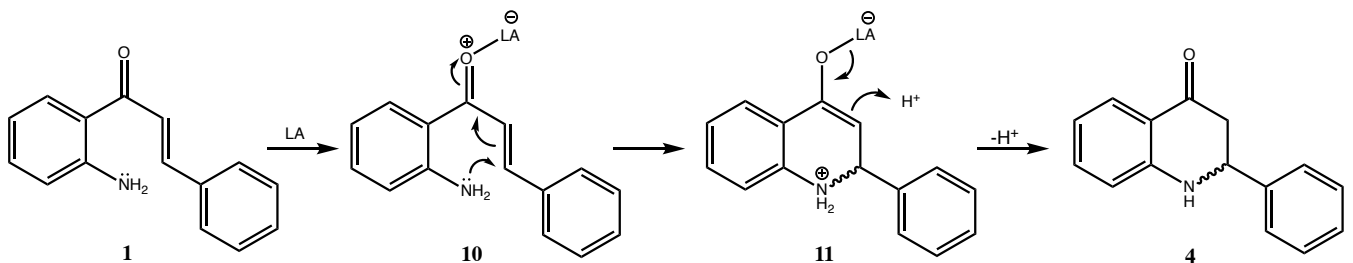
Scheme 3: Theorised Lewis base pathway for the aza-Michael addition of 2'-aminochalcone to form aza-flavanone

It had been mentioned by Tőkés and Janzso<sup>16</sup> that the reaction could also be catalysed using a "strong base," so a ‘Brønsted base’ pathway was devised in which one of the labile amine protons was removed, giving the nitrogen a formal negative charge, as shown in Scheme 4.



Scheme 4: Theorised Brønsted base pathway for the aza-Michael addition of 2'-aminochalcone to form aza-flavanone

For completeness, a ‘Lewis acid’ pathway was devised in which BF<sub>3</sub> was used as a Lewis acid (as shown in Scheme 5), similarly to the addition of a proton into the oxygen as per the Brønsted acid 1 pathway.



Scheme 5: Theorised Lewis acid pathway for the aza-Michael addition of 2'-aminochalcone to form aza-flavanone

To assess the theoretical performance of each of the pathways, the *S* isomer of the reactant, intermediate and cyclisation product of each of pathway was initially built with Avogadro<sup>2</sup> (1.94.0),<sup>42</sup> and was optimised at M06-2X/aug-cc-pVTZ in ORCA,<sup>43</sup> using CPCM<sup>23,24</sup> ethanol. This geometry was subsequently refined and thermodynamic calculations were performed at 298.15 K, using  $\omega$ B97M-V/Def2-QZVPP with SMD<sup>25</sup> ethanol for solvation.

For finding the transition states, ‘nudged elastic band’ calculations were performed to find the TS geometry through interpolation between the reactant and intermediate, and intermediate and cyclisation product geometries, before being optimised to a saddle point in ORCA at M06-2X/aug-cc-pVTZ with CPCM ethanol. The optimised TS geometries were subsequently refined with  $\omega$ B97M-V/Def2-QZVPP in SMD ethanol, before being used to calculate thermodynamic energies as per the same method for

the product, intermediate and reactant. Where barrierless reactions were suspected, the PES along the reaction coordinate was scanned using  $\omega$ B97M-V/Def2-TZVPD in ORCA to confirm the absence of a barrier. These scans were performed by holding the reaction coordinate distance at fixed values while optimising the rest of the structure around it. Increments of 0.05 Å along the reaction coordinate were scanned, from their covalently bonded distance to a distance at which the bond would be completely dissociated. If the energetic pathway between bonded and dissociated had no intermediate maxima, the reaction was considered to be barrierless. These PES scan can be found in [Appendix A](#).

Finding the transition state geometries of the Lewis base pathway proved significantly more difficult and required the use of Hessian guided optimisations, which involved performing thermodynamic calculations at 298.15 K for each optimisation step and using the calculated force constants to guide to optimisation algorithm. These were performed in ORCA at  $\omega$ B97M-V/Def2-TZVPD in SMD ethanol. Thermodynamic calculations to obtain benchmarking results were performed in ORCA as per the other transition states.

From the thermodynamic calculations benchmarking the energy of the six potential pathways, the energies were made relative to the non-activated reactant. For the Brønsted acid pathways, this was accomplished by adding on the  $\Delta G^\circ$  of  $\text{H}_3\text{O}^+$  calculated at the same level of theory to the non-activated reactant, and adding on the  $\Delta G^\circ$  of  $\text{H}_2\text{O}$  to all the states in the Brønsted acid pathways. The corrected non-activated reactant  $\Delta G^\circ$  was then subtracted from the Brønsted acid pathways to give the relative energy with respect to the non-activated pathway. This process was repeated with different corrective terms for each pathway, as shown in [Table 3.1](#). The  $\Delta G^\circ$  for each of transition state 1 was not modified in any way, since they explicitly included all the components of the cyclisation pathways, and in the case of the Brønsted pathways, explicitly used  $\text{H}_2\text{O}$  and  $\text{H}_3\text{O}^+$  as proton acceptors and donors.

Table 3.1: Energetic terms added to each benchmarked pathway to normalise them to the non-activated reactant

Pathway	Added to non-activated reactant	Added to cyclisation pathway
Brønsted acid 1/2	$\text{H}_3\text{O}^+$	$\text{H}_2\text{O}$
Brønsted base	$\text{H}_2\text{O}$	$\text{H}_3\text{O}^+$
Lewis Acid	$\text{BF}_3$	-
Lewis Base	piperidine <sup>-</sup> ((CH <sub>2</sub> ) <sub>5</sub> N <sup>-</sup> )	-

The choice to use water to balance out the protonation states was made, as without any electrons in the H<sup>+</sup> ion, it is impossible to calculate its energy using standard quantum mechanical methods, so the  $\text{H}_2\text{O} + \text{H}^+ \rightleftharpoons \text{H}_3\text{O}^+$  equilibrium was used in conjunction with Hess' law. The difference between the H<sub>2</sub>O and H<sub>3</sub>O<sup>+</sup> energies can be considered that of the H<sup>+</sup> ion, affording an easy way to obtain the proton energy through thermodynamic cycles. This is a commonly used approach where energetics of protonation are of significance, such as for the determination of  $pK_a$ . While experimental values could be used to model just the H<sup>+</sup> energy, since explicitly modelled, participating H<sub>2</sub>O and H<sub>3</sub>O<sup>+</sup> were used for certain states in the reaction trajectory, this allowed for the cancellation of methodological errors.<sup>44</sup>

The relative energies of each pathway were subsequently plotted in [Figure 3.1](#).

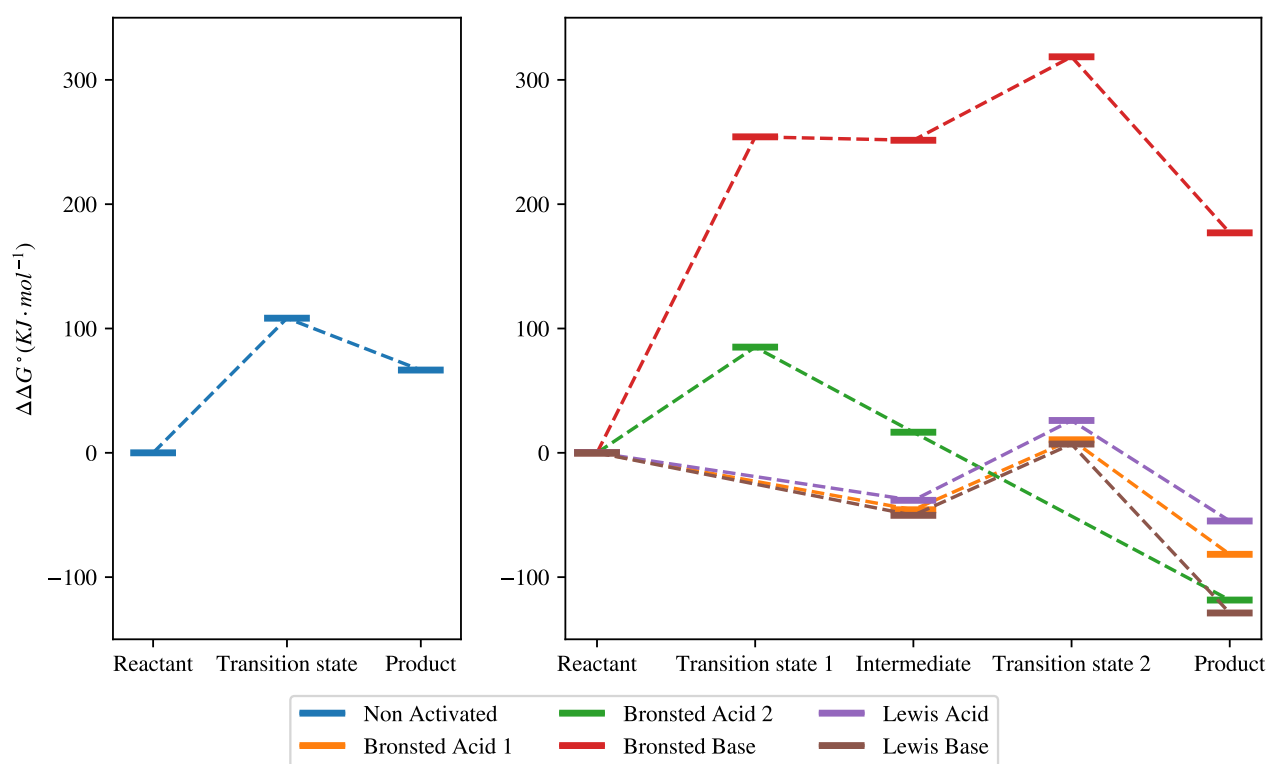


Figure 3.1: Relative reaction trajectories of the non-activated and five catalysed reaction pathways of **1** → **4**. Where no transition states are present, that portion of the pathway was found to be barrierless.

Barrier heights for each step of each potential pathway of **1** → **4** were calculated, and  $\log(k)$  rate constants for each step were determined, using the approach described in [Section 1.4](#). For all steps within the pathways that had distinct barriers, [Equation \(4\)](#) was used to calculate the rate constant, with the transmission coefficient from the Skodje-Truhlar approximations ([Equation \(5\)](#)) being used to account for quantum tunnelling effects. Where no barrier was present, the rate constant was calculated using [Equation \(3\)](#) instead, and without a barrier, transmission coefficient calculations were not necessary. The rate constants for the formation of the intermediate and the cyclisation step were multiplied together to give the overall rate constant for that particular pathway. Any subsequent steps within the pathways would involve further workup experimentally, and were thus not considered to effect the rate of cyclisation. The non-activated pathway involved no intermediate formation, and thus only one step was considered.

Table 3.2: Rate constants ( $\log(k)$ ) for both the intermediate formation reactions and the cyclisation, for each of the six pathways of **1** → **4**. Since the non-activated pathway has no intermediate formation step, it has been left blank.

Pathway	Intermediate formation	Product formation	Overall reaction
Non-activated	-	-6.1	-6.1
Brønsted acid 1	8.0	3.0	11.0
Brønsted acid 2	-1.0	23.7	22.7
Brønsted base	-31.7	1.2	-30.5
Lewis Acid	6.7	1.6	8.3
Lewis Base	8.8	2.9	11.7

Table 3.3: CHELPG partial charges ( $e$ ) of the bonding atoms of the intermediate geometry of each of the pathways.

Pathway	N	$C_\beta$
Non-activated	-0.97	-0.10
Brønsted acid 1	-1.00	-0.02
Brønsted acid 2	-1.06	0.02
Brønsted base	-1.26	-0.12
Lewis Acid	-1.08	0.04
Lewis Base	-1.28	0.10

To further understand the catalytic processes involved, partial charge analysis was performed on the  $\omega$ B97M-V/Def2-QZVPP optimised intermediate geometries of each pathway, to ascertain the nucleophilicity of the cyclising amine and the electrophilicity of  $C_\beta$ . Multiwfn<sup>45</sup> was used to calculate the CHELPG partial charges, based

off the  $\omega$ B97M-V/Def2-QZVPP calculated wavefunction. The process involved calculating the molecular electrostatic potential of the system and projecting the values onto the constituent atoms to assign partial charges. These charges have been tabulated in [Table 3.3](#).

The Hessian from the  $\omega$ B97M-V/Def2-QZVPP thermal corrections was used to re-calculate the  $\Delta G^\ddagger$  of the reaction at various temperatures. Skodje-Truhlar transmission coefficient calculations were performed based on these new values, and were used in the Eyring-Polanyi equation to obtain new rate constants, as shown in [Figure 3.6](#). The imaginary frequency of the transition state was not recalculated, and as such, the transmission coefficient would likely overestimate the proportion of the rate due to tunnelling, however this would introduce minimal error, compared to the large increase in kinetic energy through the increase in temperature.

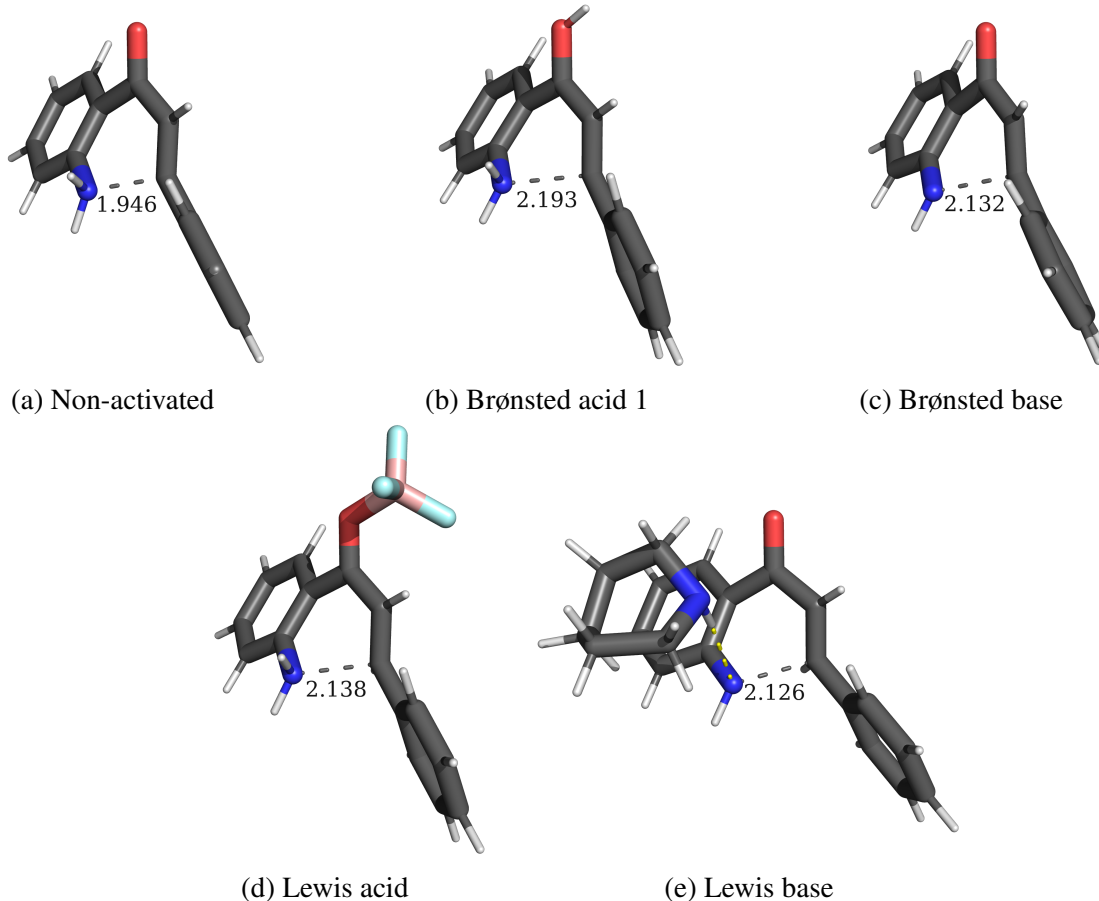


Figure 3.2: Transition state 2 of each of the pathways, excluding the Brønsted acid 2 pathway, as due to its barrierless nature, no transition state geometry exists. The labels show the transition state bonding distance, in angstrom.

Through the process of benchmarking the Lewis base pathway, it became apparent that the assumed mechanism shown in [Scheme 3](#) could not be correct. PES scans were conducted of the cyclisation of the intermediate species, with the proton attached to the cyclising amine, and attached to the Lewis base, forming piperidine<sup>+</sup>. As shown in [Figure 3.3a](#), the cyclisation could only occur if the proton was attached to the Lewis base, as otherwise the new N–C bond was negligibly stable and would likely dissociate. In attempting to optimise the transition state with the deprotonated cyclising amine however, the piperidinium kept dissociating in order to neutralise its charge. Further PES scans were performed to investigate this dissociation and as can be seen in [Figure 3.3b](#), once protonated, the piperidinium leaving was a barrierless process, indicating that it would dissociate before it could catalyse the cyclisation through this particular mechanism.

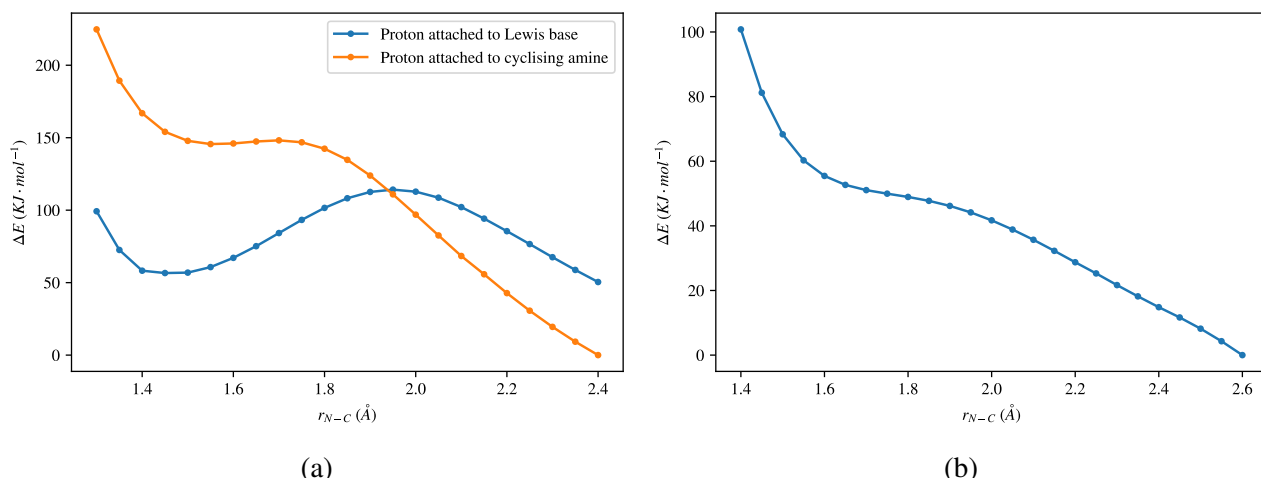
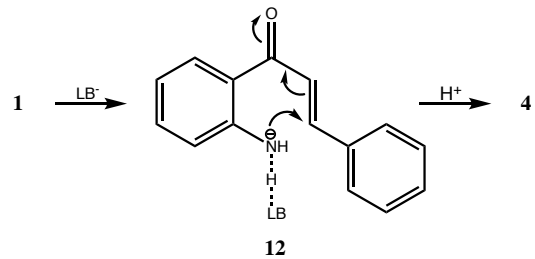


Figure 3.3: a) PES scans along the forming bond of the Lewis base pathway, with the free proton on the Lewis base (blue) and on the cyclising amine (orange). b) PES scan of the  $N_{LB}-C$  bond distance of the protonated Lewis base leaving the carbonyl carbon, prior to cyclisation occurring. The scans in a) were performed with constrained  $N_{LB}-C$  bond distances, in order to prevent the dissociation of the species.

Having identified that the negative charge was more stable

on the cyclising amine, its deprotonation was subsequently assessed for the presence of a barrier with the Lewis base floating freely in the solution, and again, the barrier was not present, leading to the formation of the revised Lewis base mechanism depicted in Scheme 6. In this mechanism, the Lewis base acted as a coordinating Brønsted base,

stabilising the negative charge through hydrogen bonding, as shown in Figure 3.2e. Given that the rate determining step in the Brønsted base pathway was the removal of the amine proton, for the piperidine to result in a barrierless deprotonation, and an intermediate that is more stable than the reactant, explains the efficiency of this pathway as observed by Zheng *et al.*<sup>17</sup>



Scheme 6: Revised Lewis base pathway for the aza-Michael addition of 2'-aminochalcone to form aza-flavanone

Of all the pathways investigated, the fastest was the Brønsted acid 2 pathway, which achieved catalysis through the formation of a carbocation in the  $\beta$  position. These results did not agree with the partial charge analysis however, likely due to donation of electron density from the adjacent phenyl ring.

Analysis of the LUMO of the intermediates of the non-activated and Brønsted acid 2 pathways ([Figure 3.4](#)) revealed that the main driving force of was the formation of the new tetrahedral geometry of  $C_\alpha$ . As a result of this change in geometry,  $C_\beta$  became far more exposed to the HOMO lone pair electrons on the nitrogen (not depicted in [Figure 3.4](#)), making orbital overlap significantly more likely than for the non-activated pathway. Comparing this to the transition state 2 geometries shown in [Figure 3.2](#), the slight torsional strain to the  $C_\alpha=C_\beta$  bond that needed to happen for proper HOMO-LUMO overlap to occur, was not required in this pathway, making it less sterically unfavourable for the cyclisation to proceed, due to the breaking of the  $\alpha, \beta$ -unstaurated ketone.

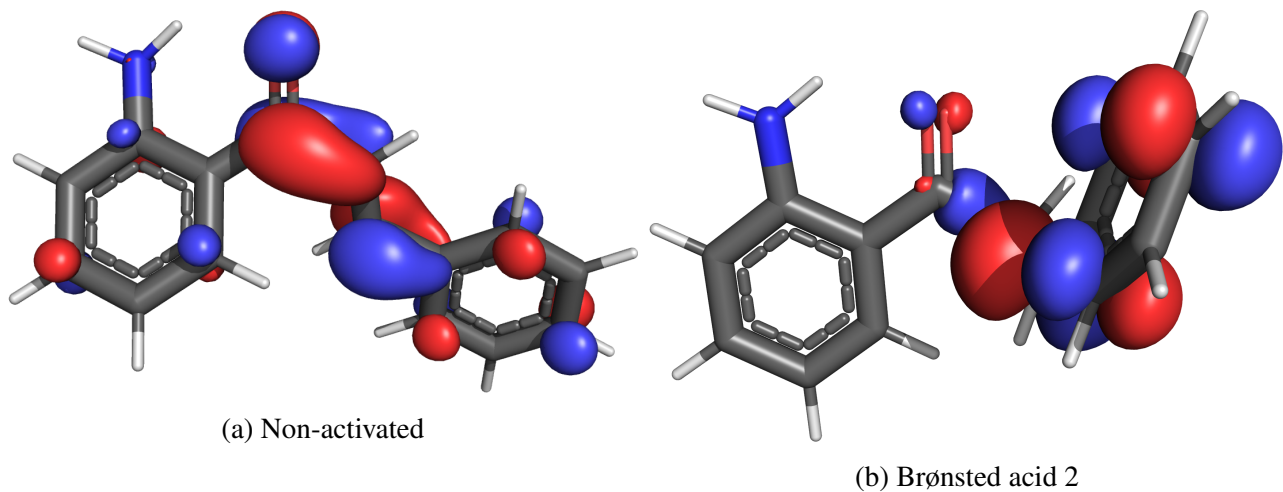


[Figure 3.4](#): Isosurfaces of the LUMO from the non-activated and Brønsted acid 2 pathway intermediate species, following an isovalue of 0.05.

The other key driving factor was the instability of the  $2^\circ$  carbocation. This particular species was more unstable than the charged species of any other pathway studied, due to the breaking of the  $\alpha, \beta$ -unstaurated ketone, which prevented the charge from being distributed up into the more electron rich atoms on the other side of the molecule. The result was that  $C_\beta$  adjacent phenyl ring had an overall partial charge of +0.52, compared with the non-activated pathway, in which the ring had an overall charge of +0.13, indicating the redistribution of the formal charge predominantly throughout the right side of the molecule.

As can be seen in [Figure 3.1](#), the other pathways all followed a relatively similar trend to each other.

The Lewis base and Brønsted base pathways both resulted in significantly more stabilised products than the Lewis acid and Brønsted acid 1 pathways, as the basic pathways resulted in the deprotonation of the amine, leading to the products containing only a single  $2^\circ \alpha$  carbocation, instead of the zwitterionic species of the acidic pathways. Compared with the non-activated pathway, all of the

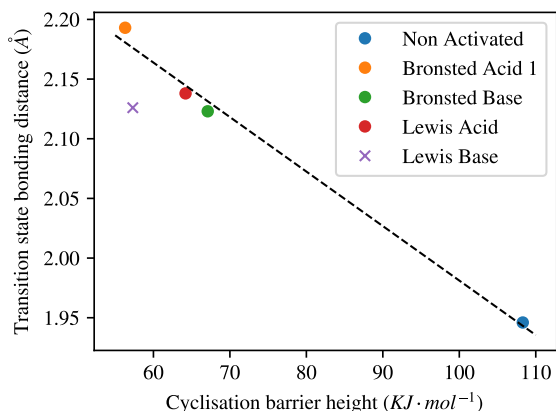


Figure 3.5: Barrier height of the cyclisation step of each of the pathways plotted against their respective transition state bonding distance. A linear trendline ( $R^2 = 0.996$ ) has been added to demonstrate the linearity of the non-intermolecularly stabilised species transition state bond length as a function of their barrier height. The Brønsted acid 2 pathway has been omitted, as no transition state geometry exists.

This can also be seen as this pathway was closest mechanistically to the Brønsted base pathway and has a similar TS bonding distance, however it possesses a lower overall barrier height. This correlation indicates that with the exception of Brønsted acid 2, all the pathways ultimately follow the same approach to catalysing the reaction; increasing the electrophilicity of  $\text{C}_\beta$  and/or increasing the nucleophilicity of the cyclising amine.

catalysed pathways, except for the Brønsted base had transition states and products that were more stable, likely helping to not only increase the rate of the reaction, but also to reduce any re-crossing of the barrier. As can be seen in Figure 3.2 all of the catalytic pathways resulted in earlier transition states for the cyclisation step than in the non-activated pathway, which correlates quite well with their respective barrier heights, as shown in Figure 3.5. The Lewis base pathway was likely an outlier due to the intermolecular stabilisation contributed from the

Multiple approximations and assumptions had to be made to calculate the energy of these pathways. The largest of which was that while the use of SMD solvation does afford a certain amount of stability to separated charges, it lacks the ability to properly hydrogen bond and distribute the charge

throughout the medium in the way that explicit solvation does. This particular issue may have caused  $\text{H}_3\text{O}^+$ , piperidine- and  $\text{C}_\beta^+$  species to not be stabilised to the same extent that they would have if solvated explicitly, resulting in the driving force for the barrierless reactions to be the mitigation of these charged species. If the systems were solvated with explicit water, it is likely that the extra solvent molecules would share their lone pair electrons and that the resulting complex would be significantly more stable than is being represented in the calculations above. This, in turn, may possibly have introduced barriers to these processes, particularly in the formation of the Brønsted acid 1 pathway intermediate. While this could be accomplished by explicitly solvating at least part of the reactant with water or ethanol molecules, the nature of the catalytic pathways had been sufficiently studied to reach the aims of this research.

Further discrepancies from experiment within this method came from the use of transmission coefficient approximations. Using the Skodje-Truhlar approximation, transmission coefficients were estimated to make a significant contribution to the rate constant of  $\kappa > 13.6$  for proton transfers, compared with  $< 1.3$  for the cyclisation steps. Given that these approximations are known to overestimate the effects of quantum tunnelling, this will have associated errors that cannot be easily quantified due to the complexities of quantum phenomena. With how small the proton is, conventional approaches to quantum mechanics which decouple the movement of the protons and electrons, can no longer be assumed to be correct and as such, protons (particularly labile ones) should be treated similarly to an electron in quantum calculations; the proton should be modelled as a wave instead of a particle.<sup>46</sup>

While the errors for the chosen methodology can be considered relatively low for density functional theory,<sup>31,33</sup> it is important to note that errors in the range of  $\pm 8 \text{ kJ}\cdot\text{mol}^{-1}$  are not insignificant when calculating rate constants<sup>I</sup>, which are highly sensitive to small fluctuations in energy. The errors are also calculated as RMSD values, based off benchmarking datasets that may not be representative of

---

<sup>I</sup>Generally speaking, "chemical accuracy" is considered to be  $\sim 4.2 \text{ kJ}\cdot\text{mol}^{-1}$

the systems being studied in this work.

From this work, despite its relatively high reaction barrier and low rate constant, the non-activated pathway was identified as the optimal pathway to study further, under the influence of an OEEF for a number of reasons. Firstly; while its rate constant corresponds to a reaction half life of between 7 and 14 days (depending on the reaction order<sup>II</sup>), under the influence of an OEEF it is very possible that this could be reduced significantly. Secondly; as previously stated, all thermodynamic calculations were performed at 298.15 K. Increasing the temperature would result in a significant increase in the reaction rate, as can be seen by the slope of the curve in [Figure 3.6](#). Depending on the order of the reaction, a 25 °C temperature increase to 50 °C would result in a reaction half life of between 6 and 13 hours, which in conjunction with the effects of an OEEF would be sufficiently fast for the purposes of experimental research.

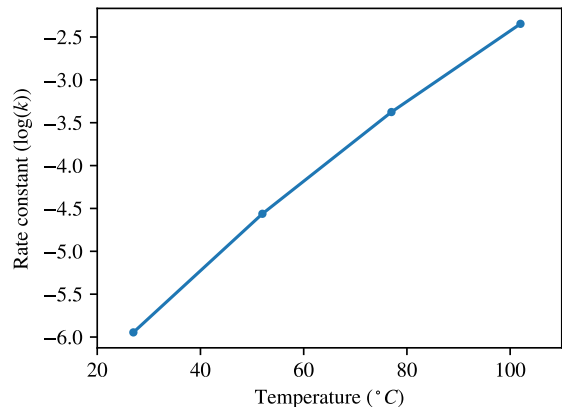


Figure 3.6:  $\log(k)$  Rate constants of the non-activated pathway as a function of temperature.

The choice to investigate the non-activated pathway further was also motivated by its simplicity, in that no extra reactants were required to make the cyclisation occur. In moving this reaction into the experimental space, in order to maximise the propagation of an OEEF through the solvent, tight control of ionic species in solution would be required to ensure that minimal charge screening occurs. Another potential issue could arise in that the the OEEF would induce charge based diffusion through the solution that may interfere with the approximations and assumption made in statistical mechanics based kinetic approaches, adding another variable that would need to be accounted for.

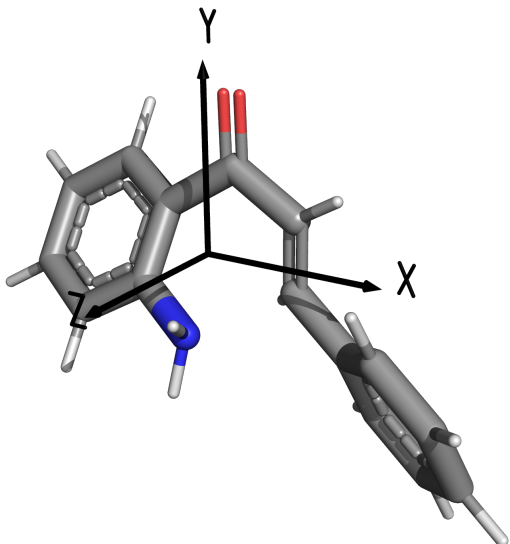
<sup>II</sup>Given that the the reaction is unimolecular and that the reaction site is pre-organised within the molecule, it is likely that it would be on the lower end of this scale

Given that the cyclisation of 2'-aminochalcone is not known to occur spontaneously, it is very probable that a proton source would be required to shuttle the ammonium proton up to the  $\alpha$  carbocation to create a more stable product. Further investigation should be carried out to determine if water by itself would be sufficient for this purpose, or if small amounts of acid would be required to accomplish this experimentally, however as previously discussed, this investigation would likely require the use of explicit solvation and *ab initio* molecular dynamics approaches<sup>47</sup> and could not be justified for this particular investigation.

## 3.2 Static benchmarks based on cardinal field directions, following the "rules"

### 3.2.1 Benchmarking the non-activated pathway barrier as a function of $F_Y$

The  $\omega$ B97M-V/Def2-QZVPP optimised geometries of the product, transition state, and reactant of the non-activated pathway from [Section 3.1](#) were oriented with their C=O bond along the Y axis, and their O=C–C <sub>$\alpha$</sub>  angle in the X/Y plane, as per [Figure 3.7](#).



With this constraint in place, according to [rule \(iii\)](#), the field direction which would have the most stabilising effect on the transition state and thus the largest catalytic effect would be the field that follows the reaction trajectory. As the reaction trajectory for this particular mechanism involves the electron density flowing from the nitrogen, through the C <sub>$\beta$</sub> =C <sub>$\alpha$</sub>  bond, and up onto the ketone as per [Scheme 1](#), the logical choice for a catalytic OEEF was  $\vec{F} = -Y$ . As such, to understand the magnitude of effects that could be expected from an OEEF in the catalytic field direction ( $F_Y$ ), single point calculations at M06-2X/6-31+G\* were performed on each of the geometries with an electric field specified in the Y direction, at strengths ranging from  $-0.015 \text{ au}$  to  $0.015 \text{ au}$  ( $\sim 0.77 \text{ V}\cdot\text{\AA}^{-1}$ ) in  $0.001 \text{ au}$  increments ( $\sim 0.05 \text{ V}\cdot\text{\AA}^{-1}$ ) in SMD ethanol. It is important to note that the field strengths used for this perturbation were incredibly unrealistic, with  $|\vec{F}| > 0.006 \text{ au}$  ( $\sim 0.3 \text{ V}\cdot\text{\AA}^{-1}$ ) being known to facilitate the cleavage bonds within conventional solvents,<sup>48</sup> and  $0.6 \text{ V}\cdot\text{\AA}^{-1}$  being beyond the limits of what is even physically possible. The extended field range of  $\vec{F} = 0.015 \text{ au}$  has become standard in the field of electrostatic catalysis for analysing the extent of perturbative OEEF effects on static geometry.<sup>11</sup>

These particular calculations were performed without allowing the geometry to relax in the field,

which allowed for the resultant energy to be a measure purely of the displacement of the electron density, without letting the geometry adapt to minimise any destabilising effects. With this in mind, the choice of solvating the molecule with SMD ethanol was made to facilitate the charge separation afforded by the OEEF.

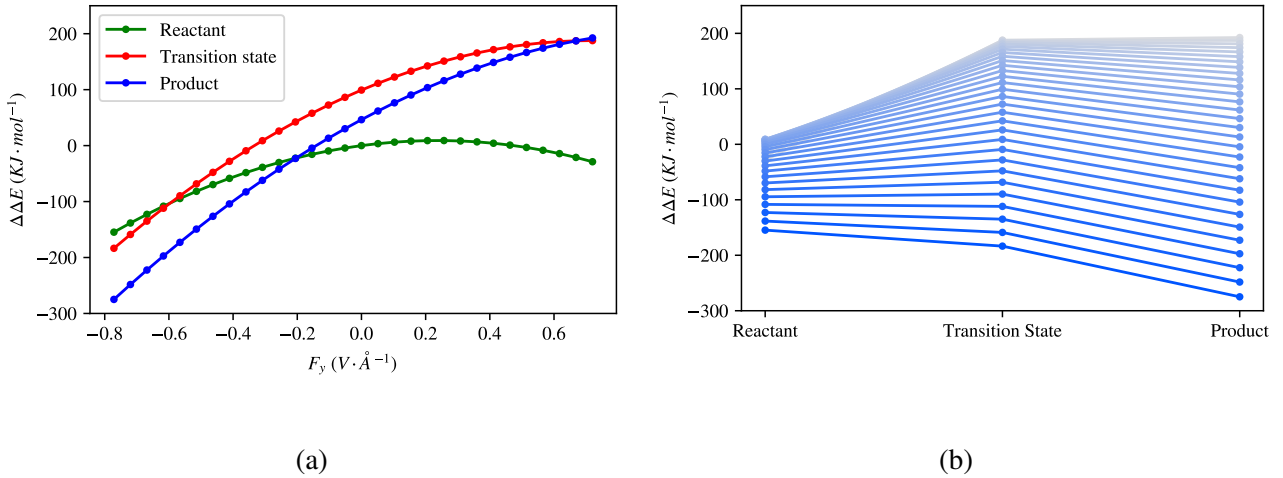


Figure 3.8: a) Potential energy of the reactant, transition state and product as a function of  $F_Y$ , in SMD ethanol. The energies are all relative to the unperturbed reactant. b) Reaction trajectory based on the potential energy from the OEEF scan in [Section 3.2.1](#), coloured from most negative field direction (brightest) to most positive (most dull).

[Figure 3.8](#) shows that the transition state and product of the non-activated pathway were significantly more susceptible to the perturbative effects of  $F_Y$ , however the effect becomes much stronger as the field becomes more negative. This outcome is unsurprising, as  $+F_Y$  corresponds to a negative charge placed above the oxygen, pushing the electron density against the molecular dipole ( $\vec{\mu}$ ) as opposed to  $-F_Y$  which amplifies  $\vec{\mu}$ . Since this polarisation goes against the natural polarity of the molecule, it presents an overall destabilising effect, and would likely result in the electrostatic decomposition of the molecule. These effects can be clearly seen in [Figure 3.9](#), as more positive values of  $F_Y$  begin to negate  $\vec{\mu}$ , making the molecule far less stable. The increase in  $|\vec{\mu}|$  of the reactant at  $F_Y > 0.2 \text{ V}\cdot\text{\AA}^{-1}$  and the

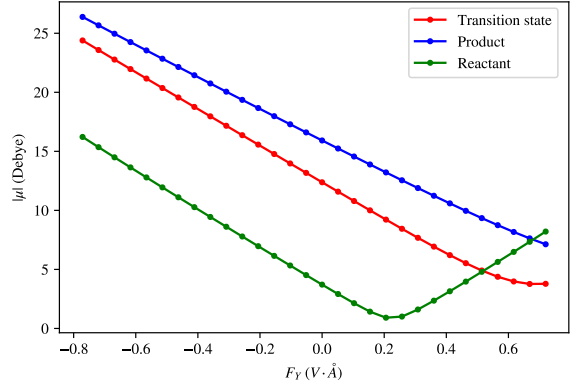


Figure 3.9: Magnitude of the molecular dipole of the reactant, transition state and product of the non-activated pathway, as a function of catalytic OEEF field strength.

transition state at  $F_Y > 0.7 \text{ V}\cdot\text{\AA}^{-1}$  correspond with a reversal of  $\vec{\mu}$  as facilitated by the OEEF.

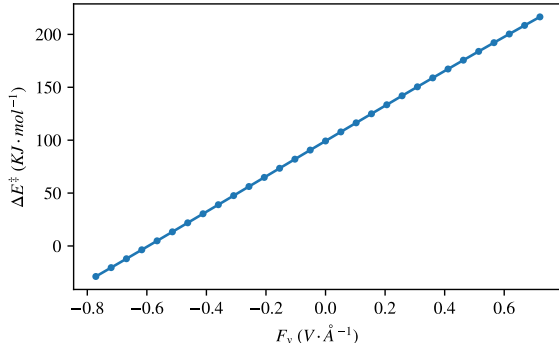


Figure 3.10: The resulting potential energy barrier heights of the reaction trajectory as a function of the strength of  $F_Y$ .

Since the decrease in OEEF perturbations for each of the reactant, TS and product, cancel out at large  $|F_Y|$  the resulting barrier height had a linear trend, with a catalytic benefit, or anti-catalytic penalty of  $16.5 \text{ kJ}\cdot\text{mol}^{-1}$  per  $0.1 \text{ V}\cdot\text{\AA}^{-1}$  of  $-F_Y$  or  $+F_Y$ , respectively. Since the product was far more polarisable than the reactant or transition state in the

Y direction, the OEEF was not only able to decrease the reaction barrier, but also increased the thermodynamic stability of the product, reducing the likelihood of barrier re-crossing. This was likely due to the reactant being fully cyclised and thus being able to better facilitate the shifting electron density from the nitrogen, up through to the ketone. At field strengths  $< -0.6 \text{ V}\cdot\text{\AA}^{-1}$ , the transition state was stabilised so significantly that the barrier was completely negated, however electric fields of this magnitude would likely cause electrostatic decomposition before the reaction could occur.

### 3.2.2 Benchmarking the bias of the S isomer over the R isomer as a function of $F_Z$

The process used to determine the perturbative effects of the OEEF in [Section 3.2.1](#) was repeated with the field direction along the Z axis ( $F_Z$ ) to assess the magnitude of discrimination between the *S* and *R* isomer forming pathways that could be facilitated by an OEEF. This direction was chosen, as it was the axis that ran perpendicular to the reaction trajectory and pertained directly to the difference in  $\vec{\mu}$  between the *R* and *S* isomers, making it the logical choice as per the unofficial [rule \(v\)](#). Since the *R* and *S* isomers are mirror images of each other across the X/Y plane, only the *S* isomer was analysed, as the direction of the OEEF could be inverted to get the equivalent results for the *R* isomer.

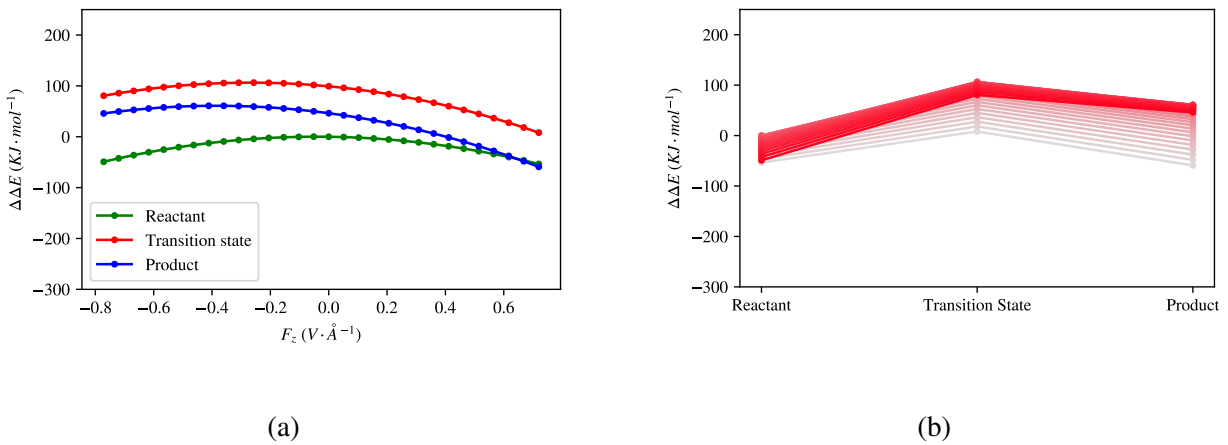


Figure 3.11: a) Potential energy of the *S* isomer of the reactant, transition state and product as a function of  $F_z$ , in SMD ethanol (b). The energies are all relative to the unperturbed reactant. b) Reaction trajectory based on the potential energy from the OEEF scan in Figure 3.11 , coloured from most negative field direction (brightest) to most positive (most dull).

From Figure 3.11 it can be seen that in general, the species were far less polarisable in the Z direction than the Y direction, however this was somewhat unsurprising, as the conjugation that would allow for large amounts of electron density delocalisation were predominantly aligned within the X/Y plane. This did mean, however, that any electron density displacement that occurred was likely along the reaction coordinate itself, facilitating discrimination between the *S* and *R* transition states through the manipulation of the bond formation itself.

In the Z direction, the product again proved to be the most polarisable component of the reaction, however the extent was significantly less than  $F_Y$ , and as such the energetic barrier always remained present. The reactant proved to be stabilised equally by  $-F_Z$  and  $+F_Z$ , however the transition state and product were more stabilised by  $+F_Z$ , likely owing to through-bond electron density shifts, facilitated by the newly formed N–C bond. Looking at  $|\vec{\mu}|$  of these species in Figure 3.12, a similar trend occurs

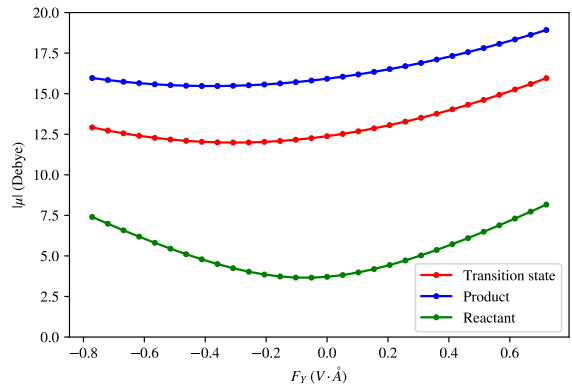


Figure 3.12: Magnitude of the molecular dipole of the reactant, transition state and product of the non-activated pathway, as a function of  $|F_z|$

with  $F_Y$  as with  $F_Z$ , however, since the natural polarity of the molecule results in  $\vec{\mu}$  having a negligibly small Z component compared to its Y component, the small shifts to the electron density in the Z axis had significantly smaller effects on the potential energy of the molecules.

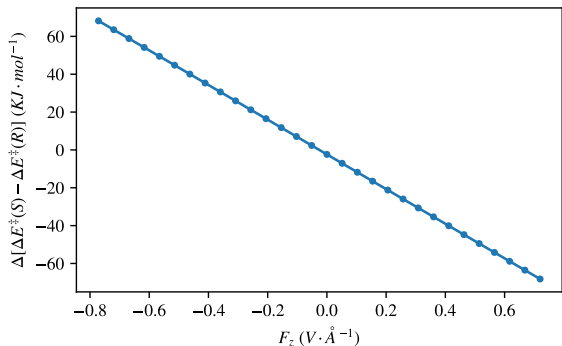


Figure 3.13: The resulting gas phase and SMD solvated barrier heights of reaction trajectory as a function of the strength of  $F_Z$ .

Since the benchmarked geometry was that of the *S* isomer, and since it was aligned as per Figure 3.7, the results of the scans were inverted to reverse the field direction, which provided the results of the *R* isomer. Subtracting the potential energy barrier heights of the inverted scans (*R* isomer), from the non-inverted scans (*S* isomer), provided the amount of

discrimination between the two isomer forming reactions that  $F_Z$  afforded, as shown in Figure 3.13. From these results, it can be said that more positive values of  $F_Z$  select for the *S* isomer and more negative values select for the *R* isomer which can be quantified as a  $9.1 \text{ kJ}\cdot\text{mol}^{-1}$  bias in favour of the *S* pathway per  $0.1 \text{ V}\cdot\text{\AA}^{-1} +F_Z$ , or in favour of the *R* pathway per  $0.1 \text{ V}\cdot\text{\AA}^{-1} -F_Z$ .

Previous studies by Wang *et al.*<sup>11</sup> on the stereocontrol of Diels-Alder reactions showed that a stereoselective OEEF posed a systematic effect on all of the species within the reaction, leaving the barriers of the *R* and *S* isomer forming pathways identical, so any separation between the two pathways occurred by stabilising the reaction pre-complex that resulted in one isomer over the other. Interestingly, in this particular study, the influence of the *R/S* selective OEEF resulted in more significant stabilisation to the transition state and product of the reaction, causing a change in the reaction barrier itself.

Computational studies within this field often explore a very wide range of field strengths,<sup>11,49</sup> however while they may provide interesting insights into molecules at, and beyond their limits of stability,

they can be considered unrealistic and unrepresentative for practical applications. As such, further investigations within this research use an OEEF of  $|\vec{F}| = 0.1 \text{ V}\cdot\text{\AA}^{-1}$  as a default with a larger  $|\vec{F}|$  of  $0.2 \text{ V}\cdot\text{\AA}^{-1}$ , since the aims of this research were fundamentally to obtain a qualitative understanding as a guide for future experimental research.

Generally speaking  $F_Z < 0$  was found to stabilise the *S* isomer and destabilise the *R* isomer to the same extent that  $F_Z > 0$  destabilised the *S* isomer and stabilised the *R* isomer. Because of this, to reduce computational cost by taking advantage of stereoisomeric symmetry, further studies within this research were performed only on the *S* isomer. The assumption was made that any and all results pertaining to OEEF mediated stereoselectivity could be generalised to the *R* isomer by flipping the Z component of  $\vec{F}$  across the X/Y plane. As such, an OEEF residing predominantly in  $+F_Z$  will be referred to as "S selective" and a field predominantly in  $-F_Z$  will be referred to as "S anti-selective". A similar approach to naming convention was taken for a field direction predominantly in  $-F_Y$ , with it from here on being referred to as "catalytic", since  $F_Y < 0$  was shown to decrease the barrier of the reaction.

### 3.2.3 Investigating the role of dielectric medium (CPCM) on OEEF perturbation

To understand the extent by which the dielectric constant of the solvent influenced the effects of the OEEF, the oriented geometries from the previous calculations were used, and single point calculations were performed on each geometry at M06-2X/6-31+G\* with CPCM ethanol, varying the dielectric constant from 5 to 100 in increments of 5. Scans were performed using catalytic ( $F_Y = -0.1 \text{ V}\cdot\text{\AA}^{-1}$ ), *S* selective ( $F_Z = 0.1 \text{ V}\cdot\text{\AA}^{-1}$ ) and, *S* anti-selective ( $F_Z = -0.1 \text{ V}\cdot\text{\AA}^{-1}$ ) OEEFs for each of the reactant, transition state and product geometries, to assess the solvent effects on both the catalytic and stereoselective OEEF field directions.

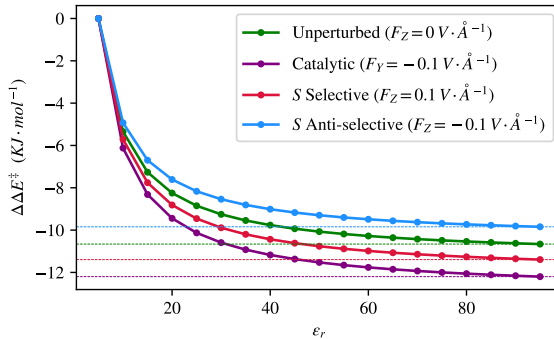


Figure 3.14: Reduction in barrier heights of the OEEF-perturbed and non-perturbed scans of the non-activated pathway as a function of solvent dielectric constant. The barrier heights are all relate to their maximum energy at  $\epsilon_r = 0$ .

marginal differences in energy arising from the polarisation of the molecules due to the OEEF itself.

Knowing that the nature of the OEEF is to polarise the species within the reaction, the assumption was made that solvation would be of particular importance to support any charge separation facilitated by the perturbation of the OEEF. However, Figure 3.14 indicated that the stabilisation of the species afforded by the dielectric medium was predominantly one of stabilising the molecule as a whole, with only marginal differences in energy arising from the polarisation of the molecules due to the OEEF itself.

This energy difference has been quantified in

Figure 3.15 by taking the barrier height differences between each of the OEEF perturbed pathways and the unperturbed pathway, with the energetic difference pertaining to the stabilisation of the

OEEF-polarised reaction by the dielectric medium.

When considering both figures, and how minimally the solvation supports the OEEF perturbation, it can be concluded that rather than choosing a solvent that

facilitates the charge separation of the polarised transition state, it is more important to choose a solvent with the lowest dielectric constant, in which the reactant remains soluble. This should allow for maximum propagation of the OEEF through the solvent, without significantly penalising the polarisation effects of the OEEF. With this in mind, the ideal solvent for this particular reaction should have a dielectric constant between 20 and 30 and will be further explored in Section 3.4.

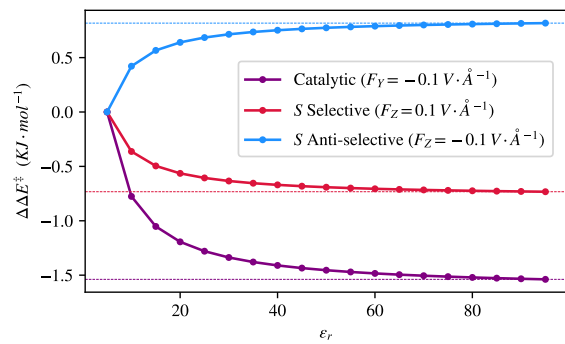


Figure 3.15: Differences between the OEEF perturbed barrier heights and non OEEF-perturbed scans of the non-activated pathway as a function of CPCM dielectric constant. This plot shows the amount of stabilisation afforded by the CPCM dielectric pertaining to the stabilisation of OEEF induced charge separation.

### 3.3 Identifying optimal OEEF directions for catalysis and *R/S* selectivity

All assumptions so far about appropriate OEEF directions to obtain particular effects were made according to the Shaik's rules. To confirm their validity and to better identify the ideal OEEF directions, however, novel approaches to the issue had to be devised and as such involved the use of extensive scripting to interpret and visualise the data. Due to their extensive python scripting interfaces, all of the following calculations were performed using Psi4 1.4<sup>50–52</sup> with the results being visualised in PyMOL open-source 2.6.0a0.<sup>53</sup>

For each of the *R* and *S* isomers, the oriented transition state geometry from the  $\omega$ B97M-V/Def2-QZVPP optimisations was taken, and single point calculations were performed at M06-2X/6-31+G\* without solvation.

A series of vectors,  $0.1 \text{ V}\cdot\text{\AA}^{-1}$  long, pointing in 56 equally spaced directions was generated, with each vector specifying the direction and magnitude of  $\vec{F}$ .

For each of the field directions, the electric field was applied and subsequent single point calculations were

performed at the same level of theory as the perturbed reference point. The resulting catalytic energies were taken as the difference between the perturbed and unperturbed single point energies for each field direction. These results have been presented in

[Figure 3.16](#). The scans were repeated at the same level of theory on the  $\omega$ B97M-V/Def2-QZVPP

optimised *R* isomer geometry, and the *R/S* separation energy for each OEEF direction was taken as

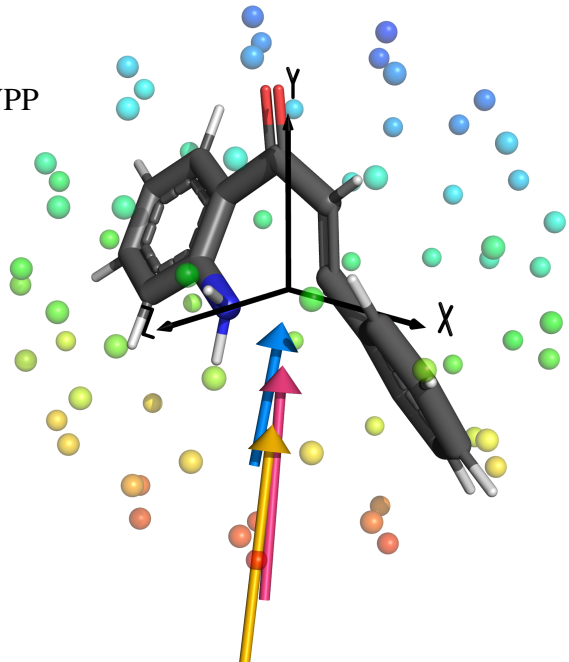
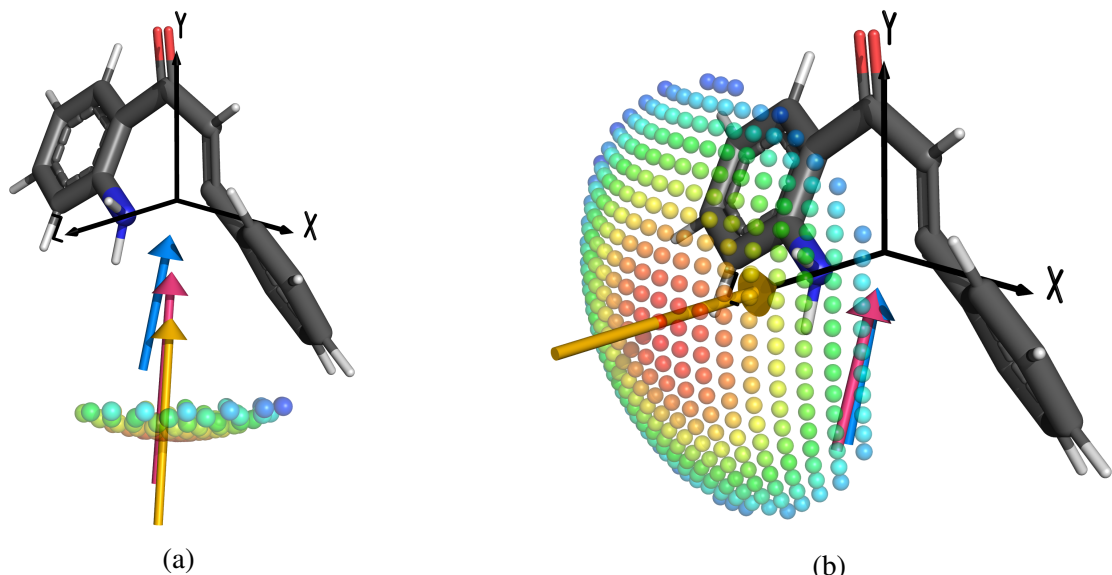


Figure 3.16: Initial, rough scan of the catalytic stabilisation of the *S* isomer afforded by various OEEFs on the non-activated transition state, relative to the non-OEEF perturbed molecule. Each sphere represents a perturbed field direction, and its colour represents the magnitude of the perturbation from most stabilising (red) to least (blue). The arrows represent the most stabilising field direction (yellow), the relative magnitude and direction of the molecular dipole of the unperturbed transition state (blue) and the perturbed transition state (pink).

$$\Delta E_{TS}(S) - \Delta E_{TS}(R)$$

for that specified OEEF perturbation.

Once the general direction of the optimal catalytic and selective fields was identified, higher resolution scans centred only around the region identified by the rough scans were performed at the same level of theory, with 106 vectors selected for the catalytic field direction and 319 vectors for the *S* selective field direction. From these results, an optimal *S* isomer "catalytic" field direction was identified based on the maximum OEEF mediated stabilisation relative to the unperturbed molecule, as shown in [Figure 3.17a](#). The field direction that proved the most selective for the *S* isomer over the *R* isomer was also selected as the "S selective" field direction, as shown in [Figure 3.17b](#). Due to the symmetry of the *S* isomer across the X/Y plane, the *S* selective OEEF was flipped in the Z direction to provide the *S* anti-selective field direction. The specific vectors for these fields have been tabulated in [Table 3.4](#).



**Figure 3.17:** More granular scans of a) the catalytic effects of the OEEF on the *S* isomer transition state, and b) the stereoselective effects of the OEEF for the *S* isomer over the *R* isomer. Each sphere represents a perturbed field direction, and its colour represents the magnitude of the perturbation from most catalytic (red) to least (blue), and most selective for the *S* isomer (red) to least (blue). The arrows represent the optimal field direction (yellow), and the the relative magnitude and direction of the molecular dipole of the unperturbed transition state (blue) and the perturbed transition state (pink).

For [Figures 3.16](#) and [3.17](#), relative energy values for the figures have have been intentionally omitted, as without any form of solvation, their values would be meaningless. While this method has been shown to represent the perturbative effects of OEEFs quite well, when introducing the errors associated

with gas phase calculations, these calculations should only be considered qualitative.

Table 3.4: Optimal OEEF directions for catalysis and stereoselection in  $\text{V}\cdot\text{\AA}^{-1}$ . The *S* anti-selective field is the *S* selective field, flipped along the mirror plane for the molecule; the Z axis.

OEEF function	$F_X$	$F_Y$	$F_Z$
Catalytic	$2.728 \times 10^{-3}$	$-9.513 \times 10^{-2}$	$1.451 \times 10^{-2}$
<i>S</i> selective	$-1.737 \times 10^{-2}$	0.0	$6.145 \times 10^{-2}$
<i>S</i> anti-selective	$-1.737 \times 10^{-2}$	0.0	$-6.145 \times 10^{-2}$

As can be seen in [Figure 3.17a](#), the identified catalytic and selective OEEF directions were in general agreement with the rules laid out by Shaik *et al.*,<sup>10</sup> however, these rules assume that the optimal catalytic OEEF should follow the reaction axis, pointing from the amine towards the oxygen. Through this scan it was shown that the optimal catalytic OEEF direction should follow from halfway between the forming N–C bond, up towards the oxygen, likely due to the electron density bulk of the reaction axis lying closer to  $\text{C}_\beta$ , than to the  $-\text{NH}_2$ . As expected, the OEEF also had a large influence on  $\vec{\mu}$ , both causing it to align with the OEEF, and increasing its magnitude. The optimal field direction for discrimination between the *S* and *R* pathways proved to be almost exactly in line with the Z axis, with a slight bias to align along the newly forming N–C bond. This perturbation had minimal effect on the dipole moment, which was in line with the findings in [Section 3.2.2](#).

It is worth noting that any OEEF aligned directly in the XY plane elicited no effect on the stereoselectivity of the reaction, however as soon as a Z component was added to  $\vec{F}$ , stereoselectivity started to increase. The same gradual increase was observed as the OEEF approached the reaction axis resulting in a gradual increase in stabilisation. Regardless of the direction, the OEEF always produced some form of perturbation, but the closer that  $\vec{F}$  was to the optimal stereoselective or catalytic field directions, the more pronounced and desirable the perturbative effects were.

As with the previous calculations, it is important to note that differences in the identified optimal field

directions may result if the geometry were re-optimised within the electric field, allowing it to relax to the perturbation of the OEEF.

### 3.3.1 Electron density difference analysis of the optimised OEEF perturbations

To identify the mechanisms by which the catalytic and selective OEEFs exert their effects on the transition state, electron density differences between the unperturbed and perturbed transition states were compared. For each of the refined field directions identified in [Section 3.3](#), electron density difference iso-surfaces of the  $\omega$ B97M-V/Def2-QZVPP optimised geometry for the transition state of the non-activated pathway were produced. This was again performed in Psi4 1.4 and involved the subtraction of the unperturbed electron density from the OEEF-perturbed electron density of each of the systems. The electron densities were calculated with M06-2X/6-31+G\* with CPCM solvation.

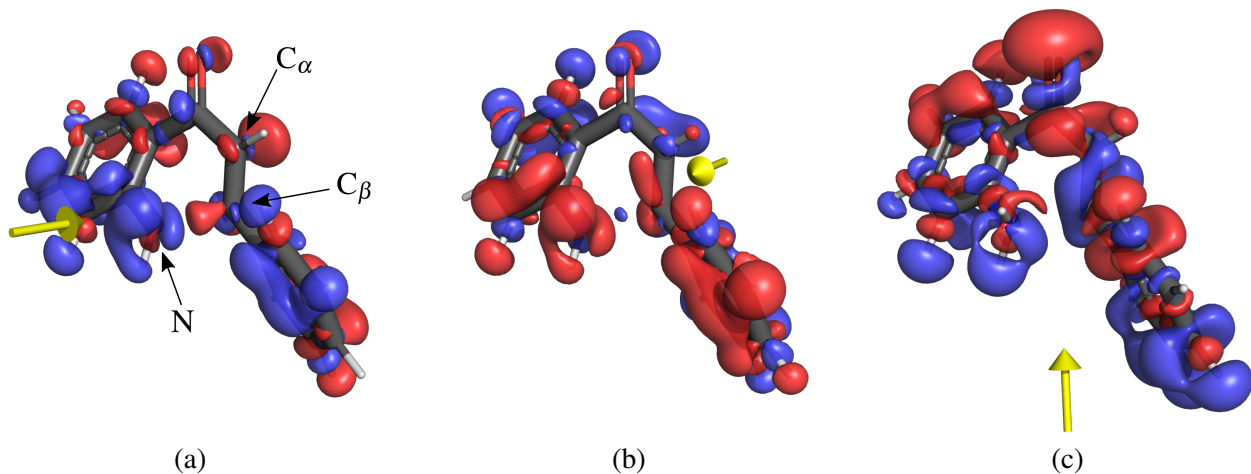


Figure 3.18: Electron density difference isosurfaces of the non-activated transition state geometry in CPCM ethanol, as perturbed by the optimised a)  $S$  selective, b)  $S$  anti-selective, and c) catalytic field directions at  $|\vec{F}| = 0.1 \text{ V}\cdot\text{\AA}^{-1}$  as per [Table 3.7](#), following an isovalue of 0.0002. The red and blue isosurfaces represent regions of increased and decreased electron density, respectively. The yellow arrow is a representation of  $\vec{F}$ .

The process by which these electric field selections exert their effects on the transition state can be quite clearly seen in the electron density difference isosurfaces shown in [Figure 3.18](#). In the catalytic field direction, by pushing the electron density of the transition state along the reaction trajectory

(according to rule (iii)), while the NH<sub>2</sub> has no net displacement of electron density, C<sub>β</sub> is made significantly more electrophilic, as the electron density of the C<sub>α</sub>=C<sub>β</sub> π bond is pushed up into to the LUMO π\* orbital residing along the C(=O)–C<sub>α</sub> bond (see [Figure 3.4a](#)). This mixing of the α,β-unsaturated ketone π system with the LUMO also occurs along the ketone double bond, making the oxygen much more negatively charged. This whole process could be considered to make the TS more like the cyclised product, resulting in a much smaller configurational change between the TS and product. It could also be considered to produce a more electrophilic C<sub>β</sub> in order to more readily accept the NH<sub>2</sub> lone pair electrons.

A similar process seems to occur in the S selective field direction, in a much more simplified manner. The cyclisation process involves the NH<sub>2</sub> lone pair electrons mixing with the LUMO π\* orbital around C<sub>β</sub> (as per [Figure 3.4a](#)), so by pushing the electron density from the NH<sub>2</sub> into the π\* orbital, the OEEF effectively starts the bond formation process. The opposite happens for the S anti-selective field direction, and any electron density from the lone pair that would naturally reside in the space between the NH<sub>2</sub> and C<sub>β</sub> is forced back onto the nitrogen. This transition state is further deactivated, as some of the electron density from the conjugated system gets pushed onto C<sub>β</sub> making it even less electrophilic.

### 3.4 Benchmarking the optimised OEEF directions on relaxed geometry

As all of the previous investigations into the effects of OEEFs on the non-activated pathway had been completed on static geometry, piecing together the individual components in a more cohesive study required the molecules to be relaxed within the field. Due to the rotational torque exerted on the molecules by the OEEF ([rule \(iv\)](#)), the specific directionality of the field proportional to the reaction axis would not be able to be maintained. As such, constraints were used within the optimiser to keep the molecule aligned.

For each of the reactant, transition state and product, their geometries were constrained with their C=O bond aligned with the Y axis and their O=C–Ph angle constrained to the XY plane. They were subsequently optimised in each of the catalytic, *S* selective and *S* anti-selective field directions identified in [Section 3.3](#), as well as without an electric field present. These calculations were performed in ORCA at M06-2X/6-31+G\* with CPCM solvation in n-hexane, dichloromethane (DCM), ethanol, dimethylsulfoxide (DMSO) and water, as well as without solvation. Thermodynamic calculations were subsequently performed on the optimised geometries at the same level of theory with the same solvation. As with the process from [Section 3.1](#), Skodje-Truhlar transmission coefficient approximations were calculated for each pathway using [Equation \(5\)](#), and rate constants were calculated using the Eyring-Polanyi equation, ([Equation \(4\)](#)) as tabulated in [Table 3.5](#).

Table 3.5: Rate constants for the relaxed geometry of the non-activated pathway, as perturbed by the identified catalytic, *S* selective and *S* anti-selective OEEFs, in comparison to the unperturbed pathway, in a range of solvents. All rates are shown as  $\log(k)$ .

Solvent	Unperturbed	<i>S</i> selective	<i>S</i> anti-selective	Catalytic
Gas ( $\varepsilon_r = 0$ )	-14.7	-14.5	-15.4	-13.1
Hexane ( $\varepsilon_r = 2.0$ )	-11.5	-10.8	-12.4	-9.6
DCM ( $\varepsilon_r = 8.9$ )	-7.8	-7.1	-8.6	-5.4
Ethanol ( $\varepsilon_r = 24.9$ )	-7.4	-6.4	-8.0	-4.7
DMSO ( $\varepsilon_r = 46.8$ )	-6.9	-6.0	-7.7	-4.4
Water ( $\varepsilon_r = 78.4$ )	-6.8	-5.9	-7.7	-4.3

The general trends from [Table 3.5](#) emphasised the findings from [Section 3.2.3](#) in that any increase in dielectric constant above  $\varepsilon_r = 20$  provided diminishing returns. Rate improvements between ethanol ( $\varepsilon_r = 24.9$ ) and water ( $\varepsilon_r = 78.4$ ) only provided marginal improvements in  $\Delta \log(k)$  of 0.1 for *R/S* separation and 0.3 for catalysis, as can also be seen in [Section 3.4](#).

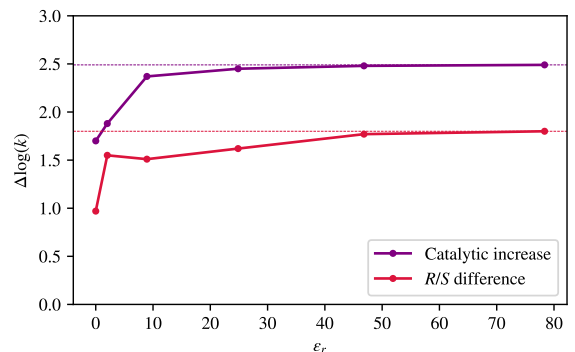


Figure 3.19:  $\log(k)$  rate constant differences between the catalysed and unperturbed, and *S* selective and *S* anti-selective OEEF perturbed pathways, modelled against a series of solvents. Asymptotes have been drawn in for easier comparison of trends.

Compared with the results in [Section 3.2.3](#) the process of relaxing the geometry afforded a significantly larger stabilisation of the barrier height, as a function of the solvent dielectric. This was likely due to the relaxation process allowing the molecule itself to physically separate any charges that were created through the perturbation of the OEEF.

In comparing [Figure 3.20b](#) with [Figure 3.15](#), significantly larger contributions from the solvation model to the effects of the OEEF were also identified. Unsurprisingly, while the geometry relaxation did cause an increase in the *S* anti-selective OEEF perturbation (likely due to the geometry being able to better separate charges), it also allowed for the geometry to better negate these effects, resulting in a smaller increase in OEEF effect than for the other perturbed fields.

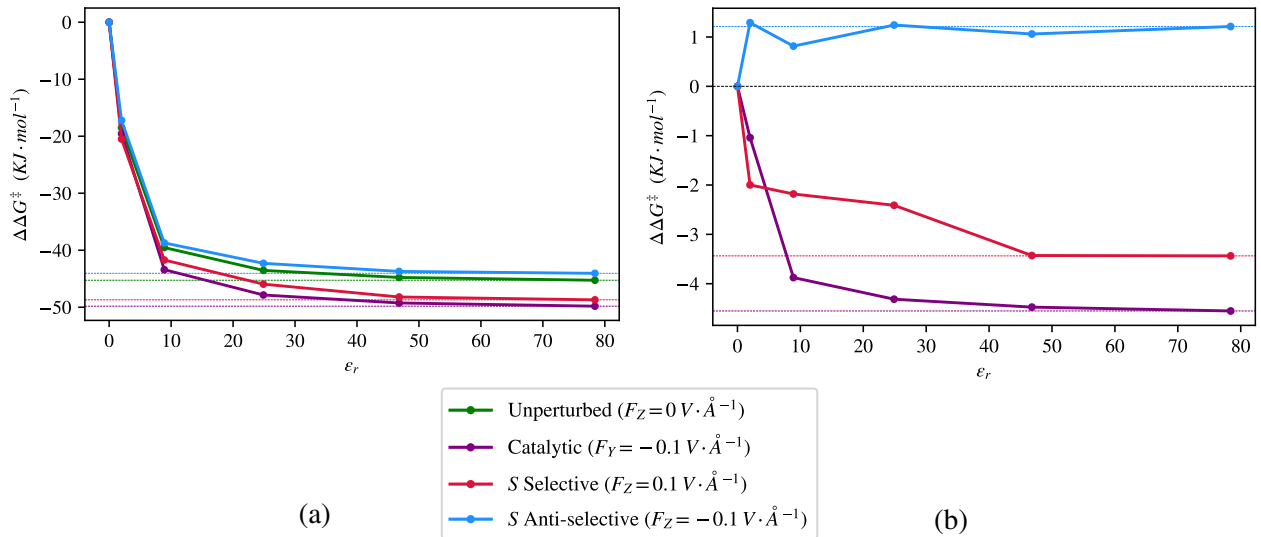


Figure 3.20: a) Reduction in barrier heights for the non OEEF-perturbed and for each of the optimised OEEF directions as a function of solvent dielectric constant, relative to the maximum energy at  $\epsilon_r = 0$ . b) Relative differences between the non OEEF-perturbed and OEEF-perturbed results from Figure 3.20a. This plot shows the amount of stabilisation afforded by the CPCM dielectric pertaining to the stabilisation of OEEF induced charge separation, with the added stabilisation of the geometry relaxation.

The results from this experiment were far more discontinuous than that of any of the previous scans, owing to the geometry being allowed to relax itself within the OEEF in order to minimise its energy. Given that the optimiser followed a gradient descent from the same starting geometry, it is likely that small deviations in the effects of each particular solvent would have resulted in a slightly different pathway being followed and thus a different minima on the PES being reached, resulting in non-continuous results. When comparing the  $\Delta\Delta E^\ddagger$ , prior to the application of thermal corrections with the thermally corrected  $\Delta G^{\ddagger}$ , a systematic increase in energy of  $\sim 2 \text{ kJ}\cdot\text{mol}^{-1}$  was identified across all solvents, and OEEF directions. This indicates that the predominant differences in barrier height between Figures 3.14 and 3.20a were specifically a result of the relaxation process, and not of the thermal contributions.

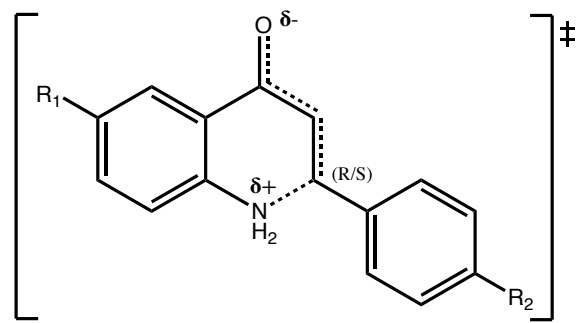
As discussed in Section 3.2.3, a theoretical tradeoff had to be made in deciding whether to choose a computational methodology that better captured the effect of the OEEF perturbation or that better represented the thermodynamics of the system. For this particular study, despite calculating thermodynamic

corrections in order to determine rate constants, it should be noted that for the non-perturbed reaction in ethanol, a  $\log(k)$  rate constant of -7.4 was identified at M06-2X/6-31+G\*, where in [Section 3.1](#),  $\omega$ B97M-V/Def2-QZVPP gave a  $\log(k)$  rate constant of -6.1. As such, the results from this section cannot be directly compared with those of [Section 3.1](#). It also cannot be assumed that these differences were systematic.

Since the methods used in this section were chosen to better represent the perturbative effects of the OEEF, the absolute values of the rate constants within this section should be considered non-representative of the reaction itself, however the rate constant differences shown in [Section 3.4](#) provide an indication of the perturbative effects of the OEEF, and ultimately of the rate constants. From this study, it can be concluded that in a modest OEEF of  $|\vec{F}| = 0.1 \text{ V}\cdot\text{\AA}^{-1}$ ,  $\log(k)$  rate constant increases of up to 2.5 can be achieved for the reaction in a catalytic OEEF and  $\log(k)$  rate constant differences of 1.8 can be obtained between the formation of the *R* and *S* isomer in an appropriately stereoselective OEEF.

### 3.5 Investigating the effects of charged derivatisation of 2'-aminochalcone

To understand the effects of derivatisation of 2'-aminochalcone with charged functionality, on the stereoselectivity afforded by the OEEF, a series of OEEF scans were performed in a similar fashion to [Section 3.3](#).



Scheme 7: Transition state of the non-activated pathway, showing the placements for R<sub>1</sub> and R<sub>2</sub>

The locations of R<sub>1</sub> and R<sub>2</sub> were chosen, due to their maximal distance from the reaction centre. This would allow for electrostatic effects to dominate over electron direction through conjugation. Given how extensive the conjugation in the system was, these effects could not be wholly mitigated. The choice of using –NO<sub>2</sub> and –NH<sub>2</sub> was based on their overall formal charges. –NO<sub>2</sub> was considered a powerful electron withdrawing group, and electrostatically would present a negative charge, while –NH<sub>2</sub> was considered an electron donating group and would present a positive charge, making them polar opposites. –H was considered a neutral intermediate species.

Starting with the ωB97M-V/Def2-QZVPP optimised geometry of the transition state of the non-activated pathway, modifications were made to the geometry in Avogadro<sup>2</sup>, as per [Scheme 7](#) with all permutations of R<sub>1</sub>/R<sub>2</sub> = H, NH<sub>2</sub>, NO<sub>2</sub> being produced. Each of the derivatives were perturbed with 105 field directions of magnitude  $|\vec{F}| = 0.1 \text{ V}\cdot\text{\AA}^{-1}$  at M06-2X/6-31+G\* without solvation in Psi4 1.4, using the same process as described in [Section 3.3](#). For these scans, the methodology differed in that the geometries were constrained as per [Section 3.4](#) and optimised in the specified OEEF at M06-2X/6-31+G\* before the single point energy was calculated.

Optimal OEEF directions were identified by subtracting the S isomer energy from the R isomer energy for each scanned OEEF direction and identifying the OEEF that resulted in the lowest energy

difference. These OEEF directions have been shown in [Figure 3.21](#), and their associated energy differences were tabulated in [Table 3.6](#). To obtain a better understanding of how the OEEF effected each individual isomer, their relative energies were plotted in [Figure 3.22](#).

A few methodological sources of error should be noted, in that this approach was severely limited by the granularity of the chosen OEEF directions, which as can be seen in [Figure 3.21](#), was relatively sparse in regions where more precision would have been desired. There was also a limitation in that Psi4 1.4 was written with modern basis sets in mind, and as such, when using older Pople style basis sets, in conjunction with the optimiser that was considerably less robust than that used in ORCA, slightly less optimal transition state geometries may have resulted. As with [Section 3.3](#), the results from this section should also be considered qualitative only, due to both the lack of solvation used, and the large methodological errors.

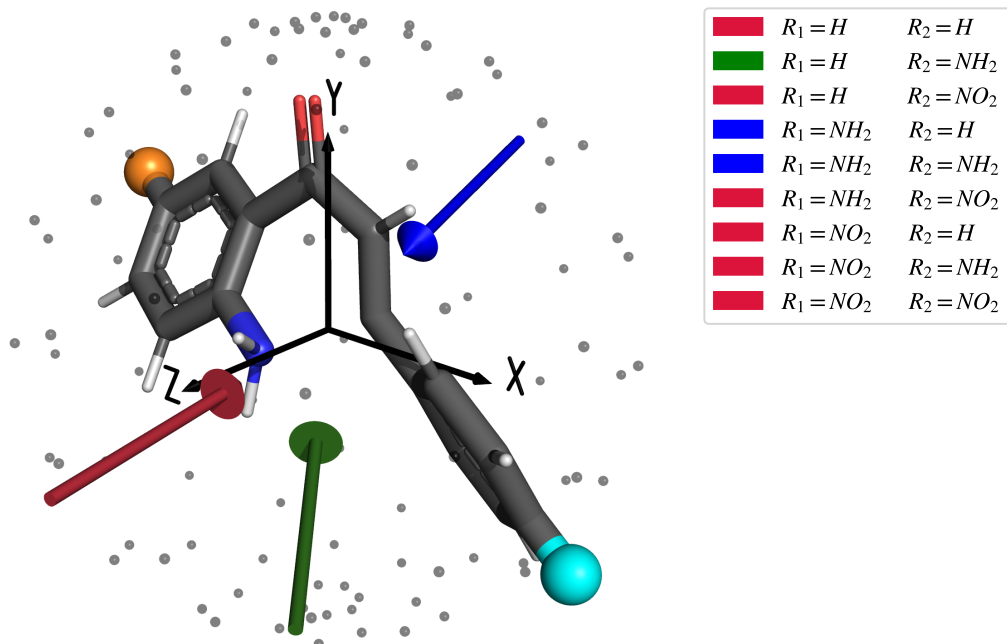


Figure 3.21: OEEF directions that result in the maximum separation between the *S* and *R* pathways of the derivatised transition state. The grey dots represent the scanned OEEF directions and the arrows denote the OEEF that resulted in the maximum *S* and *R* separation for each derivative. The orange group represents  $R_1$  and the cyan group represents  $R_2$ .

Some of the systems proved more difficult to analyse the results of, and as such electron density difference isosurfaces were also produced for each OEEF perturbation of each derivative, following

the methodology described in [Section 3.3.1](#). These surfaces have been included in [Appendix C](#).

Beyond the general effects afforded by the OEEF described in [Section 3.3](#), the effects of derivatisation can largely be broken down into a few key generalisations. Firstly, functionality in the  $R_1$  position generally posed a larger effect on the *S* isomer, and functionality in the  $R_2$  position mostly effected the *R* isomer. This was due to the  $R_1$  position predominantly effecting the cyclising amine, and the  $R_2$  position predominantly effecting  $C_\beta$ . The effects generally followed the order of  $-\text{NH}_2$  decreasing the stereoselectivity, and  $-\text{NO}_2$  increasing it.

Table 3.6: Maximum electronic energy energy differences between *S* and *R* isomers of the derivatives of the non-activated pathway, as identified by OEEF scanning. The energy reported as  $\Delta\Delta E$  is calculated as  $\Delta E(S) - \Delta E(R)$  as perturbed by  $\vec{F} = 0.1 \text{ V}\cdot\text{\AA}^{-1}$ .

$R_1$	$R_2$	$\Delta\Delta E$ <i>R/S</i> Separation ( $\text{kJ}\cdot\text{mol}^{-1}$ )
H	H	-4.3
H	$\text{NH}_2$	-0.7
H	$\text{NO}_2$	-4.8
$\text{NH}_2$	H	-2.2
$\text{NH}_2$	$\text{NH}_2$	-6.3
$\text{NH}_2$	$\text{NO}_2$	-4.6
$\text{NO}_2$	H	-19.6
$\text{NO}_2$	$\text{NH}_2$	-16.1
$\text{NO}_2$	$\text{NO}_2$	-19.7

A better understanding of the behaviour of the derivatives can be obtained from [Figure 3.23](#), in which the trends become more obvious, that the addition of extra electron density through  $-\text{NH}_2$  in either the  $R_1$  or  $R_2$  positions leads to a stabilisation of the *R* isomer. For  $-\text{NO}_2$ , the effects appeared to be dependent on the location within the molecule, with  $R_1=\text{NO}_2$  leading to significant stabilisation of the *S* isomer and destabilisation of the *R* isomer, and  $R_2=\text{NO}_2$  leading to a systematic destabilisation of both isomers.

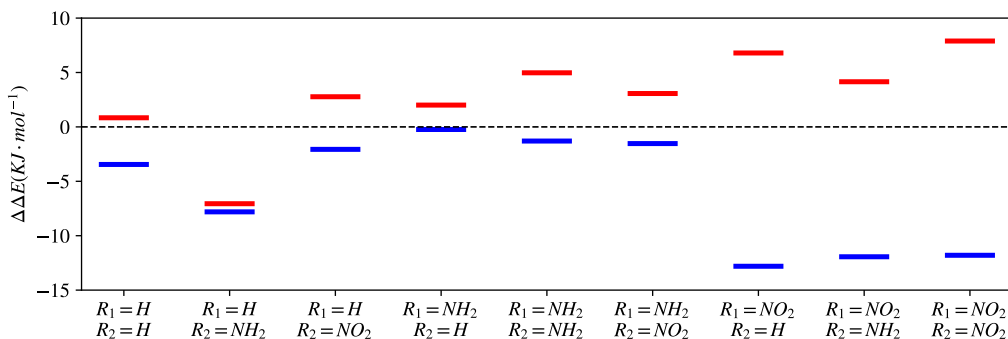


Figure 3.22: Electronic energy of the *R* (red) and *S* (blue) energy of each derivative in their optimal field, relative to the non OEEF-perturbed derivative's energy.

An important feature of note, was that the  $R_1=NH_2$ ,  $R_2=H$  and  $R_1=NH_2$ ,  $R_2=NH_2$  systems stabilised the *R* isomer so much that it resulted in a reversal of which isomer was more stabilised, and so to account for this, the optimal OEEF direction was also flipped. This posed a new mechanism, by which the OEEF pushed electron density from the  $R_1$  amine, onto the cyclising amine, to stabilise the *S* isomer. This also slightly destabilised the *R* isomer by pushing some of the ketone electron density onto  $C_\beta$ , making it less electrophilic.

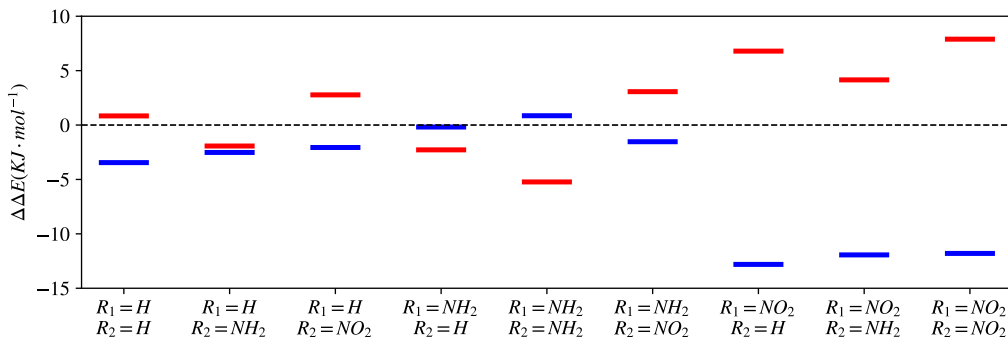


Figure 3.23: Electronic energy of the *R* (red) and *S* (blue) isomer of each derivative as perturbed by the  $R_1=H$ ,  $R_2=H$  optimal field, relative to the non OEEF-perturbed derivative's energy.

Through all of these derivatisations, it was possible that any stabilisation that occurred was simply from the increase in bulk of the molecule resulting in a larger anisotropic polarisability in the Z axis, so further calculations were performed, with all permutations of  $R_1, R_2=H, t\text{-Bu}$ . Since the *tert*-butyl groups contain large amounts of bulk without introducing any extra charge, any deviation from  $R_1, R_2=H$  could be considered due to polarisation-only effects. These calculations were carried

out as per all other relaxed OEEF scans, in Psi4 at M06-2X/6-31+G\*, however only the perturbation of the optimal field direction of  $R_1, R_2=H$  (as shown in [Figure 3.21](#)) was investigated. These results were plotted in [Figure 3.24](#).

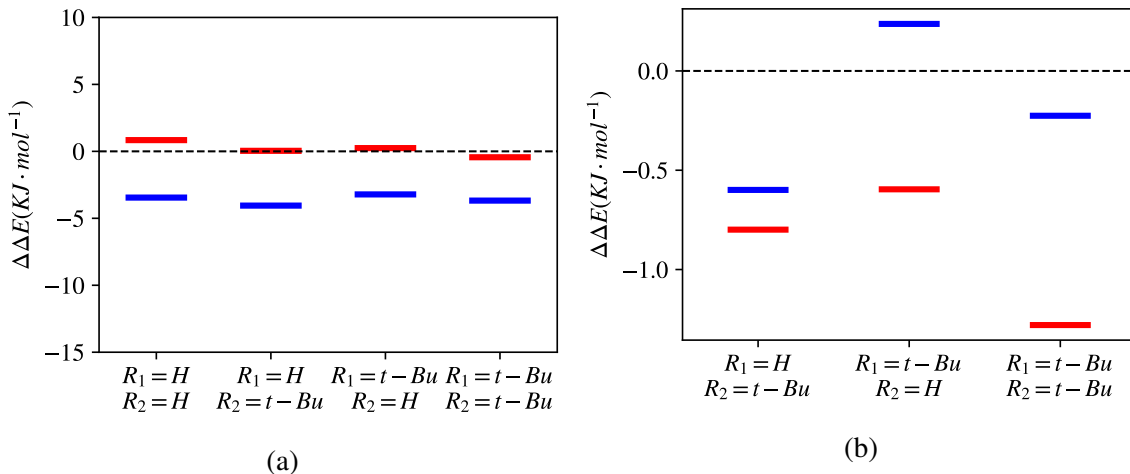


Figure 3.24: a) Electronic energy of the  $R$  (red) and  $S$  (blue) isomers of all permutations of  $R_1, R_2=H, t$ -Bu, as perturbed by the optimal  $S$  selective OEEF for  $R_1=H, R_2=H$ , a) relative to their non-perturbed energy. Differences between the energy of the  $t$ -Bu derivatised geometries and  $R_1=H, R_2=H$  have been plotted in b) to explicitly show the stability afforded by the added polarisability of the bulky groups alone.

Looking at [Figure 3.24](#), the effects of the additional polarisation that arise from having larger functionality can be considered minimal, with a maximum contribution from the addition of  $t$ -Bu groups to be 1.2 kJ·mol<sup>-1</sup>. For the most part, these effects were non-preferable, as the addition of polarisable groups always led to a more stabilised  $R$  isomer, over  $S$ . In cases where the  $S$  isomer was destabilised, this was likely due to the  $t$ -Bu groups accepting the electron density that would otherwise be localised at the cyclising amine, and in cases where the  $R$  isomer was stabilised, this was likely due to the slight increase in electron density that was afforded to the  $\alpha$ - $\beta$  unsaturated ketone.

With polarisability providing minimal contribution to the effects of derivatisation on the stereoselectivity afforded by OEEFs, in order to isolate the influence of through-bond effects of the added functionality from their electrostatic influence, further calculations were performed using point charge perturbation

methods, as described by Gryn'ova and Coote.<sup>54</sup> These methods replace the R groups with specifically placed point charges, and thus any change to the energy of the system as a result of these perturbations can only be considered the result of electrostatic effects.

Taking the M06-2X/6-31+G\* optimised geometry of  $R_1=H$ ,  $R_2=H$ , using ORCA, charges of  $q = +0.1$  and  $q = -0.1$  were placed 3 Å from the  $R_1$  and  $R_2$  terminal hydrogen, in line with their C–H bond. All permutations of  $q_1/q_2 = -0.1, 0, 0.1$  were constructed and single point energy calculations were performed on both the *R* and *S* isomers of each of these geometries, as perturbed by the  $R_1=H$ ,  $R_2=H$  optimal OEEF direction. Their energy was calculated relative to their non OEEF-perturbed counterparts and were plotted in [Figure 3.25](#).

The specific charge strengths were chosen somewhat arbitrarily, however can be considered representative of the overall point charges of the functionality chosen. It could be argued that the magnitude of a nitro group would be significantly more negative and that an amine would be significantly more positive, however much like the rest of this section, these calculations were considered a qualitative investigation into the trends, rather than a quantification of the effects.

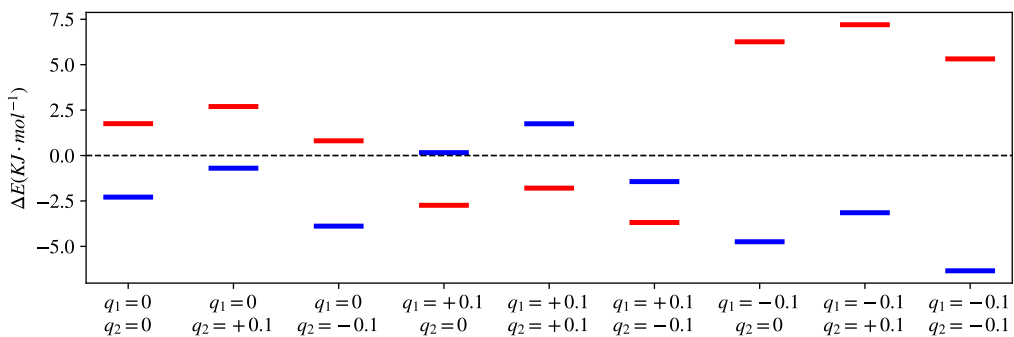


Figure 3.25: Potential energy of the *R* (red) and *S* (blue) isomer of the non derivatised 2'-aminochalcone, with  $q_1/q_2 = 0.1, 0, \text{ or } 0.1$  point charges in place of the R groups.

As can be seen in [Figure 3.25](#), the trends of the system could be identified by looking at the two positions independently. Charges in the  $q_1$  position resulted in the separation of the two species, with

$q_1 = +0.1$  resulting in the inverse separation of the species, stabilising the *R* isomer and destabilising the *S* isomer, and  $q_1 = -0.1$  resulting in a large destabilisation of the *R* isomer with a modest stabilisation of the *S* isomer. In the  $q_2$  position, the charges had a more subtle, systematic effect, influencing both isomers equally, with  $q_2 = +0.1$  destabilising both and  $q_2 = -0.1$  stabilising both.

This was likely the result of the charges in  $q_2$  changing the angle of the molecular dipole subtly, either pushing or pulling the electron density across the molecule. Through its extensively conjugated system, this changed the charge ratio between the cyclising amine and  $C_\beta$ . As with functionality in the  $R_1$  position, the contribution of the charges in the  $q_1$  position mostly effected the cyclising amine, either pushing electron density onto the amine, or pulling it away, causing it to be more or less reactive (respectively).

Both of these findings were in line with the the results of [Figure 3.23](#), with the  $q_1 = +0.1$  behaving similarly to the  $-NH_2$  group and the  $q_1 = -0.1$  behaving similarly to the  $NO_2$  group. Using [Figure 3.23](#) as a baseline, this point charge study could be considered an energy decompositon method, and thus given the negligible influence of the increased polarisability shown in [Figure 3.24](#), any stabilisation effects not seen in [Figure 3.25](#) could be considered to come specifically from through bond effects. Given how well the point charges alone replicate these results, it can be concluded that the effects of the *R* groups were predominantly electrostatic in nature.

### 3.6 Thermodynamic benchmarking of the derivatised and non-derivatised species

To truly understand the effects of derivatisation, the reactant, transition state and product of  $R_1, R_2=H$   $R_1, R_2=NO_2$  and  $R_1, R_2=NH_2$  were calculated, with thermal corrections to obtain Gibbs free energies and rate constants. These were performed at M06-2X/6-31+G\* as solvated in CPCM ethanol, using the same methodology as per [Section 3.4](#). This included the same constraining of the C=O bond and C=O–Ph angle, and relaxing the species within the presence of the catalytic and stereoselective OEEFs as identified in [Section 3.3](#). To maintain consistent results, the optimised directions of  $\vec{F}$  at a magnitude of  $0.1 \text{ V}\cdot\text{\AA}^{-1}$  from [Section 3.3](#) were used, ignoring those identified in [Section 3.5](#). For completeness, and to ascertain how a stronger OEEF would effect the rate constants, the process was repeated at a field strength of  $|\vec{F}| = 0.2 \text{ V}\cdot\text{\AA}^{-1}$ . The rate constants calculated were tabulated in [Table 3.7](#), and their relative differences have been plotted in [Figure 3.26](#). A more positive value of  $\Delta \log(k)$  represents a greater increase in the reaction rate over the unperturbed reaction for the catalytic perturbations. For the stereoselective perturbations, a positive value represents a rate increase of the formation of the *S* product over the *R* product, and a negative value represents a rate decrease.

**Table 3.7:**  $\log(k)$  rate constants for the cyclisation of both the  $R_1, R_2=H$  and  $R_1, R_2=NO_2$  forms of 2'-aminochalcone, both unperturbed and perturbed by catalytic, *S* selective, and *S* anti-selective OEEFs.

$ \vec{F}  (\text{V}\cdot\text{\AA}^{-1})$	$R_1$	$R_2$	Unperturbed	<i>S</i> selective	<i>S</i> anti-selective	Catalytic
0.1	H	H	-7.1	-6.4	-8.0	-4.7
0.2	H	H	-7.1	-6.0	-9.3	-3.9
0.1	$NO_2$	$NO_2$	-10.3	-12.8	-11.2	-5.3
0.2	$NO_2$	$NO_2$	-10.3	-12.5	-11.9	-4.1
0.1	$NH_2$	$NH_2$	-5.5	-4.0	-7.0	-4.1
0.2	$NH_2$	$NH_2$	-5.5	-5.7	-8.0	-4.4

The results from these scans were not consistent with the results of [Section 3.5](#) in that the  $R_1, R_2=NO_2$  resulted in negligible stereoselectivity while the results of  $R_1, R_2=NH_2$  were surprisingly comparable to those of  $R_1, R_2=H$ . This was predominantly due to two specific processes; firstly, the process of optimising the geometry in [Section 3.5](#) occurred in the gas phase, reducing the amount of screening that would realistically exist between the remote functionality and the reaction site. This resulted

in geometries in which the transition state bonding distances were much larger, placing the charged functionality closer to the Z axis, which as discussed in [Section 3.3](#) had an increased effect on the stereoselectivity of the reaction.

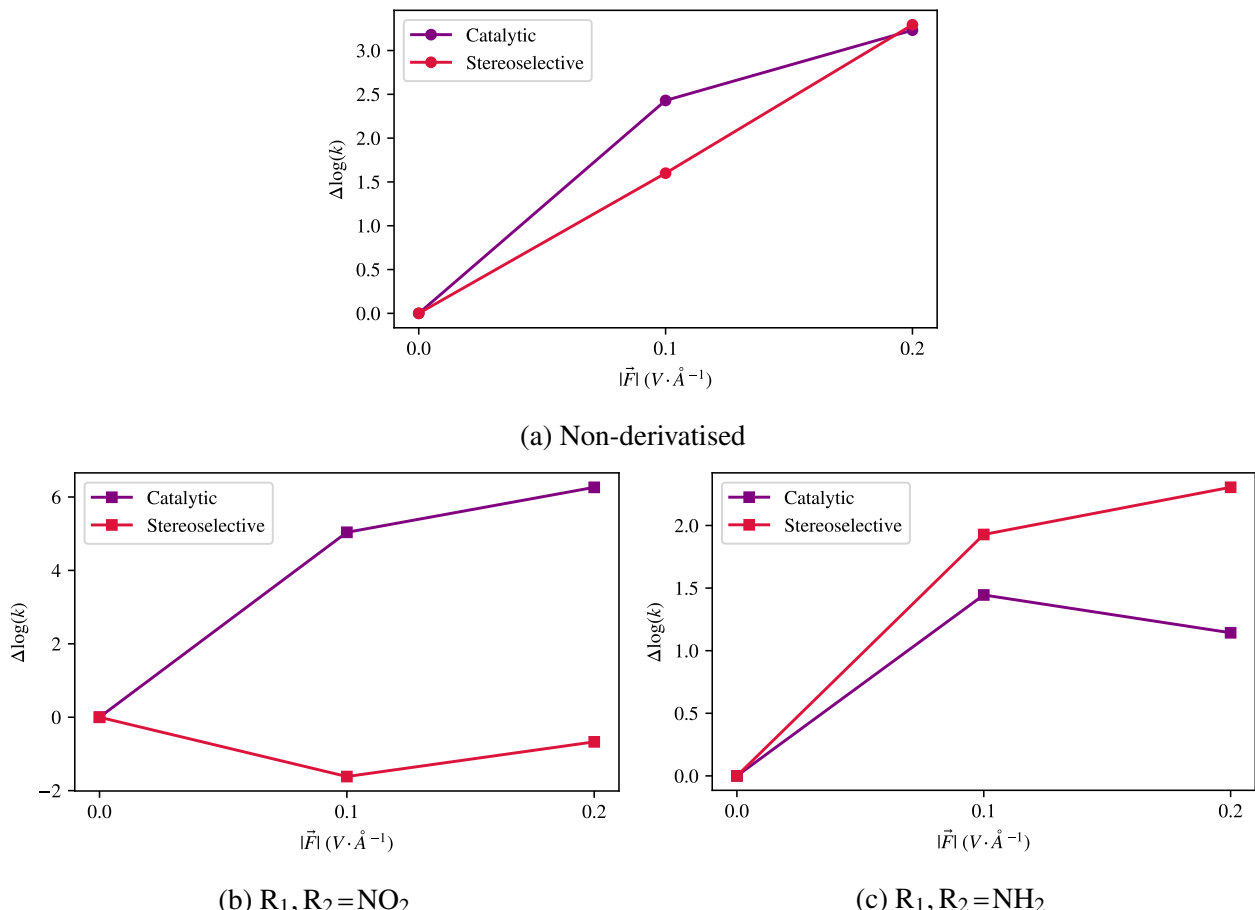


Figure 3.26:  $\log(k)$  rate constant differences between the catalytic and stereoselective OEEFs for the non-derivatised and  $R_1, R_2 = NO_2$  derivatised species of 2'-aminochalcone in  $|\vec{F}| = 0, 0.1$  and  $0.2 V \cdot \text{\AA}^{-1}$

Secondly and probably more significantly, [Section 3.5](#) only looked at the trends of differences in the transition state stability, as previous findings within this research had shown that the reactant was particularly unperturbed by the OEEF. This turned out not to be the case when derivatised, with the nitro groups making the reactant more polarisable than the product. The same effect was noticed for  $R_1, R_2 = NH_2$  however to a much smaller extent. This polarisability shift also influenced the effects of the OEEF away from the expected catalytic and stereoselective behaviours, with the nitro groups ultimately increasing  $\Delta G^{\ddagger}$  for the *S* isomer and the amine groups decreasing it.

In general however, due to the resonance effects of the 5' amine ( $R_1=NH_2$ ) contributing electron density to 2' amine, all of the  $R_1, R_2=NH_2$  perturbations resulted in larger rate constants and faster reaction times, which when coupled with the non-negligible stereoselective rate differences could be considered a positive if trying to make the reaction occur within a more reasonable timeframe. The inverse happened for the 5' nitro group ( $R_1=NO_2$ ), with the electron withdrawing properties deactivating the 2' amine, resulting in a significant decrease to the rate constants of the species.

While the stereoselective effects of the  $R_1, R_2=NO_2$  species were significantly lacking, the catalytic effects were impressive, though this was largely a product of how slow the non OEEF-perturbed reaction itself was. In reality, this catalysis did not occur as a result of the the stabilisation of the transition state, so much as a destabilisation of the reactant. This was can be clearly identified, as contrary to conventional logic, the increasing OEEF strength ultimately resulted in a less stable transition state.

One particularly significant issue of note was that due to rule (iv), if  $\vec{F}$  was not aligned with  $\vec{\mu}$ , with the restraints put in place on the position and angle of the ketone, the molecule would start to contort itself to align its dipole with the OEEF (full figures of this can be seen in [Appendix E](#)). As the magnitude of the OEEF increased, this contorting increased, both causing significant internal strain within the molecule, and moving the reaction axis out of alignment with the OEEF. From this alone it can be seen that for an OEEF that is not aligned to a molecule's dipole to be able to have a positive effect, it either needs to be toggled fast enough to not allow the geometry to relax and align itself, or the magnitude of the OEEF needs to be tuned in such a way for the rotational torque afforded by the processes in rule (iv) to be mitigated by the structure of the solvent itself.

$$ee = \frac{k_{\text{favoured}} - k_{\text{disfavoured}}}{k_{\text{favoured}} + k_{\text{disfavoured}}} \quad (11)$$

With the recognition that both the non-derivatised and amine derivatised ( $R_1, R_2 = \text{NH}_2$ ) species of 2'-aminochalcone could be considered viable options for further study, enantiomeric excesses (ee) were subsequently calculated from the relative *R* and *S* isomer rate constants, using [Equation \(11\)](#).<sup>55</sup> This gave theoretical ee of 95.1% and 99.9% for the non-derivatised species in  $|\vec{F}| = 0.1$  and  $0.2 \text{ V}\cdot\text{\AA}^{-1}$ , and 99.8% and 99.0% for the amine derivatised species in the same field strengths, respectively.

## 4 Conclusion and Future Research

Through the use of DFT based computational investigations, it was found that the non-catalysed pathway of the cyclisation of 2'-aminochalcone to aza-flavanone was a good candidate for further study into the effects of OEEF mediated stereocontrol.

When solvated in ethanol, which was identified as the optimal solvent choice, an OEEF oriented predominantly in-line with the newly forming N–C bond resulted in stereoselection at the the newly formed chiral centre, with an ee of 95.1% for  $|\vec{F}| = 0.1 \text{ V}\cdot\text{\AA}^{-1}$  and 99.9% for  $|\vec{F}| = 0.2 \text{ V}\cdot\text{\AA}^{-1}$ . Derivatisation was able to influence the rate and stereoselection afforded by the OEEF, however the specific intricacies of each system need to be investigated individually, as few generalisations could be made from this particular study.

Catalysis of the formation of racemic aza-flavanone was also found to be achievable with an OEEF directed along the reaction axis from the newly forming N–C bond up to the ketone, with an increase in  $\log(k)$  rate constant of 2.4 at  $|\vec{F}| = 0.1 \text{ V}\cdot\text{\AA}^{-1}$  and 3.2 at  $|\vec{F}| = 0.2 \text{ V}\cdot\text{\AA}^{-1}$ .

This research focused on the use of optimal OEEF directions to obtain maximum stereoselective and catalytic results, however these effects were observed in non-optimal OEEF directions as well. Any deviation in OEEF direction from parallel with the reaction axis, in line with the newly forming N–C bond caused a quantifiable amount of stereoselection.

It was found that the magnitude of the OEEF had to be kept relatively low for stereoselection to occur, as the rotational torque experienced by the molecule as  $\vec{\mu}$  would try to align with  $\vec{F}$ , prevented the molecule from remaining in a stereoselective orientation. This is an important consideration when taking this research experimentally into the realm of freely rotating molecules in solution, as

maintaining their orientation will likely come down to balancing the rotational torque with stabilising intermolecular interactions.

While this research was limited in what it could accomplish owing to time constraints, and resource limitations, it has provided valuable insights into the behaviour of the reaction, allowing for research to move forward with a more solid understanding of its behaviour within an OEEF.

Research by Xu *et al.*<sup>12</sup> has demonstrated that one way to overcome many off the limitations of conventional solvents within an electric field is to use EEFs to align a solvent composed of ionic liquids (IL), allowing them to generate an IEF that can act upon the solvated reaction. In doing so, this would overcome issues pertaining to competing electrochemical reactions, and would reduce the likelihood of an electronic double layer forming at the electrodes that would drastically attenuate the OEEF. Work by the Pas and Coote groups has shown that IEFs of  $> 0.2 \text{ V}\cdot\text{\AA}^{-1}$  can be formed and maintained for extended periods of time within an IL by aligning them with an OEEF before removing the field,<sup>56</sup> and there is further evidence to show that ILs exhibit extensive hydrogen bonding within solution<sup>57–59</sup> that could be utilised to align a solute in a particular orientation relative to the generated IEF. This hydrogen bonding could potentially provide enough rotational stabilisation to the overcome the rotational torque of the OEEF, allowing for stereoselection to occur.

In conjunction with research carried out by other members of the Pas group, the next steps for this research are to explore the reaction using polarisable molecular dynamics and *ab initio* molecular dynamics approaches to understand how different ILs will influence stereoselectivity, and to better understand the role of the generated IEF in translating this theoretical work into a more viable experimental protocol.

## 5 References

- (1) Pocker, Y.; Buchholz, R. F. *J. Am. Chem. Soc.* **1970**, *92*, 2075–2084.
- (2) Carbonell, E. *et al. J. Phys. Chem.* **1991**, *95*, 179–183.
- (3) Warshel, A. *et al. Chem. Rev.* **2006**, *106*, 3210–3235.
- (4) Sini, G. *et al. J. Mol. Struct.* **1991**, *229*, 163–188.
- (5) Shaik, S. S. *J. Am. Chem. Soc.* **1981**, *103*, 3692–3701.
- (6) Shaik, S.; de Visser, S. P.; Kumar, D. *J. Am. Chem. Soc.* **2004**, *126*, 11746–11749.
- (7) Meir, R. *et al. ChemPhysChem* **2010**, *11*, 301–310.
- (8) Stuyver, T. *et al. Wiley Interdiscip. Rev. Comput. Mol. Sci.* **2020**, *10*, 1–22.
- (9) Aragonès, A. C. *et al. Nature* **2016**, *531*, 88–91.
- (10) Shaik, S. *et al. J. Am. Chem. Soc.* **2020**, *142*, 12551–12562.
- (11) Wang, Z. *et al. J. Am. Chem. Soc.* **2018**, *140*, 13350–13359.
- (12) Xu, L.; Izgorodina, E. I.; Coote, M. L. *J. Am. Chem. Soc.* **2020**, *142*, 12826–12833.
- (13) Wang, C. *et al. J. Am. Chem. Soc.* **2019**, *141*, 7122–7136.
- (14) Atkins, P.; de Paula, J., *Atkins' Physical Chemistry*, 10th ed.; Oxford University Press: Oxford, United Kingdom, 2014.
- (15) Ciampi, S. *et al. Chem. Soc. Rev.* **2018**, *47*, 5146–5164.
- (16) Tőkés, A. L.; Janzsó, G. *Synth. Commun.* **1989**, *19*, 3159–3168.
- (17) Zheng, X. *et al. Synth. Commun.* **2013**, *43*, 1023–1029.
- (18) Saito, K.; Moriya, Y.; Akiyama, T. *Org. Lett.* **2015**, *17*, 3202–3205.
- (19) Prat, D. *et al. Green Chem.* **2016**, *18*, 288–296.

- (20) Cramer, C. J., *Essentials of computational chemistry : theories and models*, 2nd ed.; John Wiley & Sons Ltd: West Sussex, England, 2004, p 596.
- (21) Skodje, R. T.; Truhlar, D. G. *J. Phys. Chem.* **1981**, *85*, 624–628.
- (22) Sherer, E. C.; Cramer, C. J. *Organometallics* **2003**, *22*, 1682–1689.
- (23) Klamt, A.; Schüürmann, G. *J. Chem. Soc., Perkin Trans. 2* **1993**, *799*–805.
- (24) Garcia-Ratés, M.; Neese, F. *J. Comput. Chem.* **2020**, *41*, 922–939.
- (25) Marenich, A. V.; Cramer, C. J.; Truhlar, D. G. *J. Phys. Chem. B* **2009**, *113*, 6378–6396.
- (26) Zhao, Y.; Truhlar, D. G. *Theor. Chem. Acc.* **2008**, *120*, 215–241.
- (27) Hehre, W. J.; Ditchfield, R; Pople, J. A. *J. Chem. Phys.* **1972**, *56*, 2257–2261.
- (28) Clark, T. *et al.* *J. Comput. Chem.* **1983**, *4*, 294–301.
- (29) Dunning, T. H. *J. Chem. Phys.* **1989**, *90*, 1007–1023.
- (30) Kendall, R. A.; Dunning, T. H.; Harrison, R. J. *J. Chem. Phys.* **1992**, *96*, 6796–6806.
- (31) Mardirossian, N.; Head-Gordon, M. *Mol. Phys.* **2017**, *115*, 2315–2372.
- (32) Mardirossian, N.; Head-Gordon, M. *J. Chem. Phys.* **2016**, *144*, 214110.
- (33) Goerigk, L. *et al.* *Phys. Chem. Chem. Phys.* **2017**, *19*, 32184–32215.
- (34) Weigend, F.; Ahlrichs, R. *Phys. Chem. Chem. Phys.* **2005**, *7*, 3297.
- (35) Weigend, F. *Phys. Chem. Chem. Phys.* **2006**, *8*, 1057–1065.
- (36) Neese, F. *et al.* *Chem. Phys.* **2009**, *356*, 98–109.
- (37) Santra, G.; Martin, J. M. L. In *AIP Conf. Proc.* 2019; Vol. 2186, p 030004.
- (38) Gryn'ova, G. *et al.* *Nat. Chem.* **2013**, *5*, 474–481.
- (39) Gryn'ova, G.; Coote, M. L. *J. Am. Chem. Soc.* **2013**, *135*, 15392–15403.
- (40) Frisch, M. J. *et al.*, *Gaussian 16 Revision C.01*; Gaussian, Inc., Wallingford, Connecticut: 2016.

- (41) Bunce, R. A.; Nammalwar, B. *J. Heterocycl. Chem.* **2011**, *48*, 613–619.
- (42) Hanwell, M. D. *et al. J. Cheminform.* **2012**, *4*, 17.
- (43) Neese, F. *Wiley Interdiscip. Rev. Comput. Mol. Sci.* **2012**, *2*, 73–78.
- (44) Ho, J.; Coote, M. L. *Theor. Chem. Acc.* **2010**, *125*, 3–21.
- (45) Lu, T.; Chen, F. *J. Comput. Chem.* **2012**, *33*, 580–592.
- (46) Markland, T. E.; Ceriotti, M. *Nat. Rev. Chem.* **2018**, *2*, 0109.
- (47) Brehm, M. *et al. Phys. Chem. Chem. Phys.* **2012**, *14*, 5030.
- (48) Cassone, G. *et al. J. Chem. Phys.* **2015**, *142*, 054502.
- (49) Mattioli, E. J. *et al. J. Phys. Chem. C* **2019**, *123*, 26370–26378.
- (50) Parrish, R. M. *et al. J. Chem. Theory Comput.* **2017**, *13*, 3185–3197.
- (51) Turney, J. M. *et al. Wiley Interdiscip. Rev. Comput. Mol. Sci.* **2012**, *2*, 556–565.
- (52) Smith, D. G. A. *et al. J. Chem. Phys.* **2020**, *152*, 184108.
- (53) Schrödinger, L. The PyMOL Molecular Graphics System, Version 2.6, 2015.
- (54) Gryn'ova, G.; Coote, M. L. *Aust. J. Chem.* **2017**, *70*, 367.
- (55) Schniebeli, S. T. *et al. J. Am. Chem. Soc.* **2009**, *131*, 3965–3973.
- (56) Belotti, M. *et al. J. Am. Chem. Soc.* **2021**, *143*, 17431–17440.
- (57) Mohd, N. *et al. In AIP Conf. Proc.* 2017; Vol. 1809, p 020035.
- (58) Canongia Lopes, J. N. A.; Pádua, A. A. H. *J. Phys. Chem. B* **2006**, *110*, 3330–3335.
- (59) Brehm, M. *et al. Zeitschrift für Phys. Chemie* **2013**, *227*, 177–204.
- (60) Weigend, F.; Kattannek, M.; Ahlrichs, R. *J. Chem. Phys.* **2009**, *130*, 164106.
- (61) Breneman, C. M.; Wiberg, K. B. *J. Comput. Chem.* **1990**, *11*, 361–373.
- (62) Zhang, J. *J. Chem. Theory Comput.* **2018**, *14*, 572–587.

## Acknowledgements

I'd like to acknowledge and thank the following people for helping to make this work a possibility:

First and foremost, none of this work would have been possible without the unfaltering, and constantly positive support from Katya. You have always had confidence in my abilities, even when I've not been able to find the confidence in myself, and I'm sure that you will continue to do so as I tackle a PhD. Your support since I emailed you as an undergraduate at another university has motivated me to keep pursuing better things in academia and your support on a personal level and constant empathy for what I've endured this year has prevented me from giving up entirely.

Secondly, Michelle Coote who through listening to my tired and incoherent ramblings has opened up new avenues of investigation in my work and picked apart some of my less logical thought processes. You have kept my brain in check and ensured that I don't become complacent in my work.

To the staff and facilities of the Monash eResearch centre and MASSIVE, who's support and resources facilitated this research at the most fundamental level. Without computational resources, computational chemistry doesn't happen, and despite a plethora of technical issues, you've pulled through, have been been there when I've needed, and have always responded promptly to any and all service tickets I've had to lodge.



All the members of the Pas group, who have endured my constant excited posting on Slack, and who have helped me with otherwise illogical issues. It sucks that we've not been able to share an office this past year but hopefully soon we'll be popping out for a cheeky coffee together. In particular to Peter, Michael and Tom who have helped me with all sorts of technical and theoretical queries and issues that I've had over the course of the year. Some of your contributions to my project won't have made it into this work, but will definitely help, going forward.



To everyone who has helped to provide feedback on my thesis; Katya, Michelle, Peter, Sophie, Michael and India. You helped me to consolidate my mindless ramblings into a cohesive, polished thesis that's deserving of submission. Thank you.

And finally, to all the members of my personal support network, both academic and non-academic, Michael, Erica, Alex, Rhys, India and Steph, without who I doubt I'd have had the emotional energy to make it through it through the year, and deal with the setbacks of research.

# Appendix

Working ipython notebook files for the processing of data relating to benchmarks and all raw data for the OEEF scanning sections can be found at [GitHub](#). Due to the enormity of the undertaking, geometries have not been included and due to the enormity of their file sizes, PyMOL files have not been shared either, however both are available [upon request](#).

## A Raw data from the pathway benchmarking in [Section 3.1](#)

Table A.1: Raw  $\Delta G^\circ$  from the benchmarking of the reaction pathways in [Section 3.1](#). The blank cells pertain to calculations that were not performed.

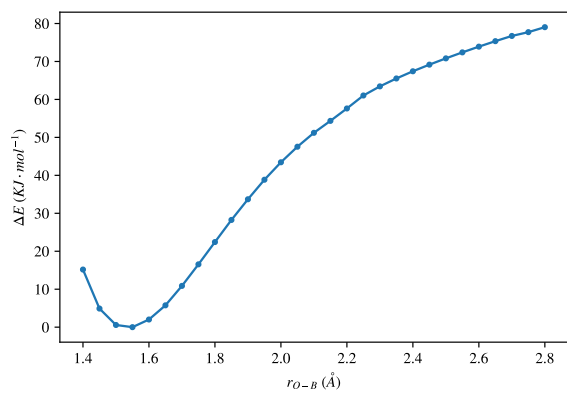
Pathway	Energy ( $E_h$ )				
	Reactant	Transition State 1	Intermediate	Transition State 2	Product
Non-activated	-709.212961	-709.171714			-709.187604
Brønsted Acid 1		Barrierless	-709.620615	-709.599167	-709.634264
Brønsted Acid 2		-786.010860	-709.596855	Barrierless	-709.648273
Brønsted Base		-785.166022	-708.726998	-708.701422	-708.755359
Lewis Acid		Barrierless	-1033.879641	-1033.855176	-1033.885971
Lewis Base		Barrierless	-960.453357	-960.453357	-960.483276

Table A.2: raw  $\Delta G^\circ$  of the species used top balance the reaction trajectories in [Section 3.1](#).

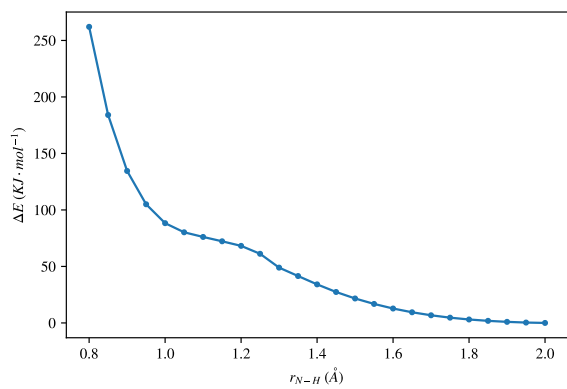
Additive	Energy ( $E_h$ )
H <sub>2</sub> O	-76.440078
H <sub>3</sub> O <sup>+</sup>	-76.830283
Piperidine	-251.221244
BF <sub>3</sub>	-324.652124

Table A.3: Transition state imaginary frequencies and calculated transmission coefficients for the intermediate formation and cyclisation steps respectively, for the reaction pathways benchmarked in [Section 3.1](#).

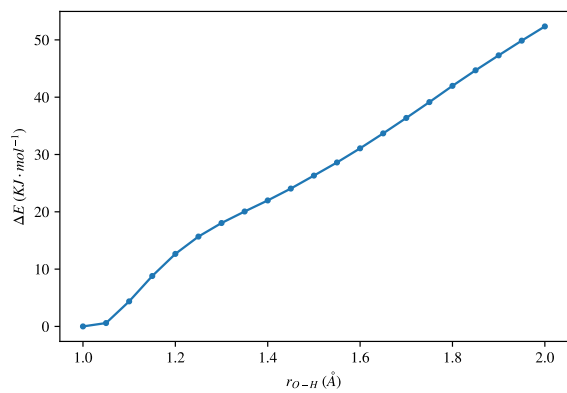
	Frequency 1 ( $cm^{-1}$ )	$\kappa_1$	Frequency 2 ( $cm^{-1}$ )	$\kappa_2$
Non-activated			-521.93	1.323
Brønsted Acid 1	Barrierless		-382.40	1.157
Brønsted Acid 2	-1228.66	13.612	Barrierless	
Brønsted Base	-1200.35	1.185	-534.59	1.342
Lewis Acid	Barrierless		-427.78	1.202
Lewis Base	Barrierless		-548.23	1.365



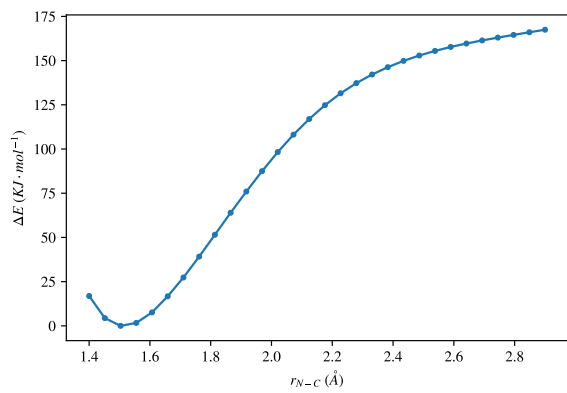
(a) PES scan of the Lewis acid ( $BF_3$ ) attaching into **1**, scanning along the O–B bond length.



(b) PES scan of the Lewis base ( $piperidine^-$ ) deprotonating the **1** amine, scanning along the amine N–H bond length.



(c) PES scan of the protonation of the 'Brønsted acid 1' pathway (**1** → **7**) scanning along the forming O–H bond length.



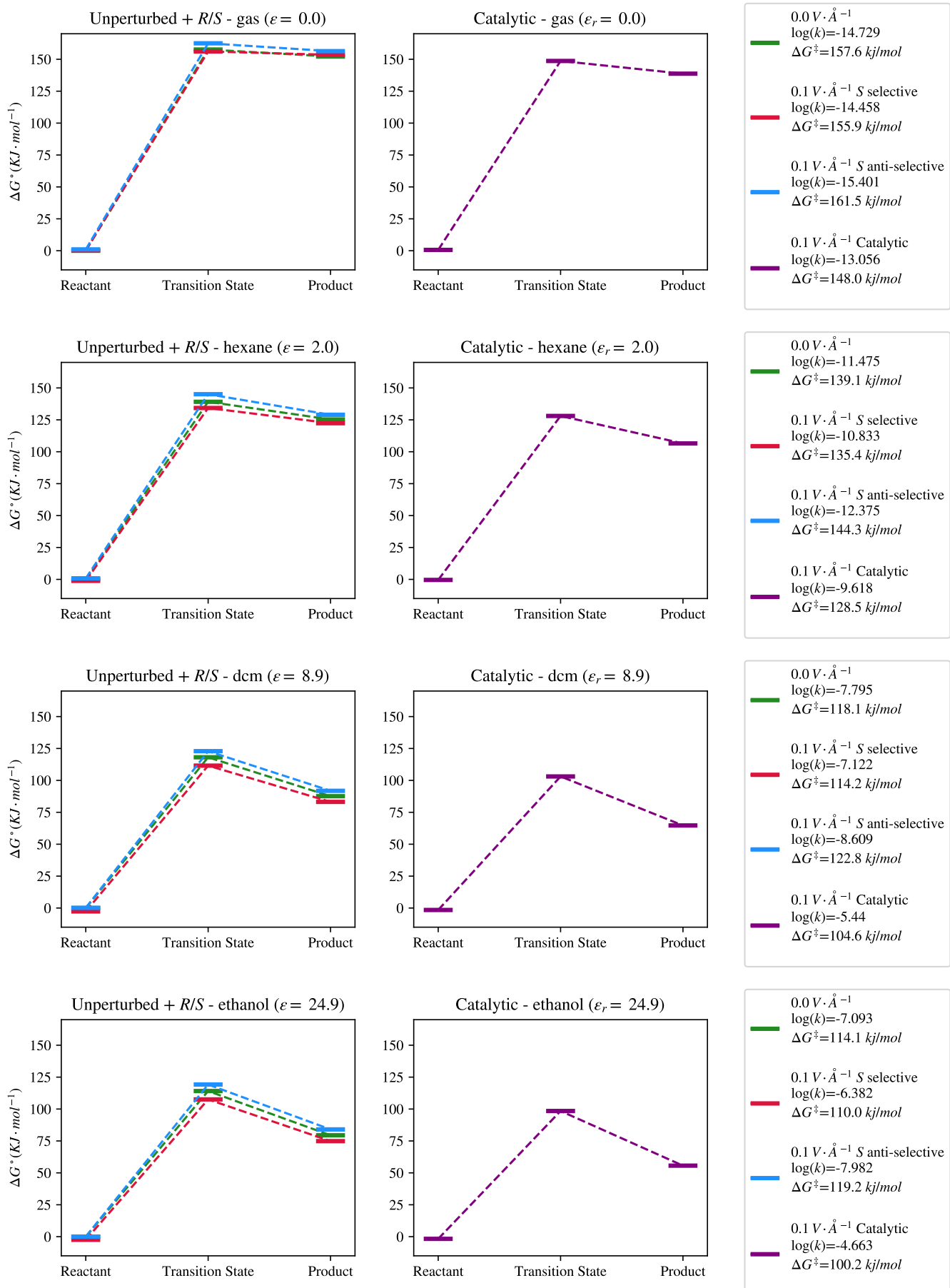
(d) PES scan of the cyclisation of the 'Brønsted acid 2' pathway (**11** → **4**) scanning along the forming N–C bond length.

Figure A.1: PES scans along the reaction coordinate for all barrierless steps in the various pathways.

## B Raw data and reaction trajectories from [Section 3.4](#)

Table B.1: Raw  $\Delta G^\circ$ , transition state imaginary frequencies, and transmission coefficients for the benchmarks performed in [Section 3.4](#)

$ \vec{F} $ (V·Å $^{-1}$ )	Energy ( $E_h$ )			Frequency (V·Å $^{-1}$ )	$\kappa$
	Reactant	Transition state	Product		
Gas					
None	-708.898472	-708.838431	-708.840519	-472.60	1.243
0.1 (Catalytic)	-708.898222	-708.841845	-708.845638	-434.69	1.210
0.1 ( <i>S</i> anti-selective)	-708.898075	-708.836571	-708.838916	-472.30	1.247
0.1 ( <i>S</i> anti-selective)	-708.898395	-708.839004	-708.840006	-472.70	1.166
Hexane					
None	-708.906434	-708.853442	-708.858711	-489.29	1.276
0.1 (Catalytic)	-708.906599	-708.857667	-708.865868	-465.54	1.246
0.1 ( <i>S</i> anti-selective)	-708.906126	-708.851179	-708.857311	-487.68	1.274
0.1 ( <i>S</i> anti-selective)	-708.906126	-708.851179	-708.857311	-487.68	1.257
DCM					
None	-708.916525	-708.871672	-708.885508	-486.00	1.266
0.1 (Catalytic)	-708.915264	-708.875421	-708.890046	-460.69	1.240
0.1 ( <i>S</i> anti-selective)	-708.914632	-708.867875	-708.879710	-484.81	1.271
0.1 ( <i>S</i> anti-selective)	-708.915696	-708.872193	-708.883006	-462.14	1.242
Ethanol					
None	-708.916180	-708.872721	-708.885927	-482.10	1.267
0.1 (Catalytic)	-708.916826	-708.878676	-708.894984	-457.65	1.236
0.1 ( <i>S</i> anti-selective)	-708.916163	-708.870769	-708.884170	-486.67	1.273
0.1 ( <i>S</i> anti-selective)	-708.917107	-708.875217	-708.887664	-458.69	1.238
DMSO					
None	-708.916626	-708.873640	-708.887326	-480.16	1.264
0.1 (Catalytic)	-708.917322	-708.879704	-708.896476	-456.87	1.235
0.1 ( <i>S</i> anti-selective)	-708.916525	-708.871672	-708.885508	-486.00	1.272
0.1 ( <i>S</i> anti-selective)	-708.916525	-708.871672	-708.885508	-486.00	1.235
Water					
None	-708.916820	-708.874020	-708.887956	-481.96	1.267
0.1 (Catalytic)	-708.917509	-708.880107	-708.897132	-456.64	1.235
0.1 ( <i>S</i> anti-selective)	-708.916764	-708.872039	-708.886105	-486.57	1.273
0.1 ( <i>S</i> anti-selective)	-708.917400	-708.876558	-708.889680	-459.05	1.238



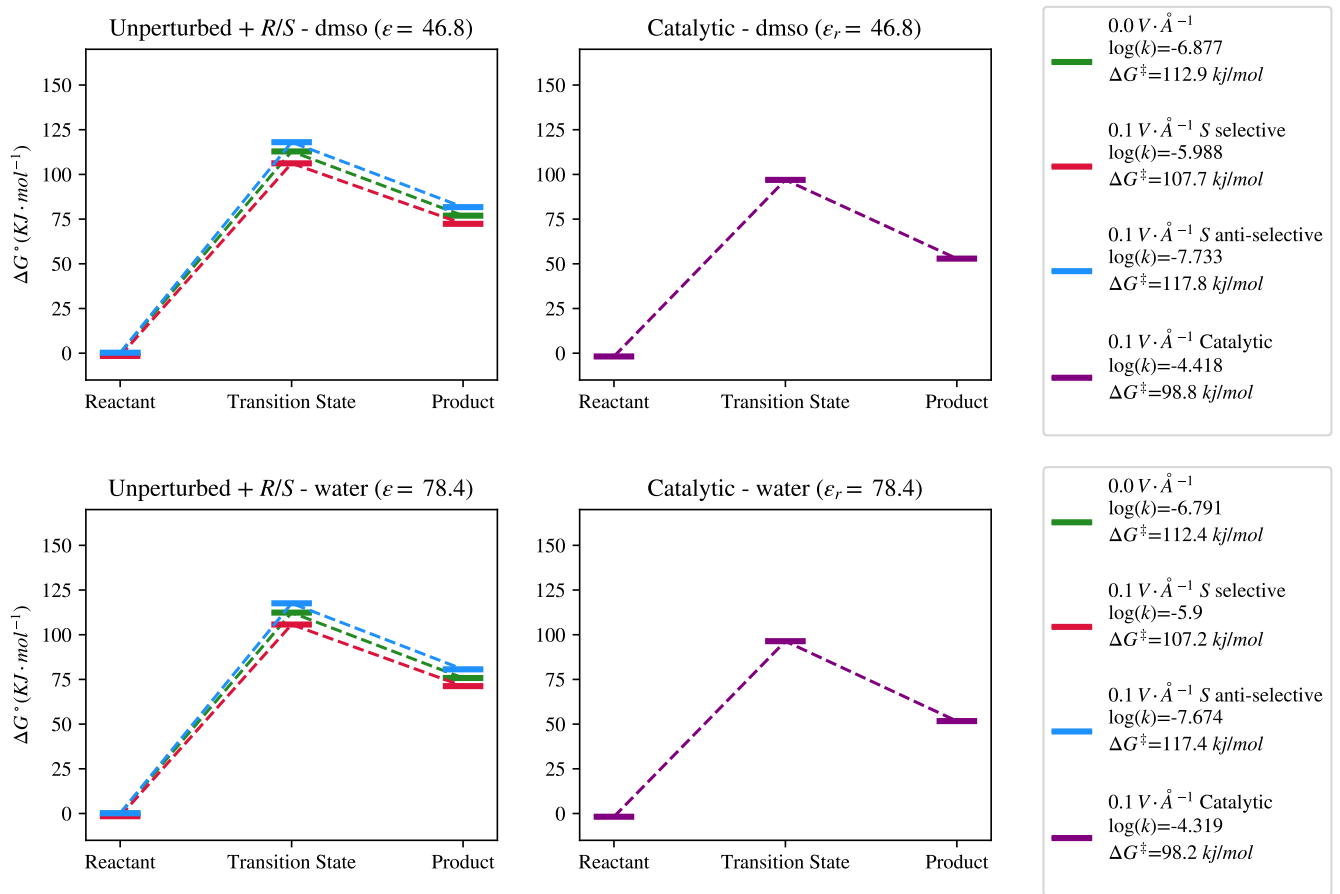
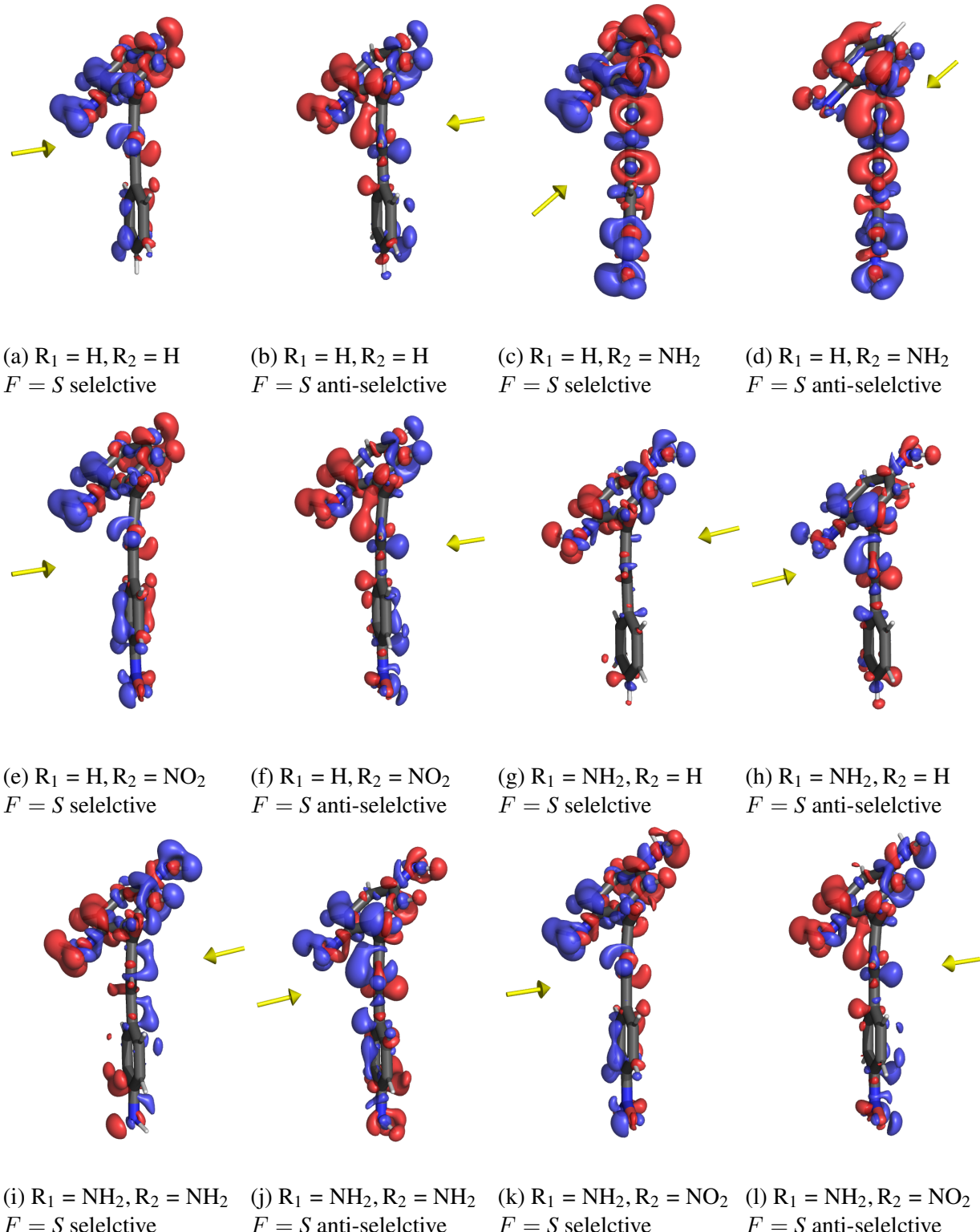
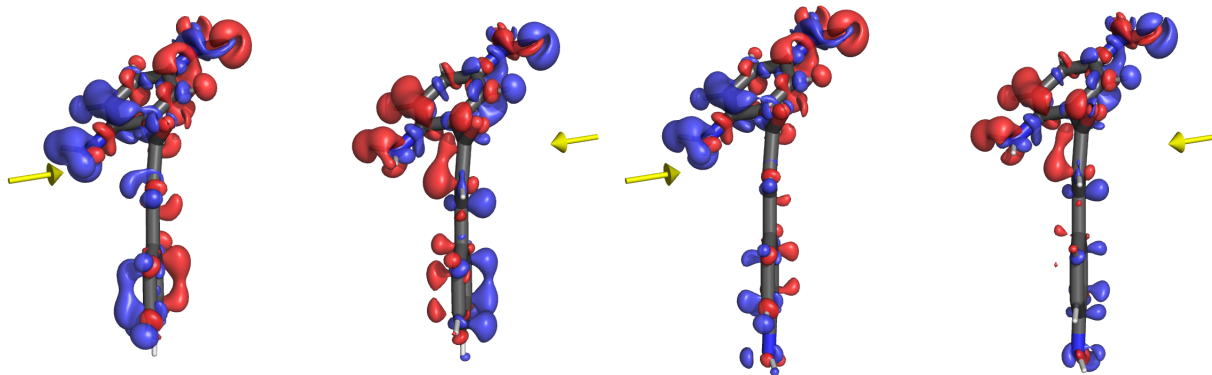


Figure B.1: Reaction trajectories for the relaxed benchmarks performed in [Section 3.4](#)

## C Electron density difference maps of the derivatives discussed in Section 3.5



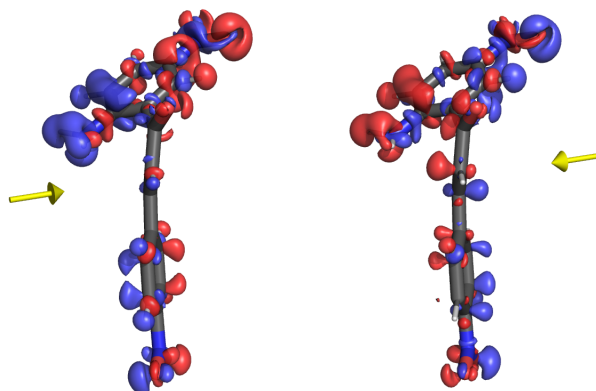


(m)  $R_1 = NO_2, R_2 = H$   
 $F = S$  selelctive

(n)  $R_1 = NO_2, R_2 = H$   
 $F = S$  anti-selective

(o)  $R_1 = NO_2, R_2 = NH_2$   
 $F = S$  selelctive

(p)  $R_1 = NO_2, R_2 = NH_2$   
 $F = S$  anti-selective



(q)  $R_1 = NO_2, R_2 = NO_2$   
 $F = S$  selelctive

(r)  $R_1 = NO_2, R_2 = NO_2$   
 $F = S$  anti-selective

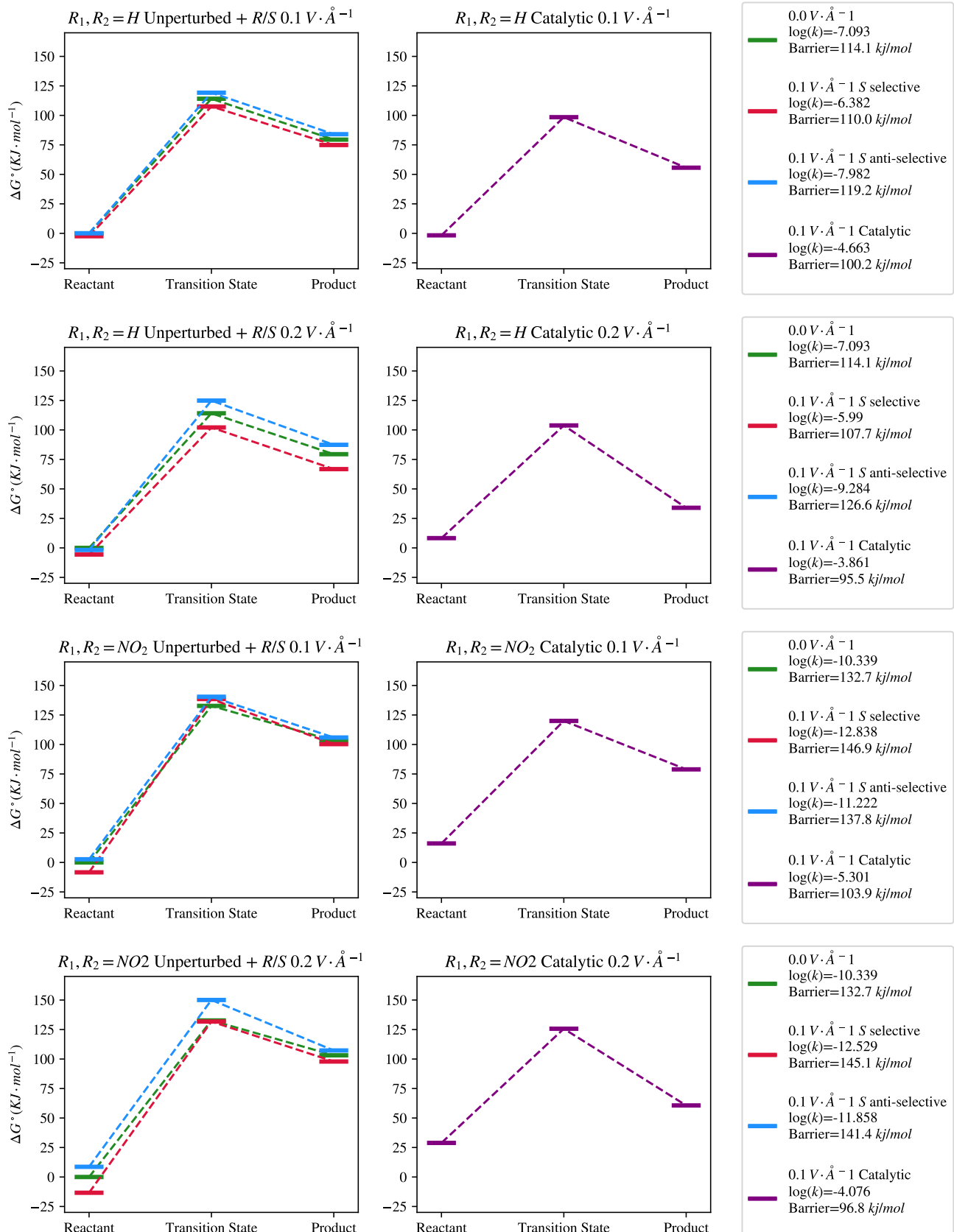
Figure C.1: Electron density difference isosurfaces following an isovalue of 0.0002 for the optimal  $0.1 \text{ V}\cdot\text{\AA}^{-1}$   $S$  selective/ $S$  anti-selective OEEF directions for each of the derivatives, calculated at M06-2X/6-31+G\*, solvated in CPCM ethanol. The red and blue isosurfaces represent regions of increased and decreased electron density respectively. The yellow arrow is a representation of the direction of the applied field vector.

## D Raw data and reaction trajectories from Section 3.4

Table D.1: Raw  $\Delta G^\circ$ , transition state imaginary frequencies, and transmission coefficients for the benchmarks performed in [Section 3.6](#)

$ \vec{F} $ (V·Å $^{-1}$ )	Energy ( $E_h$ )			Frequency (V·Å $^{-1}$ )	$\kappa$
	Reactant	Transition state	Product		
Non-derivatised ( $R_1, R_2 = H$ )					
None	-708.916180	-708.872721	-708.885927	-482.10	1.267
0.1 (Catalytic)	-708.916826	-708.878676	-708.894984	-457.65	1.236
0.1 ( <i>S</i> anti-selective)	-708.916163	-708.870769	-708.884170	-486.67	1.273
0.1 ( <i>S</i> anti-selective)	-708.917107	-708.875217	-708.887664	-458.69	1.238
0.2 (Catalytic)	-708.913028	-708.876643	-708.903230	-431.65	1.207
0.2 ( <i>S</i> anti-selective)	-708.916849	-708.868621	-708.882899	-488.55	1.276
0.2 ( <i>S</i> anti-selective)	-708.918317	-708.877299	-708.890741	-436.64	1.212
Derivatised ( $R_1, R_2 = NO_2$ )					
None	-1117.798403	-1117.747859	-1117.759120	-511.75	1.308
0.1 (Catalytic)	-1117.792269	-1117.752700	-1117.768354	-489.44	1.277
0.1 ( <i>S</i> anti-selective)	-1117.797376	-1117.744906	-1117.758071	-517.59	1.316
0.1 ( <i>S</i> anti-selective)	-1117.801593	-1117.745641	-1117.760201	-486.77	1.273
0.2 (Catalytic)	-1117.787395	-1117.750533	-1117.775299	-443.38	1.220
0.2 ( <i>S</i> anti-selective)	-1117.795114	-1117.741251	-1117.757556	-527.43	1.331
0.2 ( <i>S</i> anti-selective)	-1117.803489	-1117.748212	-1117.761122	-484.36	1.270
Derivatised ( $R_1, R_2 = NH_2$ )					
None	-819.567938	-819.527946	-819.541147	-453.96	1.232
0.1 (Catalytic)	-819.572619	-819.535792	-819.550188	-427.28	1.202
0.1 ( <i>S</i> anti-selective)	-819.569241	-819.526057	-819.540957	-463.67	1.244
0.1 ( <i>S</i> anti-selective)	-819.569181	-819.530218	-819.544841	-432.05	1.207
0.2 (Catalytic)	-819.576743	-819.539267	-819.556151	-418.99	1.193
0.2 ( <i>S</i> anti-selective)	-819.570568	-819.525077	-819.541019	-468.29	1.249
0.2 ( <i>S</i> anti-selective)	-819.572210	-819.531785	-819.548810	-407.72	1.182

## E Transition state geometries and reaction trajectories from the OEEF perturbed benchmarks in Section 3.6



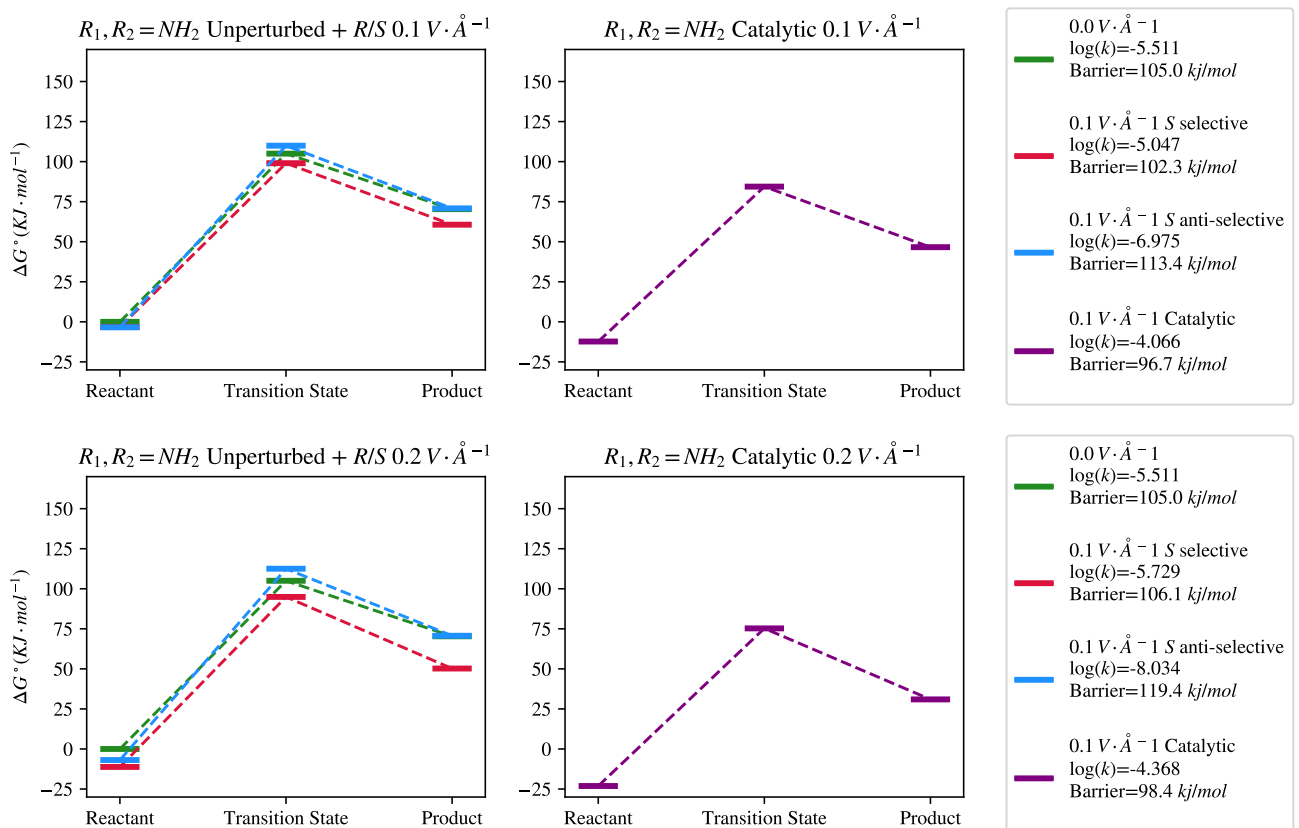
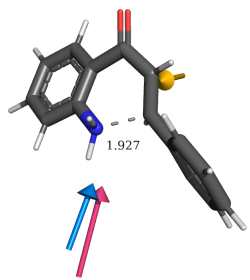
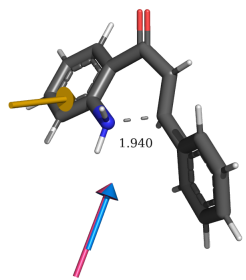


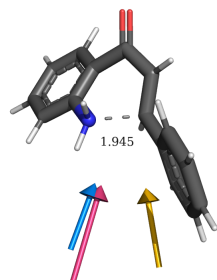
Figure E.1: Reaction trajectories for the benchmarks performed in [Section 3.6](#).



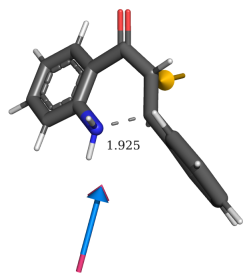
(a)  $R_1, R_2 = H$   
 $|\vec{F}| = 0.1 \text{ V}\cdot\text{\AA}^{-1}$   
*R* selective



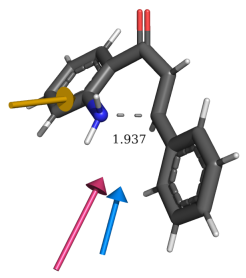
(b)  $R_1, R_2 = H$   
 $|\vec{F}| = 0.1 \text{ V}\cdot\text{\AA}^{-1}$   
*S* selective



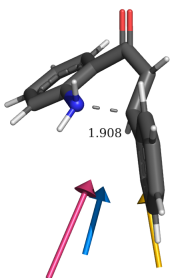
(c)  $R_1, R_2 = H$   
 $|\vec{F}| = 0.1 \text{ V}\cdot\text{\AA}^{-1}$   
Catalytic



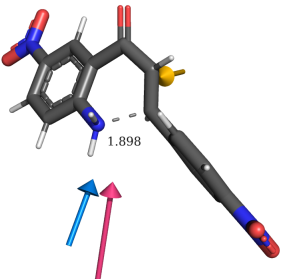
(d)  $R_1, R_2 = H$   
 $|\vec{F}| = 0.2 \text{ V}\cdot\text{\AA}^{-1}$   
*R* selective



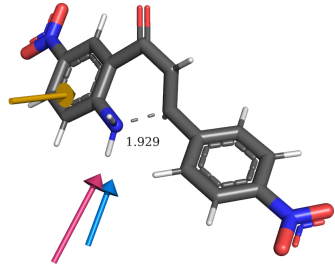
(e)  $R_1, R_2 = H$   
 $|\vec{F}| = 0.2 \text{ V}\cdot\text{\AA}^{-1}$   
*S* selective



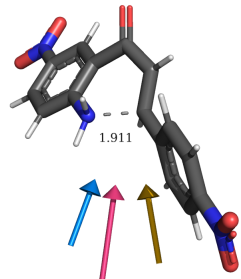
(f)  $R_1, R_2 = H$   
 $|\vec{F}| = 0.2 \text{ V}\cdot\text{\AA}^{-1}$   
Catalytic



(g)  $R_1, R_2 = \text{NO}_2$   
 $|\vec{F}| = 0.1 \text{ V}\cdot\text{\AA}^{-1}$   
*R* selective



(h)  $R_1, R_2 = \text{NO}_2$   
 $|\vec{F}| = 0.1 \text{ V}\cdot\text{\AA}^{-1}$   
*S* selective



(i)  $R_1, R_2 = \text{NO}_2$   
 $|\vec{F}| = 0.1 \text{ V}\cdot\text{\AA}^{-1}$   
Catalytic

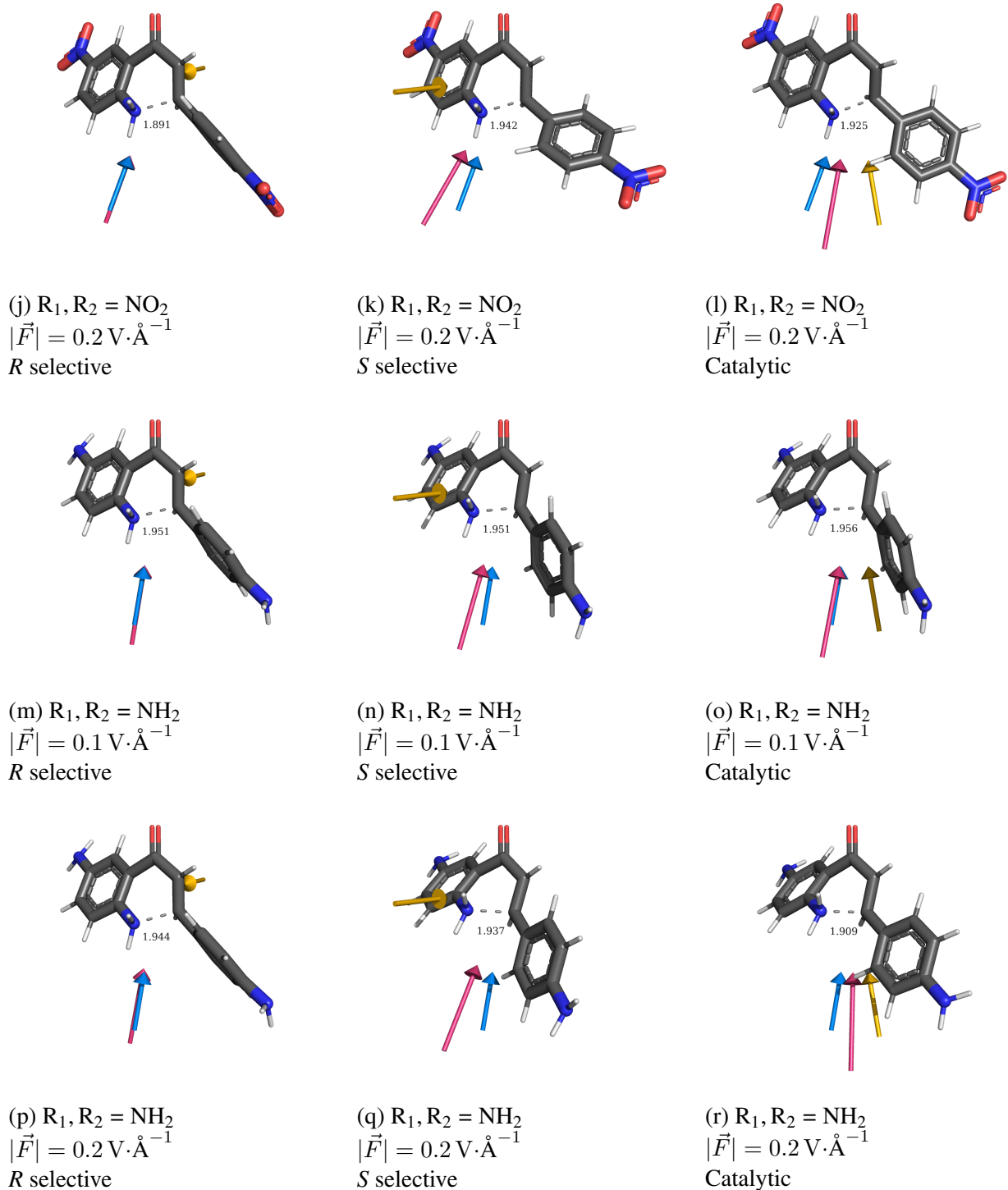


Figure E.2: Transition state geometries from the OEEF perturbed benchmarks in [Section 3.6](#)

## F Full theoretical choices, approximations and precision used throughout the project

Software Package	Job type	Functional	Basis set	Solvation	Convergence criteria	Integration grid	Approximations	Field
ORCA 5.0.1 <sup>43</sup>	Opt	M062X <sup>26</sup>	Pathway Benchmarking: low level opt aug-cc-pVTZ <sup>29,30</sup> aug-cc-pVTZ/JK	CPCM <sup>23,24</sup> Ethanol	Tightscf tightopt	Defgrid3	RIJK <sup>60</sup>	No
ORCA 5.0.1 <sup>43</sup>	Opt	$\omega$ B97M-V <sup>32</sup>	Pathway Benchmarking: High level opt Def2-QZVPP <sup>34</sup> def2/j <sup>35</sup>	SMD <sup>25</sup> Ethanol	Verytightscf tightopt	Defgrid3	RIJCosX <sup>36</sup>	No
ORCA 5.0.1 <sup>43</sup>	NEB-TS	M062X <sup>26</sup>	Pathway Benchmarking: TS Searching NEB aug-cc-pVTZ <sup>29,30</sup> aug-cc-pVTZ/JK	CPCM <sup>23,24</sup> Ethanol	Tightscf tightopt	Defgrid3	RIJK <sup>60</sup>	No
ORCA 5.0.1 <sup>43</sup>	OptTS	$\omega$ B97M-V <sup>32</sup>	Pathway Benchmarking: High level opt - TS Def2-QZVPP <sup>34</sup> def2/j <sup>35</sup>	SMD <sup>25</sup> Ethanol	Verytightscf tightopt	Defgrid3	RIJCosX <sup>36</sup>	No
ORCA 5.0.1 <sup>43</sup>	SCAN	$\omega$ B97M-V <sup>32</sup>	Pathway Benchmarking: PES scanning Def2-TZVPD <sup>34</sup> Def2/J <sup>35</sup>	SMD <sup>25</sup> Ethanol	Tightscf	Defgrid2	RIJCosX	No
ORCA 5.0.1 <sup>43</sup>	Freq	$\omega$ B97M-V <sup>32</sup>	Pathway Benchmarking: High level opt Frequencies Def2-QZVPP <sup>34</sup> Def2/j <sup>35</sup>	SMD <sup>25</sup> Ethanol	Verytightscf	Defgrid3	RIJCosX <sup>36</sup>	No
Multiwfn 3.8 <sup>45</sup>			Partial charge determination CHELPG <sup>61</sup> charges based on the wavefunctions calculated above, using a grid density of 0.1 Å. Multiwfn uses the LIBRETA <sup>62</sup> package for evaluation of the electrostatic potential					
ORCA 5.0.1 <sup>43</sup>	Single Point	M062X <sup>26</sup>	Benchmarking barrier as a function of $F_y$ 6-31+G(d) <sup>27,28</sup>	SMD <sup>25</sup> Ethanol/none	Standard	Defgrid3	none	Yes
ORCA 5.0.1 <sup>43</sup>	Single Point	M062X <sup>26</sup>	Benchmarking R/S separation as a function of $F_z$ 6-31+G(d) <sup>27,28</sup>	SMD <sup>25</sup> Ethanol/none	Standard	Defgrid3	none	Yes

ORCA 5.0.1 <sup>43</sup>	Single Point	M062X <sup>26</sup>	Benchmarking catalysis/separation ( $F_y/F_z$ ) as function of dielectric medium (CPCM) 6-31+G(d) <sup>27,28</sup> CPCM <sup>23,24</sup> varied	Standard	Defgrid3	none	Yes
Psi4 1.4 <sup>50-52</sup>	Opt	M062X <sup>26</sup>	OEEF scans 6-31+G(d) <sup>27,28</sup> none	Standard	590/99	none	Yes
Psi4 1.4 <sup>50-52</sup>	SP	M062X <sup>26</sup>	EDD isosurfaces 6-31+G(d) <sup>27,28</sup> none/CPCM <sup>23,24</sup>	Standard	590/99	none	Yes
ORCA 5.0.1 <sup>43</sup>	Opt NumFreq	M062X <sup>26</sup>	Relaxed OEEF Solvent Benchmarking 6-31+G(d) <sup>27,28</sup> CPCM <sup>23,24</sup> varied	Tightopt	Defgrid3	none	Yes/No
Psi4 1.4 <sup>50-52</sup>	Opt	M062X <sup>26</sup>	Derivative Efield scans 6-31+G(d) <sup>27,28</sup> CPCM <sup>23,24</sup>	Standard	590/99	none	Yes
ORCA 5.0.1 <sup>43</sup>	Single Point	M062X <sup>26</sup>	Point charge perturbation 6-31+G(d) <sup>27,28</sup> none	verytightscf	Defgrid3	none	Yes